Entropy driven phase transitions in hard core lattice gases

By

Dipanjan Mandal

PHYS10201205005

The Institute of Mathematical Sciences, Chennai

A thesis submitted to the

Board of Studies in Physical Sciences

In partial fulfillment of requirements

For the Degree of

DOCTOR OF PHILOSOPHY

of

HOMI BHABHA NATIONAL INSTITUTE

April, 2019

Homi Bhabha National Institute

Recommendations of the Viva Voce Committee

As members of the Viva Voce Committee, we certify that we have read the dissertation prepared by Dipanjan Mandal entitled “Entropy driven phase transitions in hard core lattice gases" and recommend that it maybe accepted as fulfilling the thesis requirement for the award of Degree of Doctor of Philosophy.

____ Date:

Chairman: Purusattam Ray

____ Date:

Guide/Convener: Rajesh Ravindran

____ Date:

Examiner: Sakuntala Chatterjee

____ Date:

Member 1: Sanatan Digal

____ Date:

Member 2: Ganesh Ramachandran

Final approval and acceptance of this thesis is contingent upon the candidate’s submission of the final copies of the thesis to HBNI.

I hereby certify that I have read this thesis prepared under my direction and recommend that it may be accepted as fulfilling the thesis requirement.

Date:

Place: **Guide**

STATEMENT BY AUTHOR

This dissertation has been submitted in partial fulfillment of requirements for an advanced degree at Homi Bhabha National Institute (HBNI) and is deposited in the Library to be made available to borrowers under rules of the HBNI.

Brief quotations from this dissertation are allowable without special permission, provided that accurate acknowledgement of source is made. Requests for permission for extended quotation from or reproduction of this manuscript in whole or in part may be granted by the Competent Authority of HBNI when in his or her judgement the proposed use of the material is in the interests of scholarship. In all other instances, however, permission must be obtained from the author.

Dipanjan Mandal

DECLARATION

I, hereby declare that the investigation presented in the thesis has been carried out by me. The work is original and has not been submitted earlier as a whole or in part for a degree / diploma at this or any other Institution / University.

Dipanjan Mandal

List of Publications arising from the thesis

- **Published**

  1. **D. Mandal**, T. Nath, R. Rajesh, *Estimating the Critical Parameters of the Hard Square Lattice Gas Model*, J. Stat. Mech. **2017**, 043201 (2017).
  2. **D. Mandal**, R. Rajesh, *The columnar-disorder phase boundary in a mixture of hard squares and dimers*, Phys. Rev. E **96**, 012140 (2017).
  3. **D. Mandal**, T. Nath, R. Rajesh, *Phase transitions in a system of hard Y-shaped particles on the triangular lattice*, Phys. Rev. E **97**, 032131 (2018).

- **In preparation**

  1. **D. Mandal**, G. Rakala, N. Vigneshwar, S. Biswas, K. Damle, D. Dhar, R. Rajesh, *Phase transitions in a system of hard plates on a three dimensional cubic lattice*, in preparation.

Other Publications not included in the thesis

- **Published**

  1. N. Vigneshwar, **D. Mandal**, K. Damle, D. Dhar, R.Rajesh, *Phase diagram of a system of hard cubes on the cubic lattice*, Phys. Rev. E **99**, 052129 (2019).
  2. S. Chakraborty, A. Mallick, **D. Mandal**, S. K. Goyal, S. Ghosh , *Non-Markovianity of qubit evolution under the action of spin environment*, Sci. Rep. **9**, 2987 (2019).

List of presentations and participations at conferences

• Contributed presentations

1. Talk given on *Entropy driven phase transitions in hard core lattice gases* in the *One Day Soft Matter Symposium* held at the Indian Institute of Technology, Madras
2. Talk given on *Phase Transitions in the System of Hard Y-shaped Particles on Triangular Lattice* in the *APS March Meeting 2018* in LACC, Los Angeles
3. Presented poster on *Phase Transitions in the System of Hard Y-shaped Particles on Triangular Lattice* in the *5th Indian Statistical Physics Communuty Meeting 2018* in ICTS, Bangalore
4. Presented poster on *Estimating the Critical Parameters of the Hard Square Lattice Gas Model* in the *4th Indian Statistical Physics Community Meeting 2017*, in ICTS, Bangalore

• Conferences attended

1. *One Day Soft Matter Symposium* held at Indian Institute of Technology, Madras (25th January, 2019)
2. Workshop on *Entropy, Information and Order in Soft Matter* held at International Centre for Theoretical Sciences, Bangalore (28-31 August, 2018)
3. *APS March Meeting 2018* held at LACC, Los Angeles (5-9 March, 2018)
4. *Indian Statistical Physics Community Meeting 2018* (ISPCM 2018) held at International Centre for Theoretical Sciences, Bangalore (16-18 February, 2018)
5. *Indian Statistical Physics Community Meeting 2017* (ISPCM 2017) held at International Centre for Theoretical Sciences, Bangalore (17-19 February, 2017)
6. *Fracmeet 2017* held at The Institute of Mathematical Sciences, Chennai (04-07 January 2017)

7. *Bangalore School on Statistical Physics - VII* held at International Centre for Theoretical Sciences, Bangalore (01-15 July, 2016)
8. *Bangalore School on Statistical Physics -VI* held at Raman Research Institute, Bangalore (02-18 July 2015)

To

My Parents

and

Sister

ACKNOWLEDGEMENTS

First and foremost I would like to express my sincere gratitude to my supervisor Prof. R. Rajesh for his constant support and encouragement during my PhD life. His proper guidance and insightful knowledge has helped me to learn the subject and to build up the thesis. It is a wonderful experience in working with him.

I am thankful to Prof. Deepak Dhar, Prof. Kedar Damle, Prof. Sibasish Ghosh and Prof. Kabir Ramola for allowing me to work with them and learn from their experience and insight. I am grateful to Prof. Gautam Menon, Prof. Satyavani Vemparala, Prof. Ganesh Ramachandran, Prof. Sanatan Digal and Prof. Purusatta Ray for their valuable suggestions and constructive criticism about my thesis work.

I am thankful to my collaborators N. Vigneshwar, Trisha Nath, Arindam Mallick, Sagnik Chakraborty and Geet Rakala for sharing their knowledge and expertise with me.

I would like to thank my friends Sanjoy, Sagnik, Pulak, Arindam, Anirban, Arnab, Jilmy, Prasanna, Abinash, Atanu, Pranendu, Rupam, Anupam, Digjoy and Akashdeep. Their direct or indirect help in leading a cheerful life at IMSc is memorable. I also thank to IMSc football, badminton and cricket players. I have enjoyed a lot playing with them.

Finally, I would like to express my love and gratitude to my parents and sister. It would not have been possible to reach this far without their continuous support and inspiration.

Contents

Contents i

Synopsis 1

List of Figures 11

List of Tables 17

1 Introduction 19

1.1 Entropy driven phase transitions 20

1.2 Hard square lattice gas 23

1.3 Mixture of hard squares and dimers 25

1.4 Hard plates on a cubic lattice 27

1.5 Hard Y-shaped particles 28

1.6 Overview of the thesis 29

2 Hard square lattice gas 31

2.1 Introduction 31

2.2 Model and Outline of Calculation 32

2.3 Calculation of Eigenvalue of T 40

2.4 Calculation of Partition Functions of Tracks 43

2.4.1 Partition function of track of width 2 43

2.4.2 Partition functions of tracks of width 4 44

2.4.3 Calculation of $a_2^{(L)}(\Delta)$ 47

2.4.4 Calculation of $a_2^{(R)}(\Delta)$ 48
2.5 Results 52
2.6 Conclusion 53

3 Mixture of hard squares and dimers **55**
3.1 Introduction 55
3.2 Model and outline of calculation 56
3.3 Calculation of two-row partition function $\Omega(\ell, \Delta)$ 60
3.4 Interfacial tension and critical parameters 63
3.4.1 Without overhangs 63
3.4.2 With overhangs 66
3.4.2.1 Right Overhangs 69
3.4.2.2 Left Overhangs 73
3.4.2.3 Phase boundary 76
3.4.3 Monte Carlo simulations 77
3.5 Discussion 79

4 Hard plates on cubic lattice **81**
4.1 Introduction 81
4.2 Model & Algorithm 82
4.3 Different Phases 87
4.4 Phase transitions 93
4.4.1 Disordered to Layered Transition 93
4.4.2 Layered to Sublattice Transition 97
4.5 Summary and discussion 100

5 *Y*-shaped particles on triangular lattice **103**
5.1 Introduction 103
5.2 Model and algorithm 104
5.3 One type of particle ($\mathbf{z_A = 0}$) 108

5.4 Two types of Particles ($\mathbf{z_A} = \mathbf{z_B}$) 114
5.5 Conclusion 122

6 Conclusions **129**

Bibliography **133**

Synopsis

Entropy is often regarded as a measure of disorder or randomness in a system. In thermodynamic systems, the ordered state has usually lower entropy than the disordered state. Phase transitions from such disordered to ordered phases are driven by a lowering of energy, and are often referred to as energy driven phase transitions. Well-known examples include paramagnetic-ferromagnetic transition, gas-liquid transition, etc. However, there are many systems for which the opposite is true, i.e., the ordered state has higher entropy compared to the disordered state. These transitions are driven by a gain in entropy, and are often referred to as entropy driven phase transitions.

There are many examples of entropy driven phase transitions. These include freezing transition in a system of hard spheres, disordered-nematic-smectic transition in a system of long rods, ordering transitions in adsorbed layer of gases on metallic surface, etc. Hard Core Lattice Gas (HCLG) models are minimal models to study entropy driven phase transitions and are the simplest systems to study critical phenomena. In HCLG models, particles are constrained to be on lattice sites and interact through only excluded volume interaction, i.e., no two particles may overlap. Since the interaction energy is either zero or infinity, temperature does not play any role. Thus, the phases and phase transitions, if any, depend only on the shape and density of the particle. Various particle shapes that have been studied in literature include triangles, squares, dimers, mixture of squares and dimers, Y-shaped particles, tetrominoes, rods, rectangles, discs, hexagons, etc. Among these, the only model that is exactly solvable model is the hard hexagon model on a triangular lattice. In general, one has to resort to Monte Carlo simulations or use approximate analytical methods to provide estimates for the different thermodynamic quantities.

Despite a long history of study, a general understanding of the dependence of the nature of the emergent phases on the shapes of the particles, as well as the order of appearance of the phases with increasing density, is lacking. Thus, studying in detail the phase behaviour of specific models of differently shaped particles will help in building a more general understanding. However, Monte Carlo simulations with only local moves have difficulty in equilibrating systems near close packing or when the excluded volume per particle is large, thus limiting to the kind of shapes that can be studied. In recent years, more sophisticated Monte Carlo algorithms that involve cluster moves have overcome this difficulty, opening up the study of particles with large excluded volume, as well as on three dimensional lattices. In this thesis we study in detail the phase behaviour of four different models using Monte Carlo algorithms with cluster moves as well as analytical methods. These are (1) hard square model on a square lattice, (2) mixture of hard squares and dimers on a square lattice, (3) hard $2 \times 2 \times 1$ plates on a cubic lattice, and (4) hard Y-shaped particles on a triangular lattice. The results that we have obtained for these different models are summarized below.

Hard square lattice gas

Consider hard 2×2 squares on a two dimensional square lattice. Particles interact only through excluded volume interaction. The hard square model is known to undergo a continuous entropy driven phase transition from a low density fluid-like phase to a high density phase with columnar order. In the columnar phase, the particles preferentially occupy even or odd rows with all columns being equally occupied, or preferentially occupy even or odd columns with all rows being equally occupied. The columnar phase breaks translational symmetry only along one of the two directions. The disorder-columnar transition

Table 1: Estimates of critical activity z_c and critical density ρ_c for columnar-disordered transition of the hard square model.

z_c	ρ_c	Method Used
97.50	0.932	Numerical [3, 8, 9, 10]
6.25	0.64	High density expansion (order one) [2, 1]
11.09	0.76	Flory type mean field [11]
11.09	0.76	Approximate counting [12]
11.13	0.764	Density Functional theory [4, 5]
14.86	0.754	High density expansion (order two) [2]
17.22	0.807	Rushbrooke Scoins approximation [1]
48.25	0.928	Interfacial tension with no defect [7]
52.49	0.923	Interfacial tension with one defect [7]
54.87	0.9326	Interfacial tension with overhang [7]
135.63	-	Interfacial tension in antiferromagnetic Ising model [6]
105.35	0.947	Result in this thesis

has been shown numerically to belong to the Ashkin Teller universality class. Different analytic and combinatorial techniques have been used to estimate the critical parameters. The estimates for critical activity, z_c, and critical density, ρ_c, obtained from different methods are summarized in Table 1. Analytical approaches like high density expansion [1, 2], Flory-type approximations [3], density functional theory [4, 5] etc., underestimate the critical activity by more than a factor of 7 compared to the numerical Monte Carlo result $z_c \approx 97.5$ and $\rho_c \approx 0.932$. The calculations based on estimating the interfacial tension [6, 7] between two ordered phases have been more successful, but the error in estimating the activity is still about 50%.

In this thesis, we significantly improve the estimate for critical activity z_c by calculating, within an approximation scheme, the interfacial tension between two differently ordered columnar phases, and then setting it to zero. For determining the interfacial tension, we have used a pairwise approximation, similar to that used in liquid state theory, that allows for the ordered phases to have multiple defects and the interface between the ordered phases to have overhangs. We estimate $z_c = 105.35$, which is in good agreement with existing Monte Carlo simulation results, and is a significant improvement over earlier best estimates of $z_c = 54.87$ and $z_c = 135.63$.

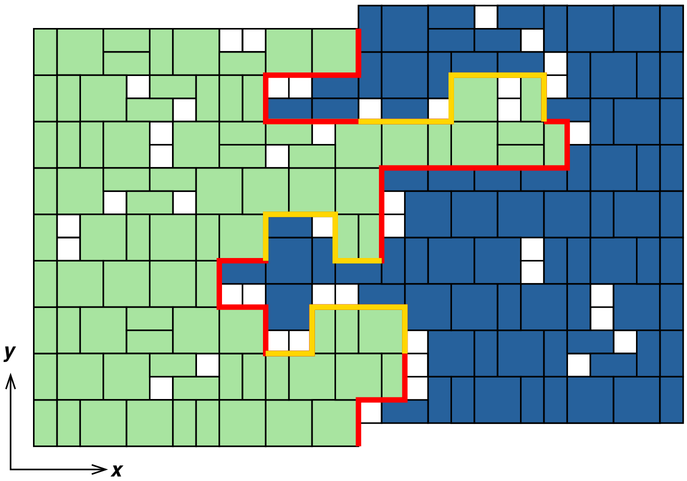

Figure 1: Schematic diagram of an interface between two columnar-ordered phases in the square-dimer model. Green and blue represent particles on even and odd rows respectively. Overhangs are indicated by yellow lines while the rest of the interface is indicated by red lines. The boundary conditions are periodic in the y-direction.

Mixture of hard squares and dimers

The hard square lattice gas model may be generalized to a mixture of squares and dimers. In this model, a mixture of hard 2×2 squares, 2×1 horizontal dimers, 1×2 vertical dimers and 1 × 1 vacancies co-exist on a $L_x \times L_y$ square lattice. We associate activities z_s, z_h, z_v and z_0 with each square, horizontal dimer, vertical dimer and vacancy respectively. This system is known to undergo a phase transition from a disordered phase to a columnar ordered phase with increasing the density of squares [8]. The critical line has continuously varying exponents. Along the fully packed square-dimer line, the system undergoes an Kosterliz-Thouless type transition to a phase with power law correlations. Thus, this model is an example of a system where two critical line with continuously varying exponents meet at a point. By writing an effective Hamiltonian for the two dimensional height field, it was possible to theoretically explain the numerically obtained results along the fully packed line [8]. However, the height mapping does not allow the phase boundary to be determined as the relation between the rigidity and the microscopic parameters is not easy to establish.

In this thesis, we estimate the phase boundary separating the ordered columnar phase and disordered phase by calculating the interfacial tension σ between two differently ordered columnar phases. We create an interface by fixing, the particle on the left half-boundaries and right half-boundaries of the system to be on even and odd rows respectively. A schematic diagram of an interface in the presence of overhangs is shown in Fig. 1. The interfacial tension σ may be defined as

$$e^{-\sigma L_y} = \frac{\sum_I Z^{(I)}}{Z^{(0)}}, \tag{1}$$

where $Z^{(I)}$ and $Z^{(0)}$ are the partition functions of the system in the presence and absence of interface respectively. We calculate the $\sigma(z_s, z_h, z_v, z_0)$ using combinatorial techniques within two different approximation schemes and equate it to zero to obtain the phase boundary. In first case we do not consider the presence of overhangs at the interface. The estimate of the phase boundaries obtained from modelling the interface without overhangs is shown by magenta line in Fig. 2(a) and (b). Here, we have normalized the activities using

$$z_s^{1/4} + z_d^{1/2} + z_0 = 1, \tag{2}$$

where $z_d = z_h = z_v$, such that a two dimensional phase diagram may be obtained. The symbols S, D and V represents fully packed lattice by squares, fully packed lattice by dimers and empty lattice respectively. Numerical results obtained from extensive Monte Carlo simulations are represented by red circles.

Secondly, we consider the presence of overhangs in the interface [see Fig. 1] to improve the estimated results. The estimates of the phase boundaries for the interface with overhangs are represented by blue line in Fig. 2(a) and (b) for both activity and density planes. The analytically obtained phase boundary, with both approximations, is in reasonable agreement with the Monte Carlo simulations. Introducing defects systematically should further improve the estimate.

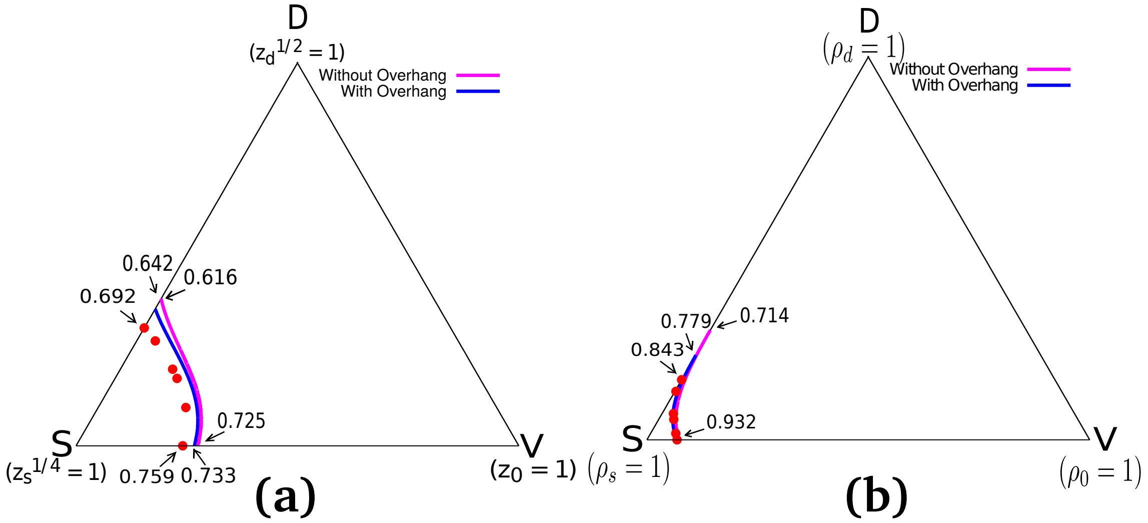

Figure 2: Phase diagram of the square-dimer model in (a) activity z-plane and (b) density ρ-plane. S and D represents the state where the lattice is fully packed by squares and dimers respectively. V represents the empty lattice. The estimates of the phase boundaries obtained from modelling the interface without overhangs is shown by magenta line while that obtained by including overhangs of height one are shown by blue lines. The data points (red circles) are obtained from Monte Carlo simulations.

Hard $2 \times 2 \times 1$ plates in cubic lattice

The generalization of square to three dimensions is the problem of hard $2 \times 2 \times 1$ plates on a $L \times L \times L$ cubic lattice. Three types of plates are possible: x-plate, y-plate and z-plate, having normals along the three principal directions of the cubic lattice. A schematic diagram of three types of particles are shown in Fig. 3.

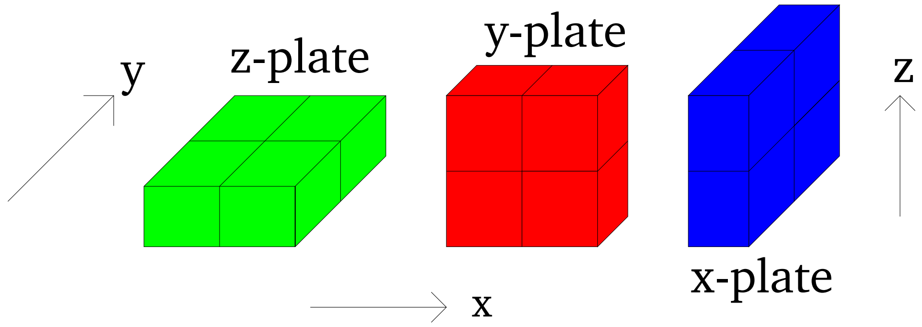

Figure 3: Schematic diagram of three types of particles in the hard plate model: x-plate, y-plate and z-plate, where x, y and z are three principal directions of the cubic lattice.

There are very few detailed studies for the HCLG models in three dimensions. One example is the model of rods [13, 14]. The main cause behind this scarcity is the lack of an efficient Monte Carlo algorithm. The algorithm using local movements of particles fails to equilibrate the system. An efficient algorithm that implements cluster movement of particles is needed to study the phase diagram of models in three dimensions.

We study the different phases and the phase transitions using transfer matrix based Monte Carlo algorithm which works through the following steps. First, we randomly choose a $2 \times 2 \times L$ track and remove all the particles that are completely inside the track. After evacuating the track, we determine the morphology of each $2 \times 2 \times 1$ rung that can be of 16 different types. Using the morphologies we calculate the partition function of the track and refill it with new equilibrium configurations.

The system undergoes two entropy driven phase transitions with increasing the particle density. These are from disordered phase to a layered phase and from a layered phase to sublattice phase. We divide the full lattice into eight appropriate sublattices to characterize different phases obtained in the simulation. In layered phase particles preferentially occupies even or odd planes in a randomly chosen direction. In this phase the symmetry of particle number density is also broken as densities of two of them become higher compared to the density of the third particle. In the high density sublattice phase each type of particle breaks the translational invariance in two directions. In this phase the symmetry of the particle number density is again restored. We have shown that the disordered to layered transition is of second order with the universality class of three dimensional Heisenberg model with cubic anisotropy, while the layered to sublattice transition is first order in nature. Schematic phase diagram in density ρ-plane is shown in Fig. 4.

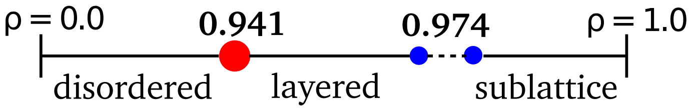

Figure 4: Phase diagram of the hard plate model, where ρ is the density. The continuous phase transition is denoted by red circle, while in the discontinuous phase transition, the co-existence region is shown by dotted line with blue circles denoting the end points.

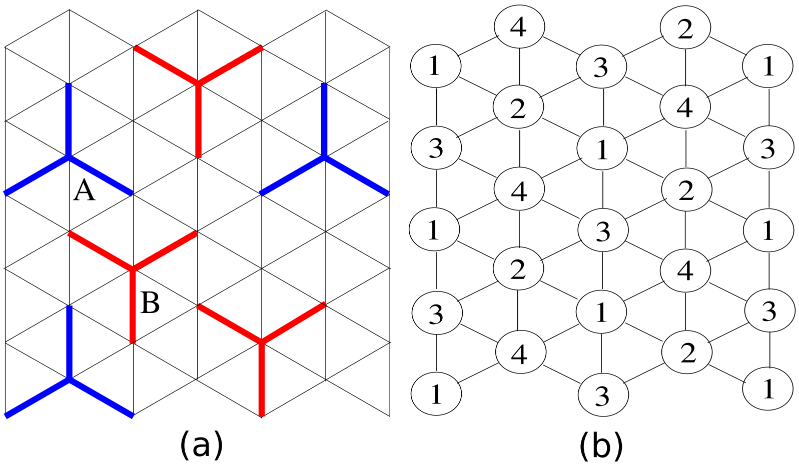

Figure 5: (a) Schematic diagram of a triangular lattice and the two types of Y-shaped particles. A- and B-type particles are represented by blue and red colors respectively. (b) The lattice sites are labeled as $1, 2, 3, 4$ depending on the sublattice they belong to.

Hard Y-shaped particles

Y-shaped particles are observed in physical systems such as Immunoglobulin-G in human blood and trinaphthylene molecules in molecular logic gates. We consider a system of hard Y-shaped particles on a triangular lattice. Each particle consists of a central site and three of its six nearest neighbours chosen alternately, such that there are two types of particles which are mirror images of each other. Schematic diagram of the two types of particles is shown in Fig. 5(a). We associate the chemical potential μ to each particle.

We study the equilibrium properties of the system using grand canonical Monte Carlo simulations that implements an algorithm with cluster moves that is able to equilibrate the system at densities close to full packing. We show that, with increasing density, the system undergoes two entropy-driven phase transitions with two broken-symmetry phases. We

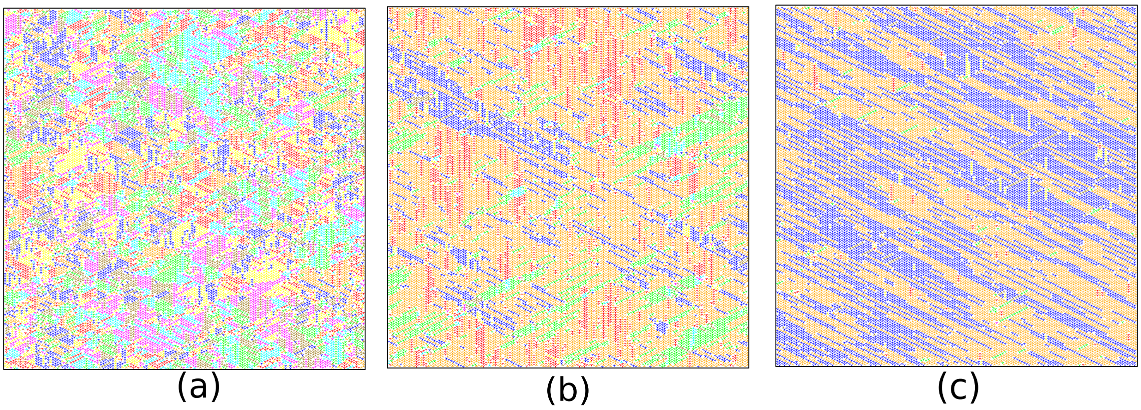

Figure 6: Snapshots of equilibrated configurations of the system of Y-shaped particles, when both types of particles are present, obtained from grand canonical Monte Carlo simulations for different values of μ: (a) disordered phase with $\mu = 4.5$ ($\rho \approx 0.88$), (b) sublattice phase with $\mu = 5.4$ ($\rho \approx 0.947$), and (c) columnar phase with $\mu = 6.0$ ($\rho \approx 0.967$). The particles on the four sublattices 1, 2, 3 and 4 are represented by yellow, olive, cyan and orange for type A and by green, red, blue and magenta for type B. The data are for a system of size $L = 300$.

divide the full lattice into four sublattices to characterize different high density phases as shown in Fig. 5(b). At low densities, the system is in a disordered phase. At intermediate densities, there is a solid-like sublattice phase in which one type of particle is preferred over the other and the particles preferentially occupy one of four sublattices. The system breaks both particle-symmetry as well as translational invariance in the sublattice phase. At even higher densities, the phase is a columnar phase, where the particle-symmetry is restored, and the particles preferentially occupy even or odd rows along one of the three directions. This phase has translational order in only one direction. Snapshots of equilibrated configurations of the system in disordered, sublattice and columnar phase are shown in Fig. 6(a), (b) and (c) respectively.

From finite size scaling, we demonstrate that both the transitions are first order in nature. We also show that the simpler system with only one type of particles undergoes a single discontinuous phase transition from a disordered phase to a solid-like sublattice phase with increasing density of particles. These results are in contradiction to earlier studies which found only a single transition [15, 16].

List of Figures

1 Schematic diagram of an interface between two columnar-ordered phases in the square-dimer model. 4

2 Phase diagram of the square-dimer model in (a) activity z-plane and (b) density ρ-plane. 6

3 Schematic diagram of three types of particles in the hard plate model. . . 6

4 Phase diagram of the hard plate model. 8

5 Schematic diagram of a triangular lattice with two types of Y-shaped particles. 8

6 Snapshots of equilibrated configurations of the system of hard Y-shaped particles in disordered, sublattice and columnar ordered phase. 9

1.1 Schematic diagram of mixture of 2×2 squares, 2×1 horizontal and 1×2 vertical dimers on square lattice. 25

1.2 Schematic diagram of Y-shaped particles on triangular lattice. 28

2.1 Snapshot of a typical configuration of the system of hard squares at equilibrium columnar ordered phase in two different representations. 33

2.2 Schematic diagram of a configuration of the system of hard squares in the presence of an interface. 35

2.3 Schematic diagram of a (a) track of width 4 (four rows) with partition function $\Omega_2(\ell,\Delta)$ and (b) track of width 2 (two rows) with partition function $\mathcal{L}(\ell)$. 38

2.4 Diagrammatic representation of the recursion relation obeyed by the generating function $G_1(y)$ defined for a track of width 2. 43

2.5 Diagrammatic representation of the recursion relation obeyed by the generating functions (a) $G_2(y, 0)$ and (b) $G_2(y, 1)$ for a track of width 4. 45

2.6 Diagrammatic representation of the recursion relation obeyed by the partition function $\Omega_2(\ell, \Delta)$ with $\Delta \geq 2$, for a track of width 4. 47

2.7 Diagrammatic representation of the recursion relation obeyed by the partition functions $\Omega_2^{(R)}(\ell, 0)$ and $\Omega_2^{(R)}(\ell, 1)$ for the track of width 4. 49

2.8 Diagrammatic representation of the recursion relation obeyed by the generating function $\widetilde{G}_2(y, 1)$ for a track of width 4. 50

2.9 Diagrammatic representation of the recursion relation obeyed by the partition function $\widetilde{\Omega}_2(\ell, \Delta)$ with $\Delta \geq 2$ for a track of width 4. 51

2.10 The variation of the interfacial tension $\sigma(z)$ with activity z. 53

3.1 Snapshot of a typical equilibrium configuration of a system where the squares at the left boundary are fixed to be on even rows and the squares at the right boundary are fixed to be on odd rows. 58

3.2 A schematic diagram of an interface that has no overhangs. 59

3.3 The shape of a generic track of two rows. 59

3.4 Diagrammatic representation of the recursion relations obeyed by the generating functions $G(y, 0)$ and $G(y, 1)$. 61

3.5 Diagrammatic representation of the recursion relation obeyed by $\Omega(\ell, \Delta)$, the partition function of a track of two rows. 62

3.6 Phase diagram of the square-dimer model in (a) activity z-plane and (b) density ρ-plane. 65

3.7 Schematic diagram of an interface with overhangs. 69

3.8 The two kinds of right overhang in which the first downward step is followed by (a) rightward or (b) leftward step. 70

3.9 Diagrammatic representation of the recursion relation satisfied by the generating function $\widetilde{\omega}(x)$. 71

3.10 Four possible configurations for each right overhang. 72

3.11 Schematic diagram of two ways of taking two downward steps before the beginning of an left overhang. 74

3.12 Variation of of $\chi/L^{7/4}$ with activity of squares $z_s^{1/4}$ for fixed activity of dimer $z_d = 0.031$ for different system sizes. 79

4.1 Schematic diagram of three types of particles: x-plate y-plate and z-plate having normals along three principal directions of the cubic lattice in hard plate model. 83

4.2 Schematic diagram of (a) sixteen possible morphologies and (b) eight possible states, that are used to construct the transfer matrix. 86

4.3 Division of the full lattice into eight sublattices $0, 1, \ldots, 7$, depending on whether each coordinate is odd or even. 87

4.4 Snapshot of cross sections of equilibrated layered phase. 89

4.5 Temporal evolution of three particle densities and eight sublattice densities for the system of hard plates in the layered phase. 91

4.6 Snapshot of cross sections of equilibrated sublattice phase. 92

4.7 Temporal evolution of eight sublattice densities and order parameters q_2, q_3 for the system in the sublattice phase. 94

4.8 Temporal evolution of eight sublattice densities in the sublattice phase for activity of each plate $z_s = 0.460$ and system size $L = 120$. 95

4.9 Variation of (a) translational order parameters q_1, q_2, q_3, and (b) nematic order parameter q_n with activity of plate z_s. 96

4.10 Data for different thermodynamic quantities near the disordered-layered transition. 98

4.11 Data for different thermodynamic quantities near the layered-sublattice transition. 99

4.12 Schematic phase diagram of the hard plate model. 101

5.1 (a) Schematic diagram of a triangular lattice with two types of Y-shaped particles. (b) The lattice sites are labeled as $1, 2, 3, 4$ depending on the sublattice they belong to. 105

5.2 Schematic diagram to illustrate the sliding move. 106

5.3 The increase in density ρ to its equilibrium value for the algorithms with and without the sliding move. 107

5.4 Snapshot of typical equilibrated configurations of the system in (a) disordered phase and (b) sublattice phase when only one type of particles are present. 109

5.5 Plot of different thermodynamic quantities near disordered-sublattice transition when only one type of particles are present. 111

5.6 Two dimensional density plots of $P(\mathbf{Q^B})$ for different values of μ_B near the transition. 112

5.7 Snapshot of a typical equilibrated configuration of the system obtained from *canonical* Monte Carlo simulations with one type of particle having fixed density $\rho^B = 0.740$. 113

5.8 (a) Schematic diagram showing the creation of a vacancy consisting of four empty sites, when a particle is removed from the fully packed sublattice phase. (b) The vacancy may be split into two half-vacancies, and separated along a row by sliding particles along the row and changing the type. 115

5.9 Snapshots of equilibrated configurations of the system with two types of particles in (a) disordered, (b) sublattice and (c) columnar phase. 116

5.10 Plot of different thermodynamic quantities near disordered-sublattice transition when two types of particles are present. 118

5.11 Plot of different thermodynamic quantities near sublattice-columnar transition when two types of particles are present. 121

5.12 Schematic diagrams to calculate, in a fully packed sublattice phase of *B*-type particles, the energy cost to create two separated half-vacancies. . . . 125

5.13 Schematic diagrams of configurations on a honeycomb lattice when: (a) no vacancy is present, (b) four bound vacancies are created, and (c) eight unbounded vacancies are created. 127

List of Tables

1 Estimates of critical activity z_c and critical density ρ_c for columnar-disordered transition of the hard square model. 3

1.1 Previous estimates of critical activity z_c and critical density ρ_c for columnar-disordered transition of the hard square model. 24

Chapter 1

Introduction

Understanding different phases and phase transitions in thermodynamic systems is one of the central problems of Statistical Physics. A phase transition is a sudden change in physical properties of matter with a small change in a control parameter such as temperature, chemical potential, pressure, etc. The changes may be smooth or abrupt depending on the values of the control parameters as well as the interactions in the system. It also depends on the symmetry of the system and the dimension. There are two types of phase transitions observed in nature. These are discontinuous or first order transition and continuous or second order transition. The nature of phase transition is determined by observing the behavior of the order parameter near the transition. The order parameter is mainly used to capture the visible order or symmetries present in the system. It is zero in the disordered phase and takes non-zero values only in the ordered phase. For first order transitions, the order parameter show discontinuity at the critical point. Both disordered and ordered phases coexist at the critical point resulting a finite value of the correlation length. On the other hand, for second order phase transitions while going from disordered to ordered phase, the order parameter increases continuously from zero to non-zero values. In this case, the correlation length diverges at the critical point. One of the well-known examples of phase transitions that are observed in nature is liquid–solid transition, where density is used as order parameter. Since the density exhibits a discontinuous jump while going from liquid phase to solid phase, the liquid–solid transition is first order in nature.

For the continuous transitions, the scaling behavior obeyed by different thermodynamic quantities, like susceptibility, compressibility, etc., near the transition point are characterized by critical exponents. Although the microscopic properties of two different systems may vary, their critical exponents will be unique if they have same universality class. The universality does not depends on the microscopic details of the system, it only depends on the underlying symmetries present in the system.

1.1 Entropy driven phase transitions

In a thermodynamic system, at constant volume and temperature T, the equilibrium phase is obtained by minimizing the Helmholtz free energy, $F = E - TS$, where E is the internal energy and S is the entropy. Entropy is often regarded as the measure of randomness or disorder in the system. Usually the ordered phase has less entropy than the disordered phase, and the phase transitions from a disordered phase to a ordered phase are driven by lowering the internal energy that outweigh the loss in entropy. These transitions are often referred as the energy driven phase transitions. Examples of energy driven phase transitions include paramagnetic–ferromagnetic transition, gas-liquid transition, etc. However, there are many examples for which the opposite is true, i.e., ordered phase has more entropy compared to the disordered phase. The phase transitions from disordered to ordered phase are driven by gain in entropy, and are often referred as entropy driven phase transitions. Well-known examples of entropy driven phase transitions include liquid–solid transition, disordered–nematic–smectic transition in the system of long rods, freezing transition in the system of hard spheres, etc.

Entropy driven phase transitions for the system of differently shaped particles have been observed in experiments. Examples of these are as follows. The system of spherical particles of PMMA (poly methyl methacrylate) shows freezing transition from fluid phase to crystalline phase with increasing particle density [17]. The system of Brownian square plates undergoes multiple entropy driven phase transitions from low density isotropic phase to intermediate density hexagonal rotator crystal phase to high density rhombic crystal phase [18]. Phase transitions to a smectic or nematic phase in the colloidal solution of tobacco mosaic virus [19], *fd* virus [20], rod-like silica colloids [21] and boehmite colloids [22], banana shaped molecules [23], etc. are also observed in experiments. Ordering transition in adsorbed layer of gas particles on metal surface [24, 25] is another example of entropy driven phase transition.

System of differently shaped particles with only hard core or excluded volume interaction serve as minimal models to study entropy driven phase transitions. Since the interaction energy between two particles are zero in hard core models, every allowed configurations have equal energy and temperature does not play any role. The phases and phase transitions, if any, depends on the shape and density of the particles, and are completely entropy driven. Hence, they are often been termed as geometrical phase transitions. Despite simplicity, the models can recreate the complicated phases observed in experiments, where there are other interactions than excluded volume interactions. For example, the disordered–nematic transition in the system of colloidal long rods was first shown by Onsager [26]. Likewise the discontinuous transition from liquid phase to solid phase in hard spherical particles of PMMA [17] may be modeled as the system of hard spheres that undergoes transition from liquid to crystalline phase with increasing particle density [27]. Various complex phases, e.g., liquid, nematic, smectic, etc., that are often observed in liquid-crystals, may be reproduced by studying the system of hard rods or sphero-cylinders [28, 29]. The phases observed in system of Brownian hard squares [18] may be obtained by studying the Monte Carlo simulation of rounded hard square [30].

Hard core models find applications in self-assembly [31, 32, 33], effectiveness of drug delivery [34, 35], design of novel materials with specific optical and chemical properties [36, 37, 38], adsorption of gas on metallic surfaces [24, 39, 40], molecular logic gates [41, 42, 43], etc.

Hard core models in lattice, also known as hard core lattice gas (HCLG) models are discrete version of hard exclusion models. In HCLG models, particles sit on lattice sites and interact only through excluded volume interaction. Unlike the continuum models, the ordered phase of HCLG models have discrete symmetry. Although the interaction is simple, HCLG models exhibit different broken-symmetry phases like solid-like sublattice order, columnar or smectic phase with partial translational order, and nematic phase with orientational order, depending on the particle shape. The study of the phases and critical behavior of lattice systems of hard particles having different geometrical shapes has been of continued interest in classical statistical mechanics, not only from the point of view of how complex phases arise from simple interactions, but also for understanding how different universality classes of continuous phase transitions depend on the shape of the particles. Such HCLG models have also been of interest in the context of the freezing transition [44, 45], directed and undirected lattice animals [46, 47, 48], the Yang-Lee edge singularity [49], and in absorption of molecules onto substrates [50, 39, 51, 52, 25].

HCLG models, specially the models in two dimensions have a long and detailed history. The model was first introduced in 1958 to demonstrate the melting transition [53]. After that, full packing of dimer model in which each particle occupies 1×2 or 2×1 sites on the square lattice, was rigorously solved using combinatorial method in 1961 [54]. The model [54, 55, 56, 57, 58, 59] is the simplest model for anisotropic particles that has exact solution in the fully packed limit. In this limit, the system is critical and the correlations between dimers decay with separation r as r^{-2} [56]. At densities different from the fully packed limit, the system is disordered [57, 59]. Soon after that the existence of phase transition in hard square model in which each particle exclude up to second nearest neighbor on square lattice, was numerically shown in 1966 [60]. Later the exact solution of the hard hexagon model on triangular lattice came in 1980 [61]. This is the only exactly solved HCLG model. Different geometrical shapes have been studied in literature, which include triangles [62], squares [1, 60, 63, 2, 7, 64], dimers [54, 55, 58, 65], trimers [66], tetrominoes [67, 68], mixture of squares and dimers [8, 69], Y-shaped molecules [16], rods [70, 71, 13, 14], rectangles [72, 73, 74, 75], cubes [76], discs [3, 77], and hexagons [61].

Although, there are a large number of studies of HCLG models, it is not clear what is the exact dependence between the shape of the particles and the emergent phase is. In this thesis, we have studied four different types of particles both in two and three dimensions, which are: (1) hard 2×2 squares on square lattice, (2) mixture of hard 2×2 squares, horizontal and vertical dimers on square lattice, (3) hard $2 \times 2 \times 1$ hard plates on cubic lattice and (4) hard Y-shaped particles on triangular lattice. Below, we summarize what is known about these models, and the new results obtained in this thesis.

1.2 Hard square lattice gas

The hard square model [1, 60, 63, 2, 7, 64] in which each particle occupies 2×2 sites on the square lattice is the prototypical model to show columnar order. The model is equivalent the 2-NN model in which a particle excludes the nearest and next-nearest neighbor from being occupied by another particle. It is a well-studied HCLG model, which undergoes a continuous transition from disordered to columnar phase with increasing particle density. The continuous transition belongs to the Ashkin-Teller universality class with the correlation length exponent $\nu \approx 0.92$ [10, 9, 8]. Ashkin-Teller model is a spin model in which two Ising spins are coupled through a variable interaction strength. The Hamiltonian H of the Ashkin-Teller model may be written as

$$H = \sum_{\langle i,j \rangle} J_1 \sigma_i \sigma_j + \sum_{\langle i,j \rangle} J_2 \tau_i \tau_j + \sum_{\langle i,j \rangle} J_3 \sigma_i \sigma_j \tau_i \tau_j, \tag{1.1}$$

Table 1.1: Previous estimates of critical activity z_c and critical density ρ_c for columnar-disordered transition of the hard square model.

z_c	ρ_c	Method Used
97.50	0.932	Numerical [3, 8, 9, 10]
6.25	0.64	High density expansion (order one) [2, 1]
11.09	0.76	Flory type mean field [11]
11.09	0.76	Approximate counting [12]
11.13	0.764	Density Functional theory [4, 5]
14.86	0.754	High density expansion (order two) [2]
17.22	0.807	Rushbrooke Scoins approximation [1]
48.25	0.928	Interfacial tension with no defect [7]
52.49	0.923	Interfacial tension with one defect [7]
54.87	0.9326	Interfacial tension with overhang [7]
135.63	-	Interfacial tension in antiferromagnetic Ising model [6]

where σ_i and τ_i are Ising spins at site i and Js are the interaction strength. The model has a line of critical points with continuously varying critical exponents. The hard square system has found application in modeling adsorption [50, 25], in combinatorial problems and tilings [78, 79, 80], and has been the the subject of recent direct experiments [18, 81].

In the high density columnar phase, the squares preferentially occupy either even or odd rows or even or odd columns, thus breaking translational order in only one of the two directions. The columnar phase has four-fold symmetry. The study of entropy driven transition in the hard square lattice gas model has a long history [53, 1, 27, 82, 83, 84, 85]. Since the model can not be solved exactly, different sophisticated analytic and rigorous methods have been used to estimate the critical parameters over the last few decades [1, 60, 2, 4, 5, 6, 7, 3, 12]. The best numerical estimates of the critical parameters, obtained from large scale Monte Carlo simulations, are critical activity $z_c \approx 97.5$, critical density $\rho_c \approx 0.932$. The estimates for z_c and ρ_c obtained from different methods are summarized in Table 1.1. Analytical approaches like high density expansion [1, 2], Flory-type approximations [3], density functional theory [4, 5] etc., underestimate the critical activity by more than a factor of 7 compared to the numerical Monte Carlo result $z_c \approx 97.5$ and $\rho_c \approx 0.932$. The calculations based on estimating the interfacial tension [6, 7] between

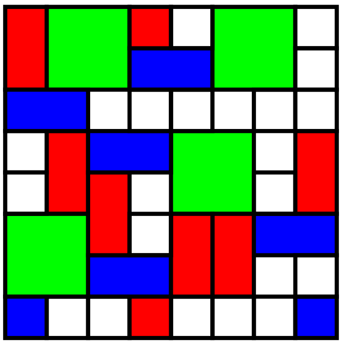

Figure 1.1: Schematic diagram of mixture of 2×2 squares, 2×1 horizontal and 1×2 vertical dimers on square lattice with periodic boundary along horizontal and vertical directions.

two ordered phases have been more successful, but the error in estimating the activity is still about 50%.

Questions addressed

Previous estimates of the critical activity have an error of nearly 50%. Can a more accurate estimate be found? In particular, for determining the interfacial tension, can the effect of multiple defects and overhangs be incorporated?

1.3 Mixture of hard squares and dimers

Polydispersity can hardly be avoided in experiments. However, compared to the monodispersed systems, the phenomenology of HCLG models of mixtures of particles of different shapes is less understood. Amongst mixtures, the best studied example is that of depletion interaction in mixtures of particles with small excluded volume and particles with larger excluded volume. When the excluded volumes are on site and first nearest neighbor, then in two dimensions, it is known from different numerical studies that there is a critical line ending in a tricritical point separating a low-density disordered fluid-like phase from a high-density solid-like sublattice phase [86, 87, 88, 89, 90, 91]. The nature of the transition is similar to that of the transition observed in the system with only larger particles. Similar demixing transition occurs in binary mixture of large and small cubes [91, 92, 4]. Other examples of mixtures that have been studied on lattices include bidispersed rods [93, 94] in which the phase diagram is richer than the monodispersed case, but without the appearance of any new phase.

The hard square lattice gas model may be generalized to a mixture of squares and dimers. In this model, a mixture of hard 2×2 squares, 2×1 horizontal dimers, 1×2 vertical dimers and 1×1 vacancies co-exist on a $L_x \times L_y$ square lattice. Schematic diagram of the square-dimer model is shown in Fig. 1.1. In a recent paper [8], a mixture of hard squares and dimers was studied. Very interestingly, it was demonstrated that the phase diagram consists of two critical lines with continuously varying exponents that meet at a point called as the Askin-Teller-Kosterlitz-Thouless point. It provided the first example of a HCLG whose critical properties vary with the composition. On the fully packed line, it was shown that the system undergoes a Korterlitz-Thouless type transition from a columnar phase to a power law correlated phase as the dimer density is increased.

Questions addressed

Along the fully packed line, the configurations of dimers and squares may be mapped onto a height field. By writing an effective Hamiltonian for the two dimensional height field, it is possible to theoretically explain the numerically obtained results, along the fully packed line [8]. However, the height mapping does not allow the phase boundary to be determined in the presence of vacancies, as the relation between the rigidity and microscopic parameters is not easy to establish. Is it possible to estimate the phase boundary separating the disordered and columnar phase by calculating the interfacial tension between two differently ordered columnar phase? If possible, how close are the estimates to the Monte Carlo results?

1.4 Hard plates on a cubic lattice

The generalization of square to three dimensions is the problem of hard $2 \times 2 \times 1$ plates on a cubic lattice. Three types of plates are possible: x-plate, y-plate and z-plate, having normals along the three principal directions of the cubic lattice. Recently analytical as well as numerical studies have been performed to get the phase diagram for the system of hard plates with varying aspect ratio in continuum. For example, rigorous calculation using coarse graining procedure proves the existence of nematic phase in the system of anisotropic $1 \times k^{\alpha} \times k$, $\alpha \in [0, 1]$ hard plates [95] in three dimensional continuum. In this model only restricted number of particle configurations are allowed. Numerical studies of the system of board-like particles [96, 97, 98] in the continuum indicate the presence of various high density phases like smectic, biaxial smectic, uniaxial and biaxial nematic, prolate and oblate columnar, etc. The phase diagram of the system is very rich, showing multiple phase transitions with changing particle densities and varying aspect ratios.

Comparatively less is known about the HCLG models in three dimensions. Detailed phase diagram that encompasses all densities is known for only rods of shape $k \times 1 \times 1$ [14, 13]. The system of hard rods shows multiple entropy driven phase transitions with increasing particle densities. For $k \geq 7$, numerically observed phase transitions are isotropic to nematic to layered-nematic to layered-disordered. In layered-nematic phase, system breaks up into layers, with nematic order in each layer. In the layered-disordered phase, unlike the layered-nematic phase, the rods within a plane, perpendicular to the layering direction, do not have nematic order.

The numerical study of HCLG models are constrained by difficulties of equilibrating the system when the density is close to full-packing, and/or the volume excluded by each particle is large. These constraints may be overcome by using Monte Carlo algorithms that include cluster moves [72, 73, 8], which significantly decrease the autocorrelation times.

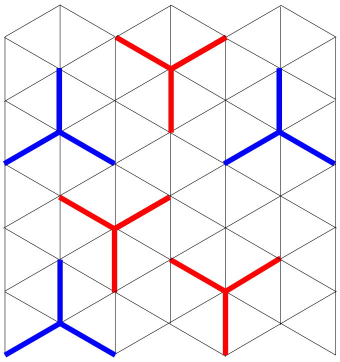

Figure 1.2: Schematic diagram of Y-shaped particles on triangular lattice with periodic boundary along three directions.

Questions addressed

Can a Monte Carlo algorithm be implemented that is able to equilibrate the system even at full packing? What is the phase diagram of the system of hard plates on a cubic lattice?

1.5 Hard Y-shaped particles

Y-shaped particles with this shape arise in different contexts. A well known example is Immunoglobulin-G (IgG), an antibody present in human blood, consisting of four peptide chains, two identical heavy chains and two identical light chains [99]. IgG has many therapeutic usages and study of different phases of Y-shaped particles [15, 100, 16] is important to understand the effect of density on the viscosity of the liquid. Another example of a Y-shaped particle that is relevant for applications is trinaphthylene. It has been useful to create a NOR logic gate on Au(111) surface [101, 102], in which napthylene branches of the molecule comes in contact of Au atom and act as input of logic gate.

Motivated by these applications, there have been a few numerical studies [16, 15] of systems of Y-shaped particles on a triangular lattice. Each particle constitutes of a central site and three of its nearest neighbors chosen alternately. There are two types of particles possible depending on which of the neighbors are chosen. Schematic diagram of the system of Y-shaped particles is shown in Fig. 1.2. In Refs. [16, 15], in addition to the hard core constraint, there are additional attractive interactions between the arms of neighboring particles. At low temperatures, a single first order phase transition from a disordered phase to a high-density ordered phase was observed. The high density phase consists of mostly only one of the two types of Y-shaped particles, and has a solid-like sublattice order. For temperatures above a critical temperature, there are no density-driven phase transitions [16, 15]. At the critical temperature, the transition has been argued to belong to the Ising universality class [16]. For Y-shaped particles with larger arm lengths, other phases are also seen [15].

Questions addressed

Is there any phase transition in hard core limit for the system of Y-shaped particles on triangular lattice with arm length one, if yes, what are the equilibrium phases and the nature of transitions?

1.6 Overview of the thesis

We have used sophisticated analytical techniques as well as large-scale Monte Carlo simulations to study these systems. The results that have been obtained in this thesis are summarized below.

In Chapter 2, we estimate the transition point separating the disordered phase and columnar phase in the system of hard 2×2 squares by calculating the interfacial tension separating two differently ordered columnar phase and equating it to zero. The obtained result improves previous estimates of critical activity and is the best estimate till date.

In Chapter 3, we consider mixture of 2×2 hard squares and dimers on square lattice. We have estimated the phase boundary separating the disordered and columnar phase using the interfacial tension method. The results show good agreement with Monte Carlo results.

In Chapter 4, we extend the system of hard squares to three dimensions. We consider system of $2 \times 2 \times 1$ square plates in cubic lattice. Three types of plates are possible, x-plate, y-plate and z-plate, having normals along x, y and z directions respectively. Particles interact only through excluded volume interaction. Using transfer matrix based Monte Carlo simulations, we have shown that the system undergoes two entropy driven phase transitions with increasing particle density. At low density the system is in disordered phase, with increasing density the system goes to a layered phase breaking translational symmetry along one of the three possible directions. At very large density, even at full packing, the equilibrium phase is sublattice ordered. In sublattice phase the system breaks translational invariance along all three directions.The nature of the phase transitions are characterized in detail.

In Chapter 5, we consider the system of hard Y-shaped particles on triangular lattice. Two types of particles are possible which are mirror images of each other. Performing grand canonical Monte Carlo simulation, we have shown that the system undergoes two entropy driven phase transitions with increasing particle density, when both types of particles are present. These are transition from disordered to sublattice phase and transition from sublattice to columnar ordered phase. Using finite size scaling, We have also shown that both transitions are discontinuous in nature. The simplified system of Y-shaped particles, when only one type of particles are present, shows a single discontinuous transition from disordered phase to sublattice phase.

In Chapter 6, we summarize the obtained results and give future outlook.

Chapter 2

Hard square lattice gas

2.1 Introduction

In this chapter, we describe the hard square lattice gas model and estimate the critical activity of the hard square model by calculating the interfacial tension between two differently ordered columnar phases. The hard square model is known to undergo a continuous transition from a disordered fluid-like phase to an ordered phase with columnar order as the density ρ or activity z is increased. The best numerical estimates for the critical behavior, obtained from large scale Monte Carlo simulations, are critical activity $z_c \approx 97.5$, critical density $\rho_c \approx 0.932$, and critical exponents belonging to the Ashkin Teller universality class with critical exponents $\nu \approx 0.92$, $\beta/\nu = 1/8$ and $\gamma/\nu = 7/4$ [3, 8, 9, 10]. Unlike the hard hexagon model [103], the hard square model is not exactly solvable. Different analytic and rigorous methods have been used to estimate the critical parameters over the last few decades [1, 60, 2, 4, 5, 6, 7, 3, 12]. The estimates for z_c and ρ_c obtained from different methods are summarized in Table 1.1. Analytical approaches like high density expansion [1, 2], Flory-type approximations [3], density functional theory [4, 5], etc., result in estimates that underestimate the critical activity by more than a factor of 7. Calculations based on estimating the interfacial tension [6, 7] between two ordered phases have been more successful. By utilizing the mapping of the hard square model to the antiferromagnetic Ising model with next nearest neighbor interactions, a fairly good estimate $z_c = 135.63$, that overestimates the critical activity, was obtained, but it is not clear how this approach may be extended [6]. In a recent paper [7], we introduced a systematic way of determining the interfacial tension as an expansion in number of defects in the perfectly ordered phase. While including a single defect improves the estimates for the critical parameters ($z_c = 52.49$), the calculation of the two-defect contribution appears to be too difficult to carry out. We also estimated the effect of introducing overhangs of height one in the interface for defect-free phases ($z_c = 54.87$). However, it is not clear how defects and overhangs may be combined in a single calculation. In this chapter, we determine the interfacial tension using a pairwise approximation [104, 105], similar to that used in liquid state theory. This approximation scheme allows us to take into account multiple defects as well as overhangs. By determining the activity at which this interfacial tension vanishes, we estimate $z_c = 105.35$, in reasonable agreement with numerical results ($z_c \approx 97.5$), and which is a significant improvement over earlier estimates. The content of this chapter is published in Ref. [64].

2.2 Model and Outline of Calculation

Consider a square lattice of size $N_x \times N_y$. The sites may be occupied by particles that are hard squares of size 2×2. The squares interact through only excluded volume interaction i.e. two squares can not overlap but may touch each other. We associate an activity z to each square.

At low activities z or equivalently at low densities ρ, the system is in a disordered phase. For activities larger than critical value z_c, the system is in a broken-symmetry phase with columnar order, which we define more precisely below. Let the lower left corner of a square be denoted as its head. In the columnar phase, the heads preferentially occupy

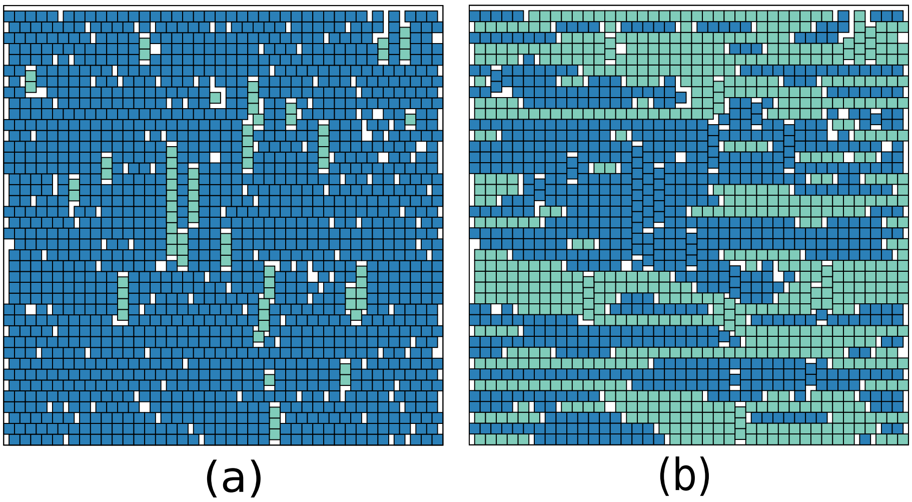

Figure 2.1: Snapshot of a typical configuration of the system of hard squares at equilibrium in two different representations. The data are for activity $z = 110$, when the density is $\rho \approx 0.937$, and the system is in an ordered phase. A square is colored blue or green depending on whether its head (bottom left point) is in even or odd (a) row and (b) column. The dominance of one color in (a) implies that the system is a row-ordered phase. The snapshot was generated using Monte Carlo simulation by implementing the cluster algorithm introduced in [106, 71].

even or odd rows with all columns being equally occupied, or preferentially occupy even or odd columns with all rows being equally occupied. An example of a row-ordered phase is shown in Fig. 2.1. The snapshot of a equilibrated configuration is shown in two different representations. When the squares are colored according to whether their heads are in even or odd rows [see Fig. 2.1(a)], one color is predominantly seen. However, when the same configuration is colored according to whether the heads of the squares are in even or odd columns [see Fig. 2.1(b)], then both colors appear in roughly equal proportion. There are clearly 4 ordered phases possible.

The aim of this paper is to estimate the critical activity z_c and critical density ρ_c separating the disordered phase from the ordered columnar phase. To do so, we determine, within an approximation scheme, the interfacial tension $\sigma(z)$ between two differently ordered columnar phases and equate it to zero to obtain the transition point. Consider boundary conditions where the left edge of the square lattice is fixed to the occupied by squares with heads in even row and the right edge is fixed to be occupied by squares in odd row. For large z, this choice of boundary condition ensures that there is an interface running from top to bottom separating a left phase or domain constituted of squares predominantly in even rows from a right phase or domain constituted of squares predominantly in odd rows. A schematic diagram of the interface is shown in Fig. 2.2. We will refer to the two phases as left and right phases or domains from now on. Let $Z^{(0)}$ be the partition functions of the system without an interface and $Z^{(\mathcal{I})}$ be the partition function when an specified interface $\mathcal{I}$ is present. The interfacial tension $\sigma(z)$ is defined as

$$e^{-\sigma N_y} = \frac{\sum_{\mathcal{I}} Z^{(\mathcal{I})}}{Z^{(0)}}. \tag{2.1}$$

As the interactions between the squares are only excluded volume interactions, the partition function in the presence of an interface may be written as a product of partition function of the left and right phases, i.e.

$$Z^{(\mathcal{I})} = Z_L^{(\mathcal{I})} Z_R^{(\mathcal{I})}, \tag{2.2}$$

where $Z_L^{(\mathcal{I})}$ and $Z_R^{(\mathcal{I})}$ denote the partition functions of the left and right phases in the presence of an specified interface $\mathcal{I}$. It is not possible to determine $Z_L^{(\mathcal{I})}$, $Z_R^{(\mathcal{I})}$ or $Z^{(0)}$ exactly. In what follows, we calculate these partition functions within certain approximations.

First, we assume that the interface between the left and right phases is a directed walk from top to bottom, i.e. the interface does not have any upward steps. We define the position of the interface to be the right boundary of the rightmost squares of the left phase. The interface is specified by its x-coordinates, η_i as shown in Fig. 2.2. We also define ξ_i to be the x-coordinates of the left most position that a square in the right phase may occupy on row i, as shown in Fig. 2.2. Clearly,

$$\xi_i = \max(\eta_{i-1}, \eta_i), \quad i = 1, 2, .., N_y/2. \tag{2.3}$$

Given an interface, we compute the partition function within an approximation. The simplest approximation is it to write the partition function as a product of partition functions

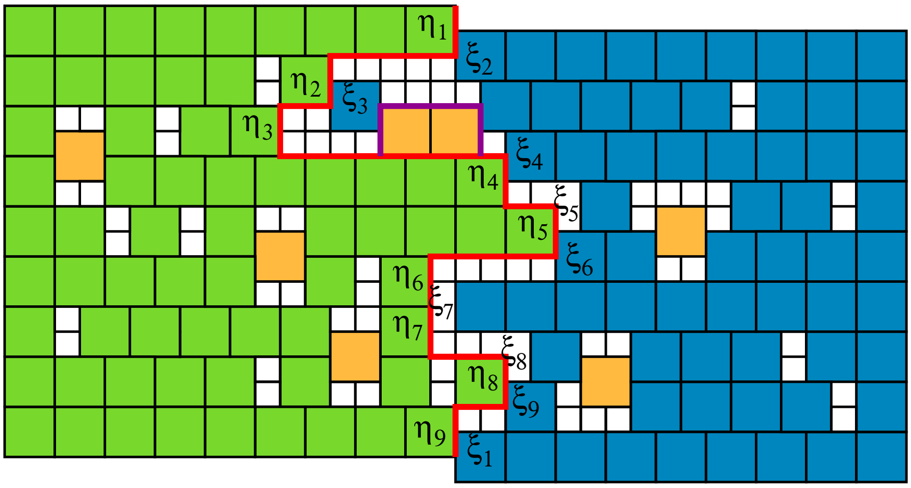

Figure 2.2: Schematic diagram of a configuration in the presence of an interface. The boundary conditions are such that the left (right) edge of the square is fixed to be occupied by even (odd) squares. The interface, constituted of the right edges of the right-most squares of the left domain is denoted by the red line and its x-coordinates are labeled by η_i. ξ_i denotes the x-coordinate of the left-most position possible for a square belonging to the right domain. An overhang of height one in the interface is denoted by magenta line.

of tracks of width two, corresponding to two consecutive rows. This approximation has the drawback that the ordered left and right phases do not have any defects, where the squares of wrong type i.e. odd squares in left or even phase and even squares in the right or odd phase will be called defects (denoted by yellow in Fig. 2.2). The calculation of interfacial tension then reduces to the special case of zero-defects of [7]. The simplest approximation that allows defects to be present is the pairwise approximation [104, 105]. Here, we approximate the the full partition function of N_y rows as a product over partition function of tracks made up of four consecutive rows, suitably scaled to avoid overcounting. We write

$$Z_L^{(\mathcal{I})} \approx \frac{\omega_2^{(L)}(\eta_1,\eta_2)\omega_2^{(L)}(\eta_2,\eta_3)\ldots\omega_2^{(L)}(\eta_{N_y/2},\eta_1)}{\mathcal{L}^{(L)}(\eta_1)\mathcal{L}^{(L)}(\eta_2)\ldots\mathcal{L}^{(L)}(\eta_{N_y/2})}, \tag{2.4}$$

$$Z_R^{(\mathcal{I})} \approx \frac{\omega_2^{(R)}(N_x-\xi_1,N_x-\xi_2)\ldots\omega_2^{(R)}(N_x-\xi_{N_y/2},N_x-\xi_1)}{\mathcal{L}^{(R)}(N_x-\xi_1)\ldots\mathcal{L}^{(R)}(N_x-\xi_{N_y/2})}, \tag{2.5}$$

$$Z^{(0)} \approx \frac{[\omega_2(N_x,N_x)]^{N_y/2}}{[\mathcal{L}(N_x)]^{N_y/2}}, \tag{2.6}$$

where $\omega_2(\ell_1,\ell_2)$ is the partition function of a track of width 4 where first two rows are of length ℓ_1 and third and fourth rows of length ℓ_2, and $\mathcal{L}(\ell)$ is the partition function of a track of width 2 where both rows have length ℓ. The superscripts (L) and (R) denote left and right phases. The choice of the denominator is motivated by the fact that in the absence of defects, $\omega_2(\ell_1, \ell_2) = \mathcal{L}(\ell_1)\mathcal{L}(\ell_2)$. In this case, the overall partition function should reduce to a product over $\mathcal{L}$'s, and the choice of the denominator ensures this. The exponent $N_y/2$ in eq. (2.6) follows from the fact that though there are N_y rows, in the columnar phase, the heads are either in even or odd rows resulting in $N_y/2$ tracks of width 2.

The partition function of the system having vertical width N_y is effectively the ratio of $N_y/2$ partition functions of tracks of width four, made up of four consecutive rows and $N_y/2$ partition functions of tracks of width two.

The partition functions for the left and right phases are different, and also not the same as the partition function of the system without an interface, because the presence of the interface imposes introduces constraints on the positioning of squares near the interface. The constraints are as follows. For the left partition function $\omega_2^{(L)}(\ell_1, \ell_2)$, there must be even squares (non-defects) present whose right edges are aligned with the position of the interface in both sets of two rows each corresponding to ℓ_1 and ℓ_2. This is because the position of the interface has been defined as the right edge of the rightmost square of the left phase. For the right partition function $\omega_2^{(L)}(\ell_1, \ell_2)$, the constraint is that there must at least one odd square (non-defect) between the interface and the left-most defect square. Otherwise, the interface can be redefined to include the defect square into the left phase. In addition, there is the question of whether defects can be placed between ℓ_1 and ℓ_2 for the left and right phases. Placing defects here is equivalent to allowing the interface to have overhangs. To prevent overcounting, we will disallow such defects for the left phase, but allow them for the right phase. Equivalently, a defect in the left phase may be placed only in the region to the left of $\min(\ell_1, \ell_2)$, and a defect in the right phase can be placed to the right of $\min(N_x - \ell_1, N_x - \ell_2)$.

It is convenient to shift to a notation where (see Fig. 2.3)

$$\omega_2(\ell_1, \ell_2) = \Omega_2[\min(\ell_1, \ell_2), |\ell_1 - \ell_2|] \tag{2.7}$$

Then, the partition function $Z^{(L)}$, $Z^{(R)}$ and $Z^{(0)}$ may be rewritten as

$$\begin{aligned}
Z_L^{(\mathcal{I})} &= \frac{\prod_{i=1}^{N_y/2} \Omega_2^{(L)}[\min(\eta_i, \eta_{i+1}), |\eta_i - \eta_{i+1}|]}{\prod_{i=1}^{N_y/2} \mathcal{L}^{(L)}(\eta_i)}, && (2.8)\\
Z_R^{(\mathcal{I})} &= \frac{\prod_{i=1}^{N_y/2} \Omega_2^{(R)}[N_x - \max(\xi_i, \xi_{i+1}), |\xi_i - \xi_{i+1}|]}{\prod_{i=1}^{N_y/2} \mathcal{L}^{(R)}(N_x - \xi_i)}, && (2.9)\\
Z^{(0)} &= \frac{[\Omega_2(N_x, 0)]^{N_y/2}}{[\mathcal{L}(N_x)]^{N_y/2}}, && (2.10)
\end{aligned}$$

For large ℓ, the partition functions Ω_2 and $\mathcal{L}$ diverge exponentially with the system size. We define

$$\begin{aligned}
\Omega_2(\ell, \Delta) &= a_2(\Delta)\lambda_2^{2\ell+\Delta}, && (2.11)\\
\Omega_2^{(L)}(\ell, \Delta) &= a_2^{(L)}(\Delta)\lambda_2^{2\ell+\Delta}, \quad \ell \gg 1, && (2.12)\\
\Omega_2^{(R)}(\ell, \Delta) &= a_2^{(R)}(\Delta)\lambda_2^{2\ell+\Delta}, && (2.13)
\end{aligned}$$

and

$$\begin{aligned}
\mathcal{L}(\ell) &= a_1\lambda_1^{\ell}, && (2.14)\\
\mathcal{L}^{(L)}(\ell) &= a_1^{(L)}\lambda_1^{\ell}, \quad \ell \gg 1, && (2.15)\\
\mathcal{L}^{(R)}(\ell) &= a_1^{(R)}\lambda_1^{\ell}. && (2.16)
\end{aligned}$$

Note that we have used the same exponential factor for all Ω_2 (as well as for all $\mathcal{L}$), since the free energy is independent of constraints arising from the boundary conditions. It is easy to determine $a_1^{(L)}$ and $a_1^{(R)}$ in terms of a_1. In the left domain, for a track of width 2, the constraint is that the rightmost square must touch the interface. This means that $\mathcal{L}^{(L)}(\ell) = z\mathcal{L}(\ell - 2) \approx za_1\lambda_1^{\ell-2}$. In the right domain, defects cannot be present in a track

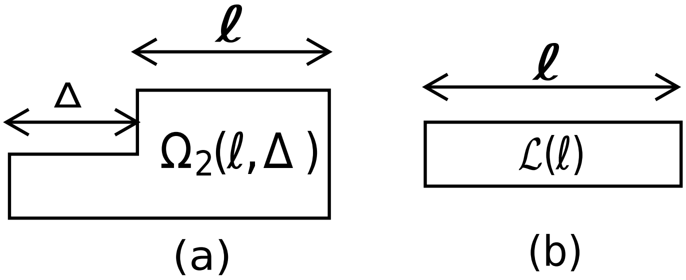

Figure 2.3: Schematic diagram of a (a) track of width 4 (four rows) with partition function $\Omega_2(\ell,\Delta)$ and (b) track of width 2 (two rows) with partition function $\mathcal{L}(\ell)$.

of width 2, and hence there are no constraints, implying that $\mathcal{L}^{(R)}(\ell) = \mathcal{L}(\ell) \approx a_1\lambda_1^{\ell}$. Therefore,

$$\begin{aligned} a_1^{(L)} &= \frac{za_1}{\lambda_1^2}, && (2.17)\\ a_1^{(R)} &= a_1. && (2.18) \end{aligned}$$

Using the asymptotic forms for the partition functions, the partition functions of the left [see eq. (2.8)] and right [see eq. (2.9)] phases may be rewritten as

$$\begin{aligned} Z_L^{(\mathcal{I})} &= \frac{\prod_{i=1}^{N_y/2} a_2^{(L)}(|\eta_i-\eta_{i+1}|)\lambda_2^{2\min(\eta_i,\eta_{i+1})+|\eta_i-\eta_{i+1}|}}{\prod_{i=1}^{N_y/2} za_1\lambda_1^{\eta_i-2}}, && (2.19)\\ Z_R^{(\mathcal{I})} &= \frac{\prod_{i=1}^{N_y/2} a_2^{(R)}(|\xi_i-\xi_{i+1}|)\lambda_2^{2N_x-2\max(\xi_i,\xi_{i+1})+|\xi_i-\xi_{i+1}|}}{\prod_{i=1}^{N_y/2} a_1\lambda_1^{N_x-\xi_i}}. && (2.20) \end{aligned}$$

Using the relations $2\min(m,n) = m+n-|m-n|$ and $2\max(m,n) = m+n+|m-n|$, taking product of $Z^{(L)}$ and $Z^{(R)}$ and simplifying, we obtain

$$Z^{(\mathcal{I})} = \frac{\lambda_2^{N_xN_y}\prod_{i=1}^{N_y/2} a_2^{(L)}(|\eta_i-\eta_{i+1}|)a_2^{(R)}(|\xi_i-\xi_{i+1}|)\lambda_2^{-|\eta_i-\eta_{i+1}|}}{\left(\frac{za_1^2}{\lambda_1^2}\right)^{N_y/2}\lambda_1^{N_xN_y/2}\prod_{i=1}^{N_y/2}\lambda_1^{-\frac{1}{2}|\eta_i-\eta_{i+1}|}}. \qquad (2.21)$$

Likewise, the partition function of the system without an interface [see eq. (2.10)] may be written for large N_x as

$$Z^{(0)} = \left[\frac{a_2(0)\lambda_2^{2N_x}}{a_1\lambda_1^{N_x}}\right]^{N_y/2}. \tag{2.22}$$

Knowing the partition functions eq. (2.21) and eq. (2.22), the interfacial tension in eq. (2.1) may be expressed in terms of a's, λ_1 and λ_2 as

$$e^{-\sigma N_y} = \left[\frac{\lambda_1^2}{z a_1 a_2(0)}\right]^{N_y/2} \sum_{I} \prod_{i=1}^{N_y/2} \frac{a_2^{(L)}(|\eta_i - \eta_{i+1}|)\, a_2^{(R)}(|\xi_i - \xi_{i+1}|)\, \lambda_2^{-|\eta_i-\eta_{i+1}|}}{\lambda_1^{-\frac{1}{2}|\eta_i-\eta_{i+1}|}}. \tag{2.23}$$

We note that all arguments are in terms of differences between consecutive η_i's or ξ_i's. It is therefore convenient to introduce new variables

$$\widetilde{\eta}_i = \eta_i - \eta_{i-1}. \tag{2.24}$$

In terms of these new variables, it is straightforward to derive

$$\xi_{i+1} - \xi_i = \widetilde{\eta}_{i+1}\theta(\widetilde{\eta}_{i+1}) + \widetilde{\eta}_i(1 - \theta(\widetilde{\eta}_i)), \tag{2.25}$$

where $\theta(x)$ is the Heaviside step function defined as $\theta(x) = 1$ for $x \geq 0$ and $\theta(x) = 0$ for $x < 0$. In terms of these new variables $\widetilde{\eta}_i$, the interfacial tension eq. (2.23) may be rewritten as

$$e^{-\sigma N_y} = \left[\frac{\lambda_1^2}{z a_1 a_2(0)}\right]^{N_y/2} \sum_{[\widetilde{\eta}_i]} \prod_{i=1}^{N_y/2} \left(\frac{\sqrt{\lambda_1}}{\lambda_2}\right)^{|\widetilde{\eta}_i|} a_2^{(L)}(|\widetilde{\eta}_i|) \times a_2^{(R)}(|\widetilde{\eta}_{i+1}\theta(\widetilde{\eta}_{i+1}) + \widetilde{\eta}_i(1 - \theta(\widetilde{\eta}_i))|), \tag{2.26}$$

where the sum over $\widetilde{\eta}_i$ varies from $-\infty$ to $+\infty$.

The summation over $\widetilde{\eta}_i$ is not straightforward to do as they are not independent due to terms coupling $\widetilde{\eta}_i$ and $\widetilde{\eta}_{i+1}$. To do the sum, we define an infinite dimensional transfer matrix T with coefficients

$$T_{\widetilde{\eta}_i,\widetilde{\eta}_{i+1}} = \left(\frac{\sqrt{\lambda_1}}{\lambda_2}\right)^{|\widetilde{\eta}_i|} a_2^{(L)}(|\widetilde{\eta}_i|)\, a_2^{(R)}(|\widetilde{\eta}_{i+1}\theta(\widetilde{\eta}_{i+1}) + \widetilde{\eta}_i(1-\theta(\widetilde{\eta}_i))|). \tag{2.27}$$

Let Λ_2 be the largest eigenvalue of the transfer matrix T. For large N_y, we may then write eq. (2.26) as

$$e^{-\sigma N_y} = \left[\frac{\lambda_1^2}{z a_1 a_2(0)}\right]^{N_y/2} \sum_{[\widetilde{\eta}_i]} \prod_{i=1}^{N_y/2} T_{\widetilde{\eta}_i,\widetilde{\eta}_{i+1}} = \left[\frac{\lambda_1^2 \Lambda_2}{z a_1 a_2(0)}\right]^{N_y/2}. \tag{2.28}$$

At the transition point, σ vanishes, and the critical activity z_c therefore satisfies the relation

$$\frac{\lambda_1^2 \Lambda_2}{z_c a_1 a_2(0)} = 1, \tag{2.29}$$

where Λ_2 depends on $a_2^{(R)}$ and $a_2^{(L)}$. These unknown parameters are calculated exactly in section 2.3 and section 2.4.

2.3 Calculation of Eigenvalue of *T*

In this section, we determine the largest eigenvalue of the transfer matrix T with components as defined in eq. (2.27). Let the largest eigenvalue of T be denoted by Λ_2 corresponding to an eigenvector Ψ with components ψ_i, $i = -\infty, \ldots, \infty$. In component form, the eigenvalue equation is

$$\sum_{j=-\infty}^{\infty} T_{i,j}\psi_j = \Lambda_2 \psi_i,\ i = -\infty, \ldots, \infty. \tag{2.30}$$

Substituting for T from eq. (2.27), we obtain

$$\left(\frac{\sqrt{\lambda_1}}{\lambda_2}\right)^{|i|} a_2^{(L)}(|i|)\left[a_2^{(R)}(0) \sum_{j=-\infty}^{0} \psi_j + \sum_{j=1}^{\infty} a_2^{(R)}(|j|)\psi_j\right] = \Lambda_2 \psi_i,\ i \geq 0, \tag{2.31}$$

$$\left(\frac{\sqrt{\lambda_1}}{\lambda_2}\right)^{|i|} a_2^{(L)}(|i|)\left[a_2^{(R)}(|i|)\sum_{j=-\infty}^{0}\psi_j + \sum_{j=1}^{\infty} a_2^{(R)}(|j+i|)\psi_j\right] = \Lambda_2\psi_i,\ i < 0. \tag{2.32}$$

First consider the case for $i \geq 0$. Eq. (2.31) may be re-written as

$$\left(\frac{\sqrt{\lambda_1}}{\lambda_2}\right)^{|i|} a_2^{(L)}(|i|)\left[a_2^{(R)}(0)\beta + \sum_{j=1}^{\infty} a_2^{(R)}(|j|)\widetilde{\psi}_j\right] = \Lambda_2\widetilde{\psi}_i,\ i \geq 0, \tag{2.33}$$

where

$$\widetilde{\psi}_i = \frac{\psi_i}{\psi_0};\ \ \beta = \sum_{i=-\infty}^{0}\widetilde{\psi}_i. \tag{2.34}$$

Since $\widetilde{\psi}_0 = 1$, from eq. (2.33) with $i = 0$, we immediately obtain the eigenvalue Λ_2 to be

$$\Lambda_2 = a_2^{(L)}(0)\left[a_2^{(R)}(0)\beta + \sum_{j=1}^{\infty} a_2^{(R)}(|j|)\widetilde{\psi}_j\right]. \tag{2.35}$$

with components of the eigenvector being

$$\widetilde{\psi}_i = \left(\frac{\sqrt{\lambda_1}}{\lambda_2}\right)^{|i|}\frac{a_2^{(L)}(|i|)}{a^{(L)}(0)},\ i \geq 0. \tag{2.36}$$

Now, consider the case $i < 0$. In terms of $\widetilde{\psi}_i$, eq. (2.32) may be written as

$$\left(\frac{\sqrt{\lambda_1}}{\lambda_2}\right)^{|i|} a_2^{(L)}(|i|)\left[a_2^{(R)}(|i|)\beta + \sum_{j=1}^{\infty} a_2^{(R)}(|j+i|)\widetilde{\psi}_j\right] = \Lambda_2\widetilde{\psi}_i,\ i < 0. \tag{2.37}$$

Substituting $\widetilde{\psi}_j$ for $j \geq 0$, from eq. (2.36), we obtain

$$\left(\frac{\sqrt{\lambda_1}}{\lambda_2}\right)^{|i|} a_2^{(L)}(|i|)F(i) = \Lambda_2\widetilde{\psi}_i,\ i < 0, \tag{2.38}$$

where, the function $F(i)$ is defined as

$$F(i) = a_2^{(R)}(|i|)\beta + \sum_{j=1}^{\infty}\left(\frac{\sqrt{\lambda_1}}{\lambda_2}\right)^{|j|}\frac{a_2^{(R)}(|j+i|)a_2^{(L)}(|j|)}{a_2^{(L)}(0)}. \tag{2.39}$$

The solution to eq. (2.38) is clearly

$$\Lambda_2 = a_2^{(L)}(0)F(0), \tag{2.40}$$

which is consistent with eq. (2.35), and

$$\widetilde{\psi}_i = \left(\frac{\sqrt{\lambda_1}}{\lambda_2}\right)^{|i|} \frac{a_2^{(L)}(|i|)F(i)}{a_2^{(L)}(0)F(0)}, \; i < 0. \tag{2.41}$$

Eq. (2.35), eq. (2.36), and eq. (2.41) determine Λ_2 and the components of the eigenvector. To solve for Λ_2 in terms of $a_2^{(L)}(\Delta)$ and $a_2^{(R)}(\Delta)$, it is convenient to define three quantities

$$\begin{aligned} k_1 &= \sum_{i=1}^{\infty} \left(\frac{\sqrt{\lambda_1}}{\lambda_2}\right)^{|i|} a_2^{(L)}(|i|)a_2^{(R)}(|i|), & (2.42)\\ k_2 &= \sum_{i=-\infty}^{0} \left(\frac{\sqrt{\lambda_1}}{\lambda_2}\right)^{|i|} a_2^{(L)}(|i|)a_2^{(R)}(|i|), & (2.43)\\ k_3 &= \sum_{i=-\infty}^{0} \sum_{j=1}^{\infty} \left(\frac{\sqrt{\lambda_1}}{\lambda_2}\right)^{|i|+|j|} \frac{a_2^{(L)}(|i|)a_2^{(R)}(|i+j|)a_2^{(L)}(|j|)}{a_2^{(L)}(0)}. & (2.44) \end{aligned}$$

Solving for β in eq. (2.34) and eq. (2.35) by substituting for $\widetilde{\psi}_i$ from eq. (2.41) and eq. (2.36) respectively, we obtain

$$\begin{aligned} \beta &= \frac{k_3}{\Lambda_2 - k_2}, & (2.45)\\ \beta &= \frac{\Lambda_2 - k_1}{a_2^{(L)}(0)a_2^{(R)}(0)}. & (2.46) \end{aligned}$$

Equating eq. (2.45) and eq. (2.46) to eliminate β, we find that Λ_2 satisfies the quadratic equation

$$\Lambda_2^2 - (k_1 + k_2)\Lambda_2 + k_1 k_2 - k_3 a_2^{(L)}(0)a_2^{(R)}(0) = 0, \tag{2.47}$$

whose largest root is

$$\Lambda_2 = \frac{k_1 + k_2 + \sqrt{(k_1 - k_2)^2 + 4a_2^{(L)}(0)a_2^{(R)}(0)k_3}}{2}. \tag{2.48}$$

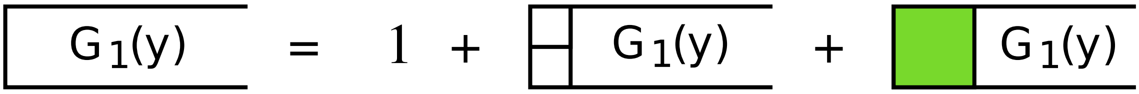

Figure 2.4: Diagrammatic representation of the recursion relation obeyed by the generating function $G_1(y)$ defined for a track of width 2 [see eq. (2.52) for definition]. The first column of the track may be occupied by two vacancies (open 1×1 square) or a square (filled 2×2 square).

The largest eigenvalue may be further simplified using

$$\begin{aligned} k_2 - k_1 &= a_2^{(L)}(0) a_2^{(R)}(0), && (2.49) \\ \widetilde{k} &= k_2 + k_1 = \sum_{i=-\infty}^{\infty} \left(\frac{\sqrt{\lambda_1}}{\lambda_2}\right)^{|i|} a_2^{(L)}(|i|) a_2^{(R)}(|i|). && (2.50) \end{aligned}$$

After simplification we get the largest eigenvalue

$$\Lambda_2 = \frac{\widetilde{k} + \sqrt{[a_2^{(L)}(0) a_2^{(R)}(0)]^2 + 4 a_2^{(L)}(0) a_2^{(R)}(0) k_3}}{2}, \tag{2.51}$$

with k_3 as in eq. (2.44) and $\widetilde{k}$ as in eq. (2.50).

2.4 Calculation of Partition Functions of Tracks

2.4.1 Partition function of track of width 2

In this subsection, we determine the asymptotic behavior of the partition function $\mathcal{L}(\ell)$ of a track of width 2 and length ℓ [the shape of the track is shown in Fig. 2.4(b)]. We define the generating function

$$G_1(y) = \sum_{\ell=0}^{\infty} \mathcal{L}(\ell) y^{\ell}, \tag{2.52}$$

where the power of $\sqrt{y}$ is the number of sites present in the system. The recursion relation obeyed by $G_1(y)$ is shown diagrammatically in Fig. 2.4 and can be written as

$$G_1(y) = 1 + y G_1(y) + z y^2 G_1(y), \tag{2.53}$$

which may be solved to give

$$G_1(y) = \frac{1}{1 - y - zy^2}. \tag{2.54}$$

Let y_1 be the smallest root of the denominator $1 - y - zy^2$ of eq. (2.54), i.e.

$$y_1 = \frac{\sqrt{1 + 4z} - 1}{2z}. \tag{2.55}$$

By finding the coefficient of y^ℓ for large ℓ, it is straightforward to obtain

$$\mathcal{L}(\ell) = a_1 \lambda_1^\ell [1 + O(\exp(-c\ell))], \; c > 0, \; \ell \gg 1, \tag{2.56}$$

where

$$\lambda_1 = \frac{1}{y_1}, \; a_1 = \frac{1}{2 - y_1}. \tag{2.57}$$

2.4.2 Partition functions of tracks of width 4

In this subsection, we determine the partition functions of tracks of width 4 without any constraints. The shape of a generic track of width 4 is characterized by parameters ℓ and Δ, and is shown in Fig. 2.3 (a). Calculating these partition functions will allow us to determine $a_2(\Delta)$ as defined in eq. (2.11).

Consider the following generating function.

$$G_2(y, \Delta) = \sum_{\ell=0}^{\infty} \Omega_2(\ell, \Delta) y^{2\ell+\Delta}, \tag{2.58}$$

where the power of $\sqrt{y}$ is the number of sites in the system. $G_2(y, 0)$ and $G_2(y, 1)$ obey simple recursion relations which are shown diagrammatically in Fig. 2.5. In equation

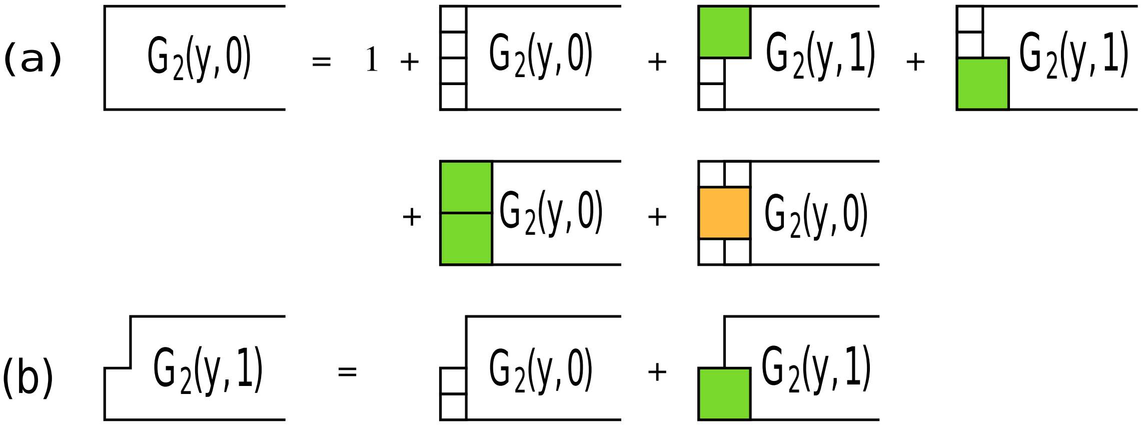

Figure 2.5: Diagrammatic representation of the recursion relation obeyed by the generating functions (a) $G_2(y, 0)$ and (b) $G_2(y, 1)$ for a track of width 4 [see eq. (2.58) for definition]. Right hand side enumerates the different ways the first column of the track may be occupied by vacancies (open 1×1 square), square (filled 2×2 green square) and defect (filled 2×2 yellow square).

form, they are

$$G_2(y, 0) = 1 + y^2G_2(y, 0) + 2zy^3G_2(y, 1) + (z^2y^4 + z_Dy^4)G_2(y, 0), \tag{2.59}$$

$$G_2(y, 1) = yG_2(y, 0) + zy^2G_2(y, 1), \tag{2.60}$$

where z_D is the activity associated with each defect square. These relations are easily solved to give

$$G_2(y, 0) = \frac{1 - zy^2}{f(y^2)}, \tag{2.61}$$

$$G_2(y, 1) = \frac{y}{f(y^2)}, \tag{2.62}$$

where

$$f(y) = z(z^2 + z_D)y^3 - (z^2 + z + z_D)y^2 - (1 + z)y + 1.$$

Let y_2 be the smallest root of $f(y) = 0$. For very large ℓ, we may write $\Omega_2(\ell, \Delta)$ as

$$\Omega_2(\ell, \Delta) = a_2(\Delta)\lambda_2^{2\ell+\Delta}[1 + O(\exp(-c\ell))], \ \ell \gg 1, \ c > 0, \tag{2.63}$$

where

$$\lambda_2 = \frac{1}{\sqrt{y_2}}. \tag{2.64}$$

Calculating coefficient of $y^{2\ell+\Delta}$, the prefactor $a_2(\Delta)$ for $\Delta = 0, 1$ is obtained to be

$$a_2(0) = \frac{-(1 - zy_2)}{y_2 f'(y_2)}, \tag{2.65}$$

$$a_2(1) = \frac{-1}{\sqrt{y_2} f'(y_2)}. \tag{2.66}$$

We now consider $\Delta \geq 2$. The recursion relation obeyed by $\Omega_2(\ell, \Delta)$ for $\Delta \geq 2$ is shown diagrammatically in Fig. 2.6, and may be written mathematically as

$$\Omega_2(\ell, \Delta) = \Omega_2(\ell, \Delta - 1) + z\Omega_2(\ell, \Delta - 2), \quad \Delta = 2, 3, ... \tag{2.67}$$

We define the generating function

$$F(\ell, x) = \sum_{\Delta=0}^{\infty} \Omega_2(\ell, \Delta) x^{\Delta}. \tag{2.68}$$

Multiplying eq. (2.67) by x^{Δ} and summing from 2 to ∞, we obtain a linear equation obeyed by $F(\ell, x)$ which is easily solved to give

$$F(\ell, x) = \frac{\Omega_2(\ell, 0) + x[\Omega_2(\ell, 1) - \Omega_2(\ell, 0)]}{1 - x - zx^2}, \tag{2.69}$$

where $\Omega_2(\ell, 0)$ and $\Omega_2(\ell, 1)$ have already been determined [see eq. (2.61), eq. (2.62)]. $F(\ell, x)$ has two simple poles at

$$x_{\pm} = \frac{-1 \pm \sqrt{1 + 4z}}{2z}. \tag{2.70}$$

Expanding the denominator about its two roots $x_{\pm}$, we determine $\Omega_2(\ell, \Delta)$ by calculating

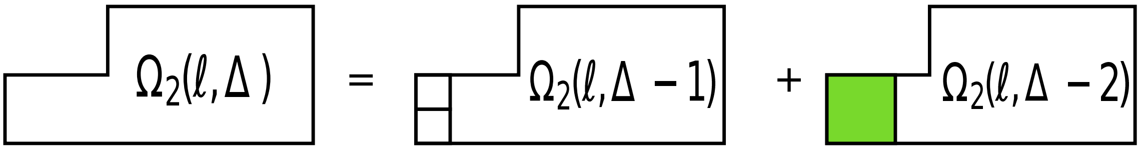

Figure 2.6: Diagrammatic representation of the recursion relation obeyed by the partition function $\Omega_2(\ell,\Delta)$ with $\Delta \geq 2$, for a track of width 4. The first column of the track may be occupied by two vacancies (open 1×1 square) or a square (filled 2×2 square).

the coefficient of x^Δ. We obtain

$$a_2(\Delta) = A_+(x_+\lambda_2)^{-\Delta} + A_-(x_-\lambda_2)^{-\Delta},\ \Delta = 0, 1, 2...,\tag{2.71}$$

where

$$A_\pm = \frac{\pm[\lambda_2 a_2(1) - (zx_\mp + 1)a_2(0)]}{\sqrt{1+4z}}.\tag{2.72}$$

2.4.3 Calculation of $a_2^{(L)}(\Delta)$

In this subsection, we calculate the pre-factor $a_2^{(L)}(\Delta)$ that characterizes the asymptotic behavior of the partition function of track of width 4 [see eq. (2.12)] for the left phase. The left phase has the constraint that the right edge of the rightmost square must touch the interface [see discussion in the paragraph following eq. (2.6)]. Thus

$$\Omega_2^{(L)}(\ell,\Delta) = z^2\Omega_2(\ell-2,\Delta),\tag{2.73}$$

where the factor z^2 accounts for the two squares adjacent to interface. Once these two squares are placed the occupation of the rest of the track has no constraints and hence enumerated by $\Omega_2(\ell-2,\Delta)$. Using eq. (2.73), eq. (2.12) and eq. (2.63), for very large ℓ we obtain

$$a_2^{(L)}(\Delta) = \frac{z^2}{\lambda_2^4}a_2(\Delta),\tag{2.74}$$

where $a_2(\Delta)$ is given in eq. (2.71).

2.4.4 Calculation of $a_2^{(R)}(\Delta)$

In this subsection, we calculate $a_2^{(R)}(\Delta)$ for $\Delta \geq 0$, as defined in eq. (2.13). Consider the track labeled by (ξ_i, ξ_{i+1}) [see Fig. 2.2]. The constraint on the right phase is that a defect is allowed to be present only to to the right of $\min(\xi_i, \xi_{i+1})$ and there must be at least one non-defect square present to its left [see discussion in the paragraph following eq. (2.6)].

First consider $\Delta = 0, 1$. The recursion relation obeyed by the partition functions $\Omega_2^{(R)}(\ell, 0)$ and $\Omega_2^{(R)}(\ell, 1)$ for right phase are shown diagrammatically in Fig. 2.7 and may be written as

$$\Omega_2^{(R)}(\ell, 0) = \Omega_2^{(R)}(\ell - 1, 0) + 2z\Omega_2(\ell - 2, 1) + z^2\Omega_2(\ell - 2, 0), \tag{2.75}$$

$$\Omega_2^{(R)}(\ell, 1) = \Omega_2^{(R)}(\ell, 0) + z\Omega_2(\ell - 1, 1). \tag{2.76}$$

Using the asymptotic expressions for the partition functions as given in eq. (2.11) and eq. (2.13), we obtain two linear equations for $a_2^{(R)}(0)$ and $a_2^{(R)}(1)$, which are easily solved to give

$$a_2^{(R)}(0) = \frac{z[2a_2(1)\lambda_2 + za_2(0)]}{\lambda_2^2(\lambda_2^2 - 1)}, \tag{2.77}$$

$$a_2^{(R)}(1) = \frac{\lambda_2 a_2^{(R)}(0) + za_2(1)}{\lambda_2^2}. \tag{2.78}$$

Now consider $\Delta \geq 2$. The recursion relation obeyed by $\Omega_2^{(R)}(\ell, \Delta)$ for $\Delta \geq 2$ may be written as

$$\Omega_2^{(R)}(\ell, \Delta) = \Omega_2^{(R)}(\ell, \Delta - 1) + z\widetilde{\Omega}_2(\ell, \Delta - 2) \tag{2.79}$$

where $\widetilde{\Omega}_2(\ell, \Delta)$ is the partition function for a generalization of the shape for $\Omega_2^{(R)}(\ell, 1)$ in the left hand side of Fig. 2.7. The lack of the subscript (R) means that there are no constraints. The first term in the right hand side of eq. (2.79) corresponds to placing vacancies

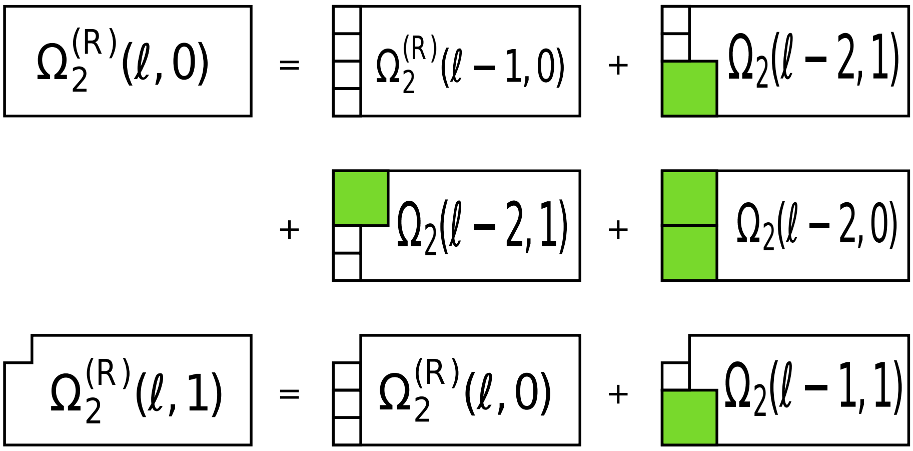

Figure 2.7: Diagrammatic representation of the recursion relation obeyed by the partition functions $\Omega_2^{(R)}(\ell,0)$ and $\Omega_2^{(R)}(\ell,1)$ for the track of width 4. Right hand side enumerates the different ways the first column of the track may be occupied by vacancies (open 1×1 square) or squares (filled 2×2 square).

in first column, and the second term to a non-defect square being placed. $\Omega_2^{(R)}(\ell,\Delta-1)$ in the right hand side of eq. (2.79) may be iterated further to yield

$$\Omega_2^{(R)}(\ell,\Delta) = \Omega_2^{(R)}(\ell,1) + z\sum_{i=0}^{\Delta-2}\widetilde{\Omega}_2(\ell,i), \tag{2.80}$$

To solve eq. (2.80), consider the generating function $\widetilde{G}_2(y,\Delta)$ defined as

$$\widetilde{G}_2(y,\Delta) = \sum_{\ell=0}^{\infty}\widetilde{\Omega}_2(\ell,\Delta)y^{2\ell+3\Delta/2}, \tag{2.81}$$

where power of $\sqrt{y}$ gives total number of sites in the system. The diagrammatic representation of the recursion relation obeyed by $\widetilde{G}_2(y,1)$ is shown in Fig. 2.8 and may be written as

$$\widetilde{G}_2(y,1) = y^{3/2}G_2(y,0) + zy^{5/2}G_2(y,1) + z_D y^{7/2}G_2(y,0), \tag{2.82}$$

where z_D is the activity associated with each defect, and $G_2(y,0)$ and $G_2(y,1)$ are as in eq. (2.61) and eq. (2.62). The generating function $\widetilde{G}_2(y,1)$ is then easily solved to give

$$\widetilde{G}_2(y,1) = \frac{(1+z_D y^2 - zz_D y^4)y^{3/2}}{f(y^2)}. \tag{2.83}$$

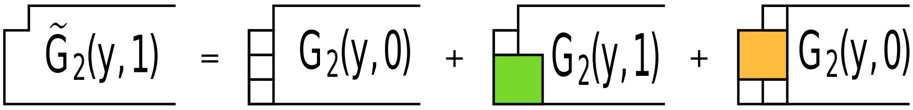

Figure 2.8: Diagrammatic representation of the recursion relation obeyed by the generating function $\widetilde{G}_2(y,1)$ [see eq. (2.81) for definition] for a track of width 4. Right hand side enumerates the different ways the first column of the track may be occupied by vacancies (open 1×1 square), square (filled 2×2 square of color green) and defect (filled 2×2 square of color yellow).

For large ℓ the partition function may be written asymptotically as

$$\widetilde{\Omega}_2(\ell,\Delta) = \widetilde{a}_2(\Delta)\lambda_2^{2\ell+\Delta}, \ \Delta \geq 0, \ \ell \gg 1. \tag{2.84}$$

Calculating the coefficient of $y^{2\ell+3/2}$ from eq. (2.83) and using eq. (2.84), we obtain the prefactor

$$\widetilde{a}_2(1) = \frac{-(1+z_D y_2 - z z_D y_2^2)}{\sqrt{y_2} f'(y_2)}. \tag{2.85}$$

Now calculate the partition function $\widetilde{\Omega}_2(\ell,\Delta)$ for $\Delta \geq 2$. The diagrammatic representation of the recursion relation obeyed by the partition function $\widetilde{\Omega}_2(\ell,\Delta)$ for $\Delta \geq 2$ is shown in Fig. 2.9 and may be written mathematically as

$$\widetilde{\Omega}_2(\ell,\Delta) = \widetilde{\Omega}_2(\ell,\Delta-1) + (z+z_D)\widetilde{\Omega}_2(\ell,\Delta-2), \ \Delta = 2,3,.... \tag{2.86}$$

We define the generating function

$$H(\ell,t) = \sum_{\Delta=0}^{\infty} \widetilde{\Omega}_2(\ell,\Delta)t^{\Delta}. \tag{2.87}$$

Multiplying eq. (2.86) by t^{Δ} and performing summation over Δ from 2 to ∞, we obtain a linear equation obeyed by $H(\ell,t)$ which is solved to give

$$H(\ell,t) = \frac{\widetilde{\Omega}_2(\ell,0) + t\left[\widetilde{\Omega}_2(\ell,1) - \widetilde{\Omega}_2(\ell,0)\right]}{1 - t - (z+z_D)t^2}. \tag{2.88}$$

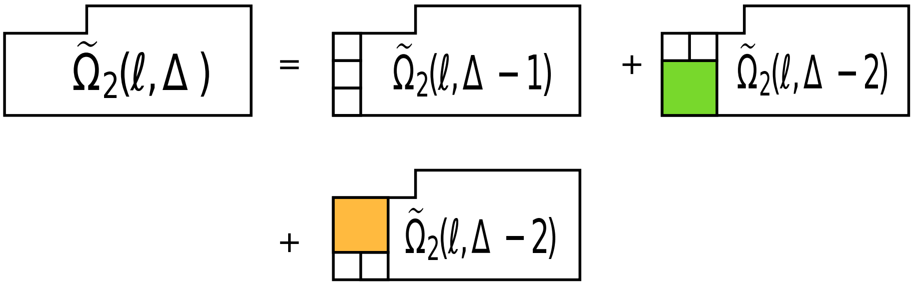
$\widetilde{\Omega}_2(\ell,\Delta)$
=
$\widetilde{\Omega}_2(\ell,\Delta-1)$
+
$\widetilde{\Omega}_2(\ell,\Delta-2)$
+
$\widetilde{\Omega}_2(\ell,\Delta-2)$

Figure 2.9: Diagrammatic representation of the recursion relation obeyed by the partition function $\widetilde{\Omega}_2(\ell, \Delta)$ with $\Delta \geq 2$ for a track of width 4. Right hand side enumerates the different ways the first column of the track may be occupied by vacancies (open 1×1 square), square (filled 2×2 square of color green) and defect (filled 2×2 square of color yellow).

$H(\ell, t)$ has two simple poles determined by the roots of the quadratic equation $1 - t - (z + z_D)t^2 = 0$

$$t_\pm = \frac{-1 \pm \sqrt{1 + 4(z + z_D)}}{2(z + z_D)}. \tag{2.89}$$

Expanding the denominator about $t_\pm$ and calculating the coefficient of t^Δ, we get the expression for $\widetilde{\Omega}_2(\ell, \Delta)$ and using eq. (2.84) the prefactor is obtained to be

$$\widetilde{a}_2(\Delta) = B_+(t_+\lambda_2)^{-\Delta} + B_-(t_-\lambda_2)^{-\Delta}, \ \Delta \geq 0, \tag{2.90}$$

where

$$B_\pm = \frac{\pm\left[\lambda_2\widetilde{a}_2(1) - [(z + z_D)t_\mp + 1]a_2(0)\right]}{\sqrt{1 + 4(z + z_D)}}. \tag{2.91}$$

We now return to eq. (2.80) and replace the partition functions $\Omega_2^{(R)}(\ell, \Delta)$ and $\widetilde{\Omega}_2(\ell, i)$ by their asymptotic forms given in eq. (2.13) and eq. (2.84) respectively, and do the summation over $\widetilde{\Omega}_2(\ell, i)$ from $i = 0$ to $(\Delta - 2)$, to obtain the prefactor

$$a_2^{(R)}(\Delta) = v_1\lambda_2^{-\Delta} + v_2(t_+\lambda_2)^{-\Delta} + v_3(t_-\lambda_2)^{-\Delta}, \ \Delta \geq 2, \tag{2.92}$$

where

$$\begin{aligned} v_1 &= a_2^{(R)}(1)\lambda_2 + z\Big(\frac{B_+t_+}{t_+-1} + \frac{B_-t_-}{t_--1}\Big), \\ v_2 &= -\frac{zB_+t_+^2}{t_+-1}, \\ v_3 &= -\frac{zB_-t_-^2}{t_--1}. \end{aligned}$$

2.5 Results

In this section we determine the interfacial tension $\sigma(z)$ between two ordered phases as a function of the activity z. From eq. (2.28), $\sigma(z)$ may be written as

$$\sigma(z) = -\frac{1}{2}\log\left[\frac{\lambda_1^2\Lambda_2}{za_1a_2(0)}\right], \tag{2.93}$$

where Λ_2, λ_1, a_1 and $a_2(0)$ are as in eq. (2.51), eq. (2.57), and eq. (2.65). Λ_2 depends on $a_2^{(L)}(\Delta)$ and $a_2^{(R)}(\Delta)$, which in turn have been calculated in eq. (2.74) and eq. (2.92). We also set $z_D = z$, where z_D is the activity of a defect.

The variation of $\sigma(z)$ with activity z is shown in Fig. 2.10. It decreases monotonically with decreasing z and becomes zero at a finite value of z, which will be our estimate of the critical activity z_c. We find that $z_c = 105.35$ for the interface with overhangs. As a check for the calculation, we confirm that if we set $z_D = 0$, then we obtain the results for the estimated z_c in the absence of defects [7]. The result for z_c compares well with the numerical estimate from Monte Carlo simulations of $z_c \approx 97.5$ [see table 1.1].

The occupied area fraction or density ρ may be calculated from the partition function $Z^{(0)}$ as:

$$\rho = \frac{4z}{N_xN_y}\frac{\partial}{\partial z}\Big[\log\big(Z^{(0)}\big)\Big], \tag{2.94}$$

where the factor 4 accounts for the area of a square. Substituting for $Z^{(0)}$ from eq. (2.22),

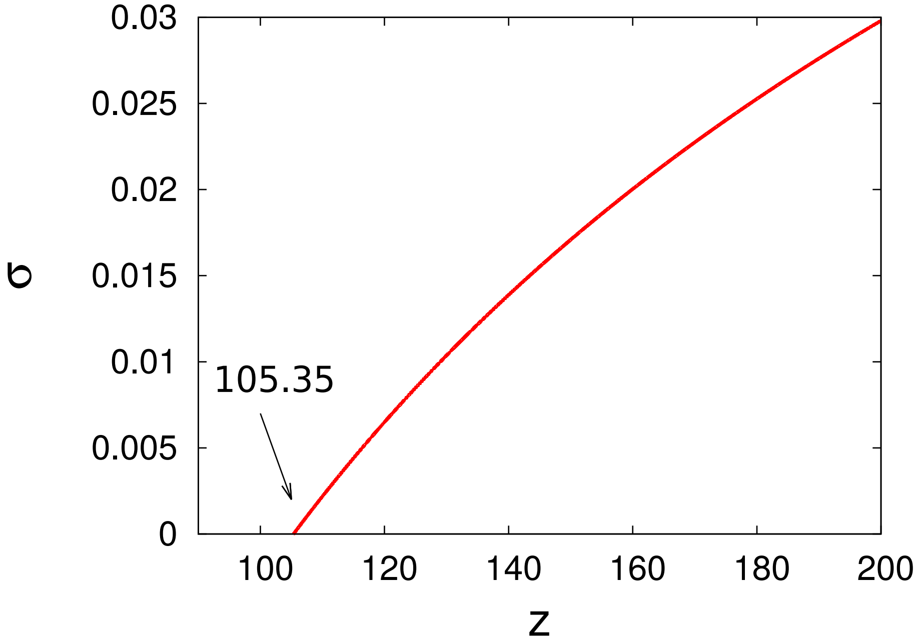

Figure 2.10: The variation of the interfacial tension $\sigma(z)$ with activity z. Interfacial tension $\sigma(z)$ vanishes at the critical activity $z = z_c$.

the density ρ in eq. (2.94), in the thermodynamic limit $N_x \to \infty$, $N_y \to \infty$, reduces to

$$\rho = 4z\left[\frac{1}{\lambda_2}\frac{\partial \lambda_2}{\partial z} - \frac{1}{2\lambda_1}\frac{\partial \lambda_1}{\partial z}\right]. \tag{2.95}$$

We thus obtain the critical density to be $\rho_c = 0.947$. This estimate compare well with the Monte Carlo results of $\rho_c \approx 0.932$ [see table 1.1].

2.6 Conclusion

In this paper, we estimated the transition point of the disordered-columnar transition in in the hard square model by calculating the interfacial tension between two ordered phases within a pairwise approximation. This calculation allows for multiple defects to be present as well as the interface to have effective overhangs. We obtain the critical activity $z_c = 105.35$ and critical density $\rho_c = 0.947$, which agrees reasonably with the numerically obtained results of $z_c \approx 97.5$ and $\rho_c \approx 0.932$. Our estimate for the critical activity is a considerable improvement over earlier estimates based on many different approaches [see table 1.1].

We calculated the prefactor $a_2^{(R)}(\Delta)$ by allowing defects to be present as overhangs [see section 2.4.4]. The calculation can be repeated when defects are present only in regions which do not correspond to overhangs. This corresponds to a defect in the right phase being present only to the right of $\max(\xi_i, \xi_{i+1})$ [see Fig. 2.2]. This calculation leads to an estimate of $z_c = 43.28$, which is about half the value of the numerical result of $z_c \approx 97.5$. The decrease in the value of z_c on excluding overhangs is consistent with the fact that the entropy of the system with interface decreases while the entropy of the system without interface remains unchanged. We, thus, conclude that the presence of overhangs in the interface is important for the calculation of interfacial tension.

A similar analysis for determining the phase boundary may be done for other kind of systems, which show a transition from disordered to columnar ordered phase with increasing density. The mixture of hard squares and dimers [8] shows such a transition, and so does the system of $(d \times 2)$ hard rectangles [73, 74, 7]. It would be interesting to see whether the approximation scheme used in this paper is useful in obtaining reliable estimates for the phase boundaries in these problems.

Chapter 3

Mixture of hard squares and dimers

3.1 Introduction

In this chapter, we estimate the phase boundary separating the disordered and columnar phase for the mixture of hard squares and dimers. The mixture of hard squares and dimers was studied both numerically and analytically in Ref. [8]. The system undergoes a transition from a square-rich columnar phase to a dimer-rich disordered phase across a critical line along which the critical exponents continuously vary depending on the composition of the mixture, consistent with the Ashkin-Teller universality class. On the fully packed line, it was shown that the system undergoes a Korterlitz-Thouless type transition from a columnar phase to a power law correlated phase as the dimer density is increased. Along the fully packed line, the configurations of dimers and squares may be mapped onto a height field. By writing an effective Hamiltonian for the two dimensional height field, it was possible to theoretically explain the numerically obtained results, along the fully packed line [8]. However, the height mapping does not allow the phase boundary to be determined, as the relation between the rigidity and microscopic parameters is not easy to establish. In this chapter, we determine the phase diagram within an approximation scheme, and compare with the numerically obtained phase boundary.

Estimates of phase boundaries in systems showing columnar order, obtained from standard approximation schemes like density functional theory, high density expansions, Flory-type approximations, etc., are quite poor [see Ref. [64] for a tabulation of results for the hard square model]. In recent work [7, 64], we described a systematic way of determining the interfacial tension between two differently ordered columnar phases in terms of number of defects and overhangs in the interface. The estimates obtained from the interfacial tension are in good agreement with the numerical results for the hard square gas [7, 64] as well as the hard rectangle gas [7]. In this thesis, we use the same method to obtain the phase boundary for the mixture of squares and dimers. We estimate the interfacial tension between two different columnar ordered phases and by setting it to zero, we obtain limiting condition for the stability of columnar phase. First, we assume that the interface between the two ordered phases has no overhangs and that the ordered phases have perfect order. We improve the estimate for the phase boundary by allowing the interface to have overhangs of height one. The results are summarized in Fig. 3.6. For instance, along the fully packed line our estimates for the critical density for squares are within 8% of the numerical result. The content of this chapter is published in Ref. [69].

3.2 Model and outline of calculation

Consider a square lattice of size $L_x \times L_y$. The lattice may be occupied by particles of three different shapes: squares, horizontal dimers and vertical dimers of size (2×2), (2×1) and (1×2) respectively. The particles interact only through excluded volume interaction, i.e. no two particles may overlap. We associate with each square, horizontal dimer, vertical dimer and vacancy (1×1) activities z_s, z_h, z_v and z_0 respectively. We will refer to the bottom left corner of a particle as its head.

Depending on the values of the activities, the system may exist in a disordered fluid like phase or in an ordered phase which has columnar order [8]. In the columnar phase, the heads of squares and vertical (horizontal) dimers preferably occupy either even or odd rows (columns) with equal fraction on an average in even or odd columns (rows).

The aim of the chapter is to determine the phase boundary between the columnar and disordered phases. This is done by estimating the interfacial tension $\sigma(z_s, z_h, z_v, z_0)$ between two ordered columnar phases, and by equating it to zero, we obtain estimates for the critical activities and densities. Let the phase in which majority of heads of squares and vertical dimers are in even (odd) rows be called even (odd) phase. To compute $\sigma(z_s, z_h, z_v, z_0)$, we impose an interface in the system by fixing squares at the left boundary to be even and those at the right boundary to be odd. A snapshot of a typical equilibrium configuration seen in a Monte Carlo simulation of a system with these boundary conditions is shown in Fig. 3.1. There is a left phase with even squares and vertical dimers separated from a right phase with odd squares and vertical dimers by an interface. The horizontal dimers could be even or odd in both phases. To define an unique position of the interface for any allowed configuration of particles, we adopt the convention that the boundary between the left or even phase and right or odd phase is placed as far left as possible. With this convention, there is a well-defined interface. The bulk phases have only few defects. By defects, we mean particles of the wrong type (odd in even phase or even in odd phase). When the defects are removed, a fully ordered columnar phase is recovered.

Let $Z^{(0)}$ and $Z^{(I)}$ be the partition function of the system without and with an interface I respectively. The interfacial tension σ is defined as

$$e^{-\sigma L_y} = \frac{\sum_I Z^{(I)}}{Z^{(0)}}, \tag{3.1}$$

Due to the nature of interactions between particles being hard core, we can write the partition function of the system in the presence of an interface as a product of the partition functions of the left and right phases, i.e.

$$Z^{(I)} = Z_L^{(I)} Z_R^{(I)}, \tag{3.2}$$

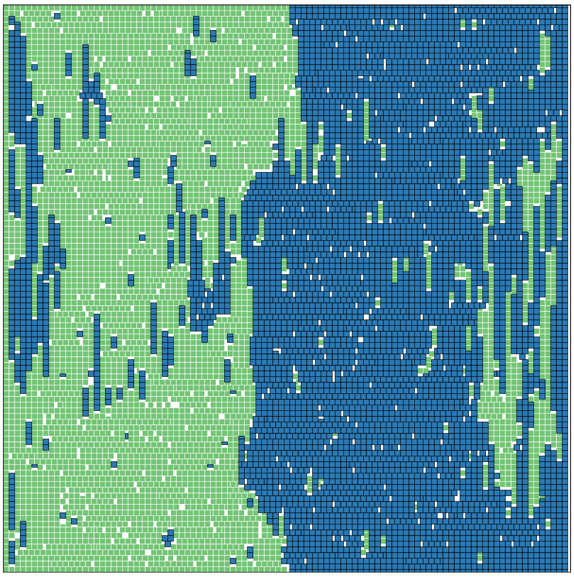

Figure 3.1: Snapshot of a typical equilibrium configuration of a system where the squares at the left boundary are fixed to be on even rows (green) and the squares at the right boundary are fixed to be on odd rows (blue). At high enough activity z_s (as in the figure), a sharp interface separates the left even phase from the right odd phase.

where L and R denote left and right.

$Z^{(I)}$ cannot be calculated for an arbitrary interface I. We therefore calculate it within two approximations. As a first approximation, we consider the simplest case where we ignore overhangs in the interface and defects in the bulk. In this simplified model, the interface is defined by the position of right boundary of the left phase, and denoted by η_i (see Fig. 3.2). Since we assume perfect columnar order for the left and right phases, the partition functions for both left and right phases are a product of partition functions of tracks made up of two adjacent rows ($L_y/2$ of them):

$$Z_L^{(I)} = \prod_{i=1}^{L_y/2} [z_v\Omega(\eta_i - 1, 0) + z_s\Omega(\eta_i - 2, 0)], \tag{3.3}$$

$$Z_R^{(I)} = \prod_{i=1}^{L_y/2} \Omega(L_x - \max(\eta_i, \eta_{i+1}), |\eta_i - \eta_{i+1}|), \tag{3.4}$$

where $\Omega(\ell, \Delta)$ is the partition function of a track of two rows with a shape as shown in Fig. 3.3. In the region corresponding to Δ, only horizontal dimers can be placed. The right hand side of Eq. (3.3) follows from the fact that, for the left phase, there must be either

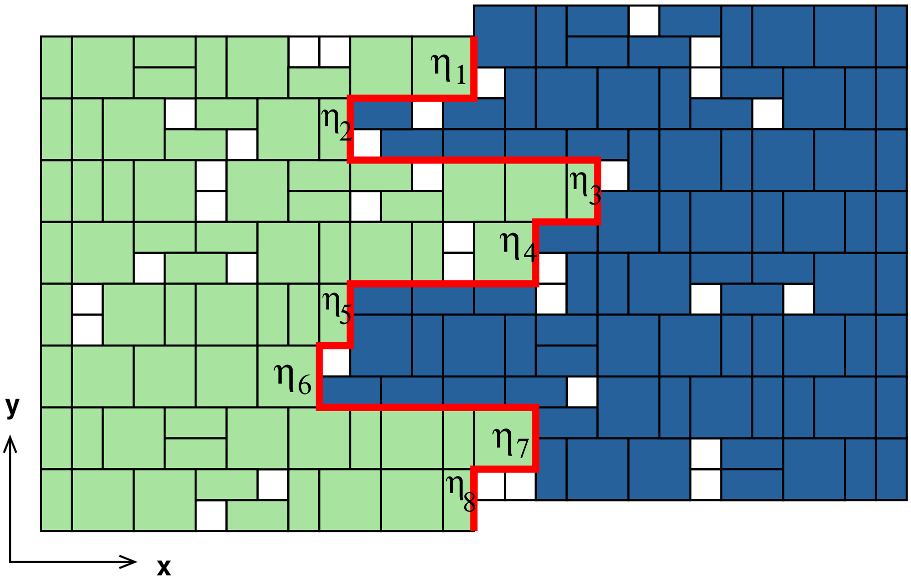

Figure 3.2: A schematic diagram of an interface that has no overhangs. The interface is indicated by the red line and its x-coordinates are denoted by η_i. The boundary conditions are periodic in the y-direction.

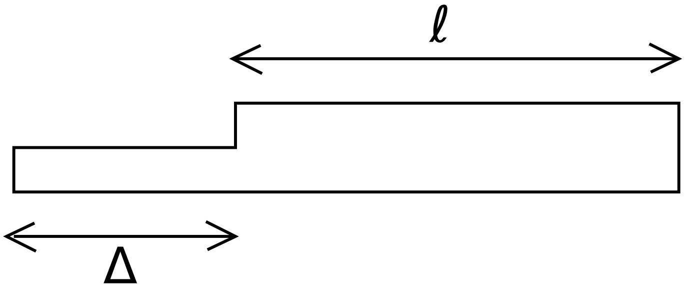

Figure 3.3: The shape of a generic track of two rows. It is characterized by two lengths ℓ and Δ and has partition function $\Omega(\ell, \Delta)$.

a vertical dimer or square touching the interface. The partition function of the system without an interface is

$$Z^{(0)} = \prod_{i=1}^{L_y/2} \Omega(L_x, 0). \tag{3.5}$$

In the second approximation, we allow the interface to have overhangs of height one. We still do not allow defects in the bulk. The calculation is on the same lines as that described above. This allows us to obtain an improved estimate of the critical parameters.

The calculation of the interfacial tension involves determining the partition function $\Omega(\ell,\Delta)$ of a track of two rows, and is done in the next section.

3.3 Calculation of two-row partition function $\Omega(\ell,\Delta)$

In this section we calculate $\Omega(\ell,\Delta)$, the partition function of a track of two rows with shape as shown in Fig. 3.3. Consider the generating function defined as

$$G(y,\Delta) = \sum_{\ell=0}^{\infty} \Omega(\ell,\Delta) y^{\ell+\Delta/2}, \tag{3.6}$$

where the power of $\sqrt{y}$ is the number of sites in the system.

First, consider the case $\Delta = 0, 1$. $G(y,0)$ and $G(y,1)$ obey simple recursion relations which are shown diagrammatically in Fig. 3.4 and may be written as

$$\begin{aligned} G(y,0) &= 1 + z_0^2 y G(y,0) + z_v y G(y,0) + z_s y^2 G(y,0) + \\ &\quad 2 z_0 z_h y^{3/2} G(y,1) + z_h^2 y^2 G(y,0), && (3.7)\\ G(y,1) &= z_h y G(y,1) + z_0 y^{1/2} G(y,0). && (3.8) \end{aligned}$$

These are easily solved to yield

$$G(y,0) = \frac{1 - z_h y}{f(y)}, \tag{3.9}$$

$$G(y,1) = \frac{z_0 \sqrt{y}}{f(y)}, \tag{3.10}$$

where the function $f(y)$ in the denominator is

$$\begin{aligned} f(y) =& z_h(z_s + z_h^2) y^3 - (z_s + z_h^2 + z_h z_0^2 - z_h z_v) y^2 \\ & - (z_h + z_v + z_0^2) y + 1, \end{aligned} \tag{3.11}$$

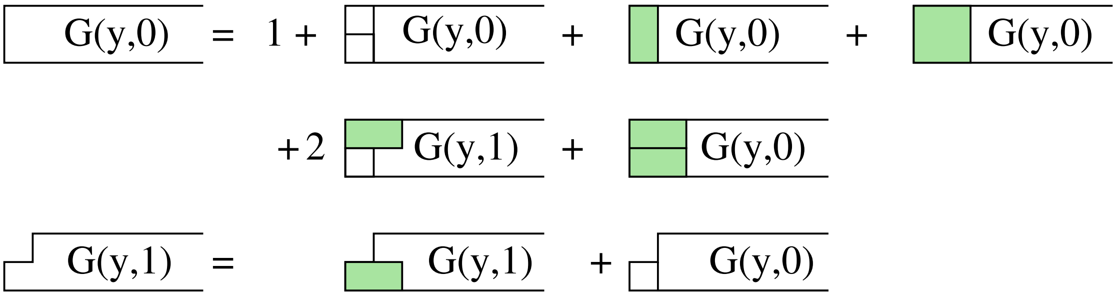

Figure 3.4: Diagrammatic representation of the recursion relations obeyed by the generating functions $G(y,0)$ and $G(y,1)$ [see Eq. (3.6) for definition]. The left-most column may be occupied by vacancies, dimers or squares.

a third order polynomial in y. Let y_1 be smallest root of $f(y) = 0$. Then, it is clear that

$$\Omega(\ell,\Delta) = a(\Delta)\lambda^{\ell}[1 + O(e^{-c\ell})], \quad \ell \gg 1, \tag{3.12}$$

where

$$\lambda = \frac{1}{y_1}. \tag{3.13}$$

The prefactor $a(\Delta)$ for $\Delta = 0, 1$ is determined by calculating the coefficient of $y^{\ell+\Delta/2}$. It is easily checked that

$$a(0) = \frac{-(1 - z_h y_1)}{y_1 f'(y_1)}, \tag{3.14}$$

$$a(1) = \frac{-z_0}{y_1 f'(y_1)}. \tag{3.15}$$

Equations (3.12)–(3.15) determine $\Omega(\ell,\Delta)$ for $\Delta = 0, 1$.

We now calculate $\Omega(\ell,\Delta)$ for $\Delta \geq 2$. The recursion relation obeyed by $\Omega(\ell,\Delta)$ is shown diagrammatically in Fig. 3.5, and may be written as

$$\Omega(\ell,\Delta) = z_0\Omega(\ell,\Delta-1) + z_h\Omega(\ell,\Delta-2), \ \Delta \geq 2. \tag{3.16}$$

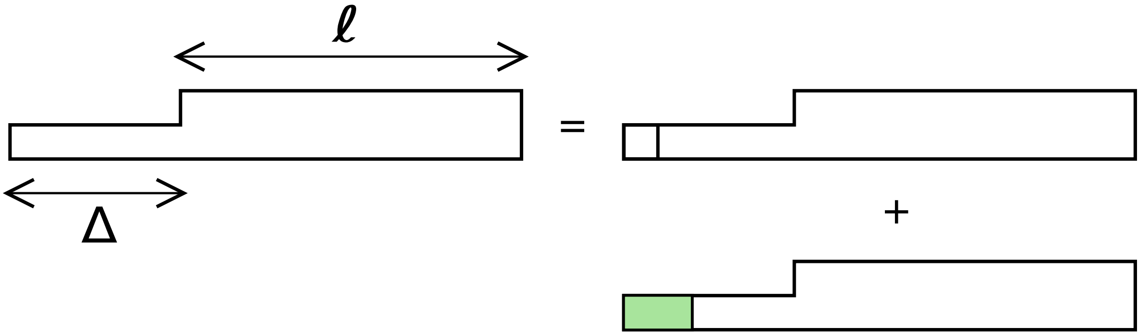

Figure 3.5: Diagrammatic representation of the recursion relation obeyed by $\Omega(\ell, \Delta)$, the partition function of a track of two rows as shown in Fig. 3.3, for $\Delta \geq 2$. The left-most column of the may be occupied by a vacancy or a horizontal dimer.

To solve Eq. (3.16), define the generating function

$$H(\ell, x) = \sum_{\Delta=0}^{\infty} \Omega(\ell, \Delta) x^{\Delta}. \tag{3.17}$$

Multiplying Eq. (3.16) by x^{Δ} and summing over Δ, we obtain a linear equation for $H(\ell, x)$ that may be solved to yield

$$H(\ell, x) = \frac{\Omega(\ell, 1)x + \Omega(\ell, 0)(1 - z_0 x)}{1 - z_0 x - z_h x^2}. \tag{3.18}$$

The generating function $H(\ell, x)$ has two simple poles determined by the zeros of the quadratic equation $1 - z_0 x - z_h x^2 = 0$. These are

$$x_{\pm} = \frac{-(z_0 \pm \sqrt{z_0^2 + 4z_h})}{2z_h}. \tag{3.19}$$

Expanding the denominator of Eq. (3.18) about x_+ and x_- we obtain the coefficient of x^{Δ} to be

$$\Omega(\ell, \Delta) = \sum_{i=\pm} \frac{a(1) + a(0) z_h x_i}{(z_0 + 2 z_h x_i) x_i^{\Delta}} \lambda^{\ell}, \ell \gg 1. \tag{3.20}$$

Using Eqs. (3.12) and (3.20), we can write

$$a(\Delta) = \frac{p_+}{x_+^\Delta} + \frac{p_-}{x_-^\Delta}, \Delta \geq 0, \tag{3.21}$$

where

$$p_\pm = \frac{a(1) + a(0) z_h x_\pm}{z_0 + 2 z_h x_\pm}.$$

3.4 Interfacial tension and critical parameters

We now calculate interfacial tension $\sigma(z_s, z_h, z_v, z_0)$. The results for the interface without overhangs is in Sec. 3.4.1 and for the interface with overhangs in Sec. 3.4.2.

3.4.1 Without overhangs

For large L_x and η_i, using Eqs. (3.3), (3.4) and (3.12), the partition functions of the left and right domains may be written as

$$\begin{aligned} Z_L^{(I)} &= \left[\frac{a(0)}{\lambda}(z_v + \frac{z_s}{\lambda})\right]^{L_y/2} \prod_{i=1}^{L_y/2} \lambda^{\eta_i}, && (3.22) \\ Z_R^{(I)} &= \prod_{i=1}^{L_y/2} a(|\eta_i - \eta_{i+1}|) \lambda^{L_x - \max(\eta_i, \eta_{i+1})}. && (3.23) \end{aligned}$$

Taking the product of Eqs. (3.22) and (3.23) and using the relation

$$\max(\eta_i, \eta_{i+1}) = \frac{|\eta_i - \eta_{i+1}| + \eta_i + \eta_{i+1}}{2}, \tag{3.24}$$

we obtain the partition function of the system with interface

$$\begin{aligned} Z^{(I)} &= \left[\frac{a(0)}{\lambda}(z_v + \frac{z_s}{\lambda})\right]^{L_y/2} \times \\ &\prod_{i=1}^{L_y/2}\left[\lambda^{L_x-|\eta_i-\eta_{i+1}|/2} a(|\eta_i - \eta_{i+1}|)\right]. \end{aligned} \tag{3.25}$$

Note that $Z^{(I)}$ depends only on the difference $|\eta_i - \eta_{i+1}|$ and not on η_i. Summing over all configurations I is equivalent to summing over all differences $(\eta_i - \eta_{i+1})$. Performing the sum and using Eq. (3.21), we obtain

$$\begin{aligned} \sum_I Z^{(I)} = &\Bigg[a(0)\lambda^{L_x-1}(z_v + \frac{z_s}{\lambda})\times \\ &\left(p_+ \frac{x_+\sqrt{\lambda}+1}{x_+\sqrt{\lambda}-1} + p_- \frac{x_-\sqrt{\lambda}+1}{x_-\sqrt{\lambda}-1}\right)\Bigg]^{L_y/2}. \end{aligned} \tag{3.26}$$

The partition function of the system without an interface can be easily calculated using Eq. (3.5)

$$Z^{(0)} = \left[\Omega(L_x, 0)\right]^{L_y/2} = \left[a(0)\lambda^{L_x}\right]^{L_y/2}. \tag{3.27}$$

The interfacial tension, as defined in Eq. (3.1) may be determined from Eqs. (3.26) and (3.27) to be

$$e^{-\sigma L_y} = \left[(\frac{z_v}{\lambda} + \frac{z_s}{\lambda^2})\left(p_+ \frac{x_+\sqrt{\lambda}+1}{x_+\sqrt{\lambda}-1} + p_- \frac{x_-\sqrt{\lambda}+1}{x_-\sqrt{\lambda}-1}\right)\right]^{\frac{L_y}{2}}. \tag{3.28}$$

The phase boundary corresponds to the values of the parameters at which the interfacial tension vanishes. This immediately gives

$$\left[\frac{z_v}{\lambda} + \frac{z_s}{\lambda^2}\right]\left[p_+ \frac{x_+\sqrt{\lambda}+1}{x_+\sqrt{\lambda}-1} + p_- \frac{x_-\sqrt{\lambda}+1}{x_-\sqrt{\lambda}-1}\right] = 1. \tag{3.29}$$

The phase boundary obtained from Eq. (3.29) is shown by the magenta line in Fig. 3.6(a) and Fig. 3.6(b). Here, the activities have been normalized using

$$z_s^{1/4} + z_d^{1/2} + z_0 = 1, \tag{3.30}$$

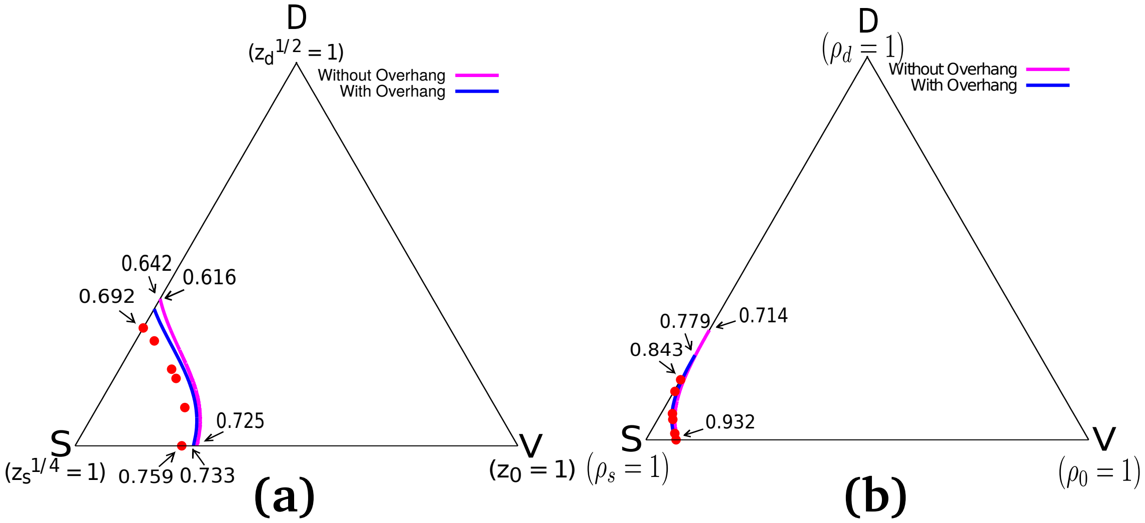

Figure 3.6: Phase diagram of the square-dimer model in (a) activity z-plane and (b) density ρ-plane. S and D represents the state where the lattice is fully packed by squares and dimers respectively. V represents the empty lattice. The estimates of the phase boundaries obtained from modelling the interface without overhangs is shown by magenta line while that obtained by including overhangs of height one are shown by blue lines. The data points (red circles) are obtained from Monte Carlo simulations.

where $z_d = z_h = z_v$, such that a two dimensional phase diagram may be obtained. It shows transitions at $z_s^{1/4} = 0.725$ along square-vacancy (SV) line and at $z_s^{1/4} = 0.616$ along square-dimer (SD) line. These should be compared with results from Monte Carlo simulations [8]: $z_s^{1/4} = 0.759$ along SV line and at $z_s^{1/4} = 0.692$ along SD line.

The density of sites occupied by squares ρ_s, horizontal dimers ρ_h and vertical dimers ρ_v may be calculated from the partition function $Z^{(0)}$ as:

$$\rho_s = \frac{4z_s}{L_xL_y}\frac{\partial \ln Z^{(0)}}{\partial z_s}, \tag{3.31}$$

$$\rho_i = \frac{2z_i}{L_xL_y}\frac{\partial \ln Z^{(0)}}{\partial z_i}, \quad i = h, v, \tag{3.32}$$

where the factor 4 and 2 accounts for the area of a square and a dimer respectively. Substituting for $Z^{(0)}$ from Eq. (3.27), the densities may be written in the thermodynamic limit

$L_x \to \infty$, $L_y \to \infty$ as:

$$\begin{aligned} \rho_s &= \frac{2z_s}{\lambda}\frac{\partial\lambda}{\partial z_s}, && (3.33) \\ \rho_i &= \frac{z_i}{\lambda}\frac{\partial\lambda}{\partial z_h},\ i = h, v, && (3.34) \end{aligned}$$

where total dimer density $\rho_d = \rho_h + \rho_v$ and density of vacancy $\rho_0 = 1 - \rho_d - \rho_s$.

In the density plane, it shows transitions at $\rho_s = 0.928$ along SV line and at $\rho_s = 0.714$ along SD line. The Monte Carlo results show transitions at $\rho_s = 0.932$ along SV line and at $\rho_s = 0.843$ along SD line. Our estimation of critical activities along SV and SD lines agree satisfactorily with the numerical results (see Sec. 3.4.3).

3.4.2 With overhangs

In the calculation presented in Sec. 3.4.1, the interface was modelled as having no overhangs. We now allow the interface to have a certain subclass of overhangs, and obtain an improved estimate for the phase boundary. To be able to do the calculation in the presence of overhangs, we first reformulate the calculation in the absence of overhangs in terms of a weighted, directed walk.

The interface with no overhang (see Fig. 3.2) may be visualized as a partially directed self avoiding walk (PDSAW) from top to bottom, where the walk is not allowed to take a step in the upward direction, but allowed to take steps in the leftward, rightward, and downward directions as long as the walk is self avoiding. We denote a downward step by $\mathbb{D}$, a leftward step of length Δ by $\mathbb{L}_\Delta$ and rightward step of length Δ by $\mathbb{R}_\Delta$. To maintain self avoidance, every set of consecutive leftward or rightward steps must be preceded (or followed) by a downward step. Thus, the different PDSAWs may be enumerated by arbitrary concatenation of substrings $\mathbb{D}$, $\mathbb{D}\mathbb{L}_\Delta$, and $\mathbb{D}\mathbb{R}_\Delta$ where $\Delta = 1, 2, \ldots$, and the length of the walk in the vertical direction is given by the number of $\mathbb{D}$s in the string. The formal generating function of these strings may be written as

$$\mathbb{G}_0 = \sum_{L_y=0,2,4,\ldots} (\mathbb{D} + \mathbb{D}\widetilde{\mathbb{R}} + \mathbb{D}\widetilde{\mathbb{L}})^{L_y/2}, \tag{3.35}$$

$$= \frac{1}{1 - (\mathbb{D} + \mathbb{D}\widetilde{\mathbb{R}} + \mathbb{D}\widetilde{\mathbb{L}})}, \tag{3.36}$$

where

$$\widetilde{\mathbb{L}} = \sum_{\Delta=1}^{\infty} \mathbb{L}_{\Delta}, \tag{3.37}$$

$$\widetilde{\mathbb{R}} = \sum_{\Delta=1}^{\infty} \mathbb{R}_{\Delta}. \tag{3.38}$$

The generating function $\mathbb{G}_0$ generates all possible walks of all possible lengths along the vertical direction. However, it does not assign weights to a walk.

To assign weights to each walk, we have to determine the weights D, L_Δ and R_Δ that correspond to the substrings $\mathbb{D}$, $\mathbb{L}_\Delta$, and $\mathbb{R}_\Delta$. To do so, we determine the weight of a PDSAW by taking the ratio of Eq. (3.25) and Eq. (3.27) to obtain

$$\frac{Z^{(I)}}{Z^{(0)}} = \left[\frac{a(0)}{\lambda}\left(z_v + \frac{z_s}{\lambda}\right)\right]^{L_y/2} \times$$

$$\prod_{i=1}^{L_y/2}\left[\lambda^{-|\eta_i-\eta_{i+1}|/2}\frac{a(|\eta_i - \eta_{i+1}|)}{a(0)}\right], \tag{3.39}$$

$$= D^{L_y/2}\prod_{i=1}^{L_y/2}(R, L)_{|\eta_i-\eta_{i+1}|}, \tag{3.40}$$

where R or L in Eq. (3.40) is chosen depending on whether the step is in the rightward or leftward direction. From Eqs. (3.39) and (3.40), we immediately read out

$$D = a(0)\left(\frac{z_s}{\lambda^2} + \frac{z_v}{\lambda}\right), \tag{3.41}$$

$$L_\Delta = \frac{a(\Delta)}{a(0)}\lambda^{-\Delta/2}, \tag{3.42}$$

$$R_\Delta = \frac{a(\Delta)}{a(0)}\lambda^{-\Delta/2}. \tag{3.43}$$

Consider now the weighted generating function

$$\mathcal{G}_0 = \frac{1}{1 - (D + D\widetilde{R} + D\widetilde{L})}, \tag{3.44}$$

where

$$\begin{aligned} \widetilde{R} &= \sum_{\Delta=1}^{\infty} R_\Delta = \sum_{\Delta=1}^{\infty} L_\Delta = \widetilde{L}, \\ &= \frac{1}{a(0)}\left(\frac{p_+}{x_+\sqrt{\lambda} - 1} + \frac{p_-}{x_-\sqrt{\lambda} - 1}\right). \end{aligned} \tag{3.45}$$

It is straightforward to see that, in terms of the interfacial tension σ, $\mathcal{G}_0$ may be written as

$$\mathcal{G}_0 = \sum_{L_y=0}^{\infty} e^{-2\sigma L_y}, \tag{3.46}$$

Equation (3.46) is convergent for all $\sigma > 0$, and diverges at $\sigma = 0$, corresponding to the transition point. From Eq. (3.44), the divergence of $\mathcal{G}_0$ corresponds to the condition

$$D + D\widetilde{R} + D\widetilde{L} = 1, \tag{3.47}$$

Substituting for D, $\widetilde{R}$ and $\widetilde{L}$ from Eqs. (3.41) and (3.45), we obtain the same same equation for the phase boundary as obtained earlier in Eq. (3.29).

We now allow the interface to have overhangs of height one. If an overhang is present, then a horizontal line on the dual lattice will intersect the interface more than once. A schematic diagram of an interface with overhangs is shown in Fig. 3.7. The interface with overhangs can no longer be interpreted as a PDSAW, as the walk is now allowed to take upward steps. However, restricting the overhangs to height one implies that each upward step has to followed by a downward step before another upward step can be taken. We now generalize the PDSAW to take into account these upward steps.

An overhang will be termed as right or left overhang depending on whether it appears in

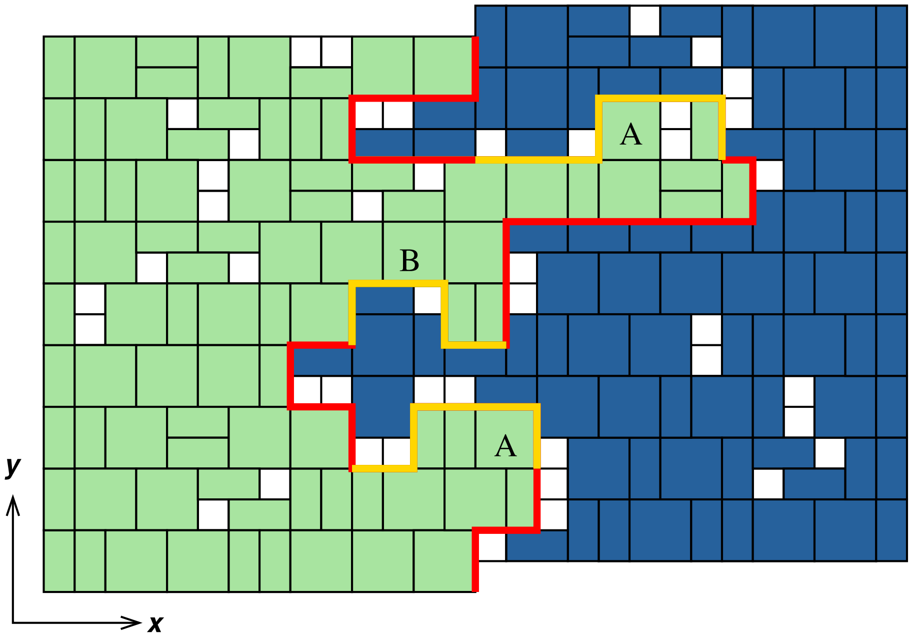

Figure 3.7: Schematic diagram of an interface with overhangs. Overhangs are indicated by yellow lines while the rest of the interface is indicated by red lines. Overhangs could be of type right (shown by A) or left (shown by B). The boundary conditions are periodic in the y-direction.

the right (as shown by yellow with index A in Fig. 3.7) or left phase (as shown by yellow with index B in Fig. 3.7). We now separately determine the generating function of all possible walks with right and left overhangs of height one.

3.4.2.1 Right Overhangs

There are two kinds of right overhangs depending on whether the first downward step is followed by rightward steps [see Fig. 3.8(a)] or leftward steps [see Fig. 3.8(b)]. We split each of these into two parts: the initial part shown by red and the remaining part shown by yellow in Fig. 3.8. This amounts to restricting to configurations where a horizontal dimer does not cross the right boundary of shaded region in Fig. 3.8. We denote these parts of the walk by $\mathbb{W}_R^{(1)}(n)$, $\mathbb{W}_R^{(2)}(n)$ and $\mathbb{O}_R(n_1,n_2)$ respectively, where the superscript refer to the two types of right overhangs and subscript R stands for right. Thus a generic

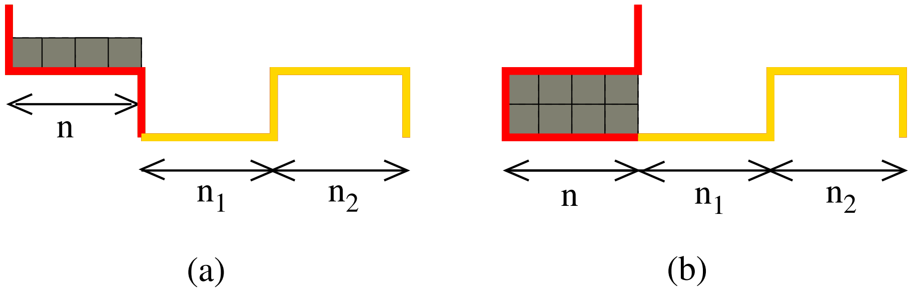

Figure 3.8: The two kinds of right overhang in which the first downward step is followed by (a) rightward or (b) leftward step. Overhangs are indicated by yellow lines.

right overhang is represented by

$$\mathbb{W}_R^{(i)}(n)\mathbb{O}_R(n_1, n_2)\mathbb{O}_R(n_3, n_4)..., \; i = 1, 2. \tag{3.48}$$

We now determine the weights for these overhangs. It is clear that

$$W_R^{(1)} = \sum_{n=1}^{\infty} wt[\mathbb{W}_R^{(1)}(n)] = D^2 \sum_{n=1}^{\infty} \omega(n)\lambda^{-n/2}, \tag{3.49}$$

$$W_R^{(2)} = \sum_{n=0}^{\infty} wt[\mathbb{W}_R^{(2)}(n)] = D^2 \sum_{n=0}^{\infty} \left[\omega(n)\lambda^{-n/2}\right]^2, \tag{3.50}$$

where the weight of $\mathbb{W}_R^{(i)}(n)$ may be determined by considering an interface with only one overhang. Here $\omega(\Delta)$ is the partition function of a track of width one and length Δ, and appears in the weights because the shaded region in Fig. 3.8 may be occupied by horizontal dimers.

The partition function $\omega(\Delta)$ is easily determined. Define the generating function

$$\widetilde{\omega}(x) = \sum_{\Delta=0}^{\infty} \omega(\Delta)x^{\Delta}, \tag{3.51}$$

where the power of x represents the number of sites in the system. The recursion relation obeyed by $\widetilde{\omega}(x)$ is shown diagrammatically in Fig. 3.9 and may be written as

$$\widetilde{\omega}(x) = 1 + z_0\widetilde{\omega}(x)x + z_h\widetilde{\omega}(x)x^2, \tag{3.52}$$

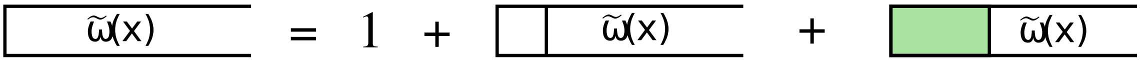

Figure 3.9: Diagrammatic representation of the recursion relation satisfied by the generating function $\widetilde{\omega}(x)$ [see Eq. (3.51) for definition]. The left-most column may be occupied by a vacancy or by a horizontal dimer.

with solution

$$\widetilde{\omega}(x) = \frac{1}{1 - z_0 x - z_h x^2}. \tag{3.53}$$

Expanding the denominator about its two roots $x_\pm$ [see Eq. (3.19)] and using Eq. (3.51), we can write

$$\omega(\Delta) = \frac{b_+}{x_+^\Delta} + \frac{b_-}{x_-^\Delta}, \Delta \geq 0, \tag{3.54}$$

where

$$b_\pm = \frac{1}{2 - z_0 x_\pm}. \tag{3.55}$$

Using Eq. (3.54), the weights $W_R^{(1)}$ and $W_R^{(2)}$ may be rewritten as

$$W_R^{(1)} = D^2\left(\frac{b_+}{x_+\sqrt{\lambda} - 1} + \frac{b_-}{x_-\sqrt{\lambda} - 1}\right), \tag{3.56}$$

$$\begin{aligned} W_R^{(2)} = D^2\Bigg(&\frac{b_+^2}{1 - (x_+^2\lambda)^{-1}} + \frac{b_-^2}{1 - (x_-^2\lambda)^{-1}} \\ &+ \frac{2b_+b_-}{1 - (x_+x_-\lambda)^{-1}}\Bigg). \end{aligned} \tag{3.57}$$

Now consider the weight O_R defined as

$$\begin{aligned} O_R &= \sum_{n_1}\sum_{n_2} wt[\mathbb{O}_R(n_1, n_2)] \\ &= O_R^{(A)} + O_R^{(B)} + O_R^{(C)} + O_R^{(D)}, \end{aligned} \tag{3.58}$$

where $O_R^{(i)}$ depends on the different ways the particles at the edge of the overhangs may be

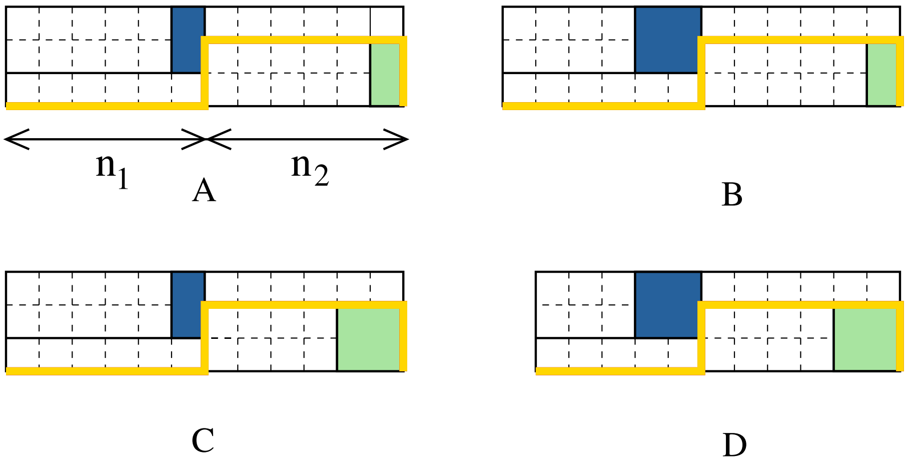

Figure 3.10: For each right overhang, there are four possible configurations (A–D) depending on whether the particles adjacent to the downward steps are squares or vertical dimers.

placed (see Fig. 3.10). The weight of these four kinds of overhangs may be determined in a straightforward manner by considering example of an interface with only downward step and one overhang :

$$
\begin{aligned}
O_R^{(A)} &= \sum_{n_1=1}^{\infty}\sum_{n_2=1}^{\infty}\Big[z_v^2\omega(n_1)\omega(n_2)\Omega(n_1-1,0)\Omega(n_2-1,0)\lambda^{-3(n_1+n_2)/2}\Big], && (3.59)\\
O_R^{(B)} &= \sum_{n_1=2}^{\infty}\sum_{n_2=1}^{\infty}\Big[z_v z_s\omega(n_1)\omega(n_2)\Omega(n_1-1,0)\Omega(n_2-2,0)\lambda^{-3(n_1+n_2)/2}\Big], && (3.60)\\
O_R^{(C)} &= \sum_{n_1=1}^{\infty}\sum_{n_2=2}^{\infty}\Big[z_s z_v\omega(n_1)\omega(n_2)\Omega(n_1-2,0)\Omega(n_2-1,0)\lambda^{-3(n_1+n_2)/2}\Big], && (3.61)\\
O_R^{(D)} &= \sum_{n_1=2}^{\infty}\sum_{n_2=2}^{\infty}\Big[z_s^2\omega(n_1)\omega(n_2)\Omega(n_1-2,0)\Omega(n_2-2,0)\lambda^{-3(n_1+n_2)/2}\Big]. && (3.62)
\end{aligned}
$$

The sums over n_i may be expressed in term of the generating function $G(y,0)$ [see Eq. 3.6]. This gives

$$
\begin{aligned}
O_R &= \bigg[G(x_+^{-1}\lambda^{-3/2},0)\frac{b_+}{x_+\lambda^{3/2}}\Big(\frac{z_s}{x_+\lambda^{3/2}}+z_v\Big)\\
&\quad + G(x_-^{-1}\lambda^{-3/2},0)\frac{b_-}{x_-\lambda^{3/2}}\Big(\frac{z_s}{x_-\lambda^{3/2}}+z_v\Big)\bigg]^2. \qquad (3.63)
\end{aligned}
$$

The total weight of all walks with right overhang may now be computed. Let $\mathbb{U}_R$ represent all possible walks with right overhang and having total weight U_R. Then

$$U_R = [W_R^{(1)} + W_R^{(2)}][O_R + O_R^2 + O_R^3 + ...] \\ \times[1 + R_1 + R_2 + ...], \tag{3.64}$$

where the second term in right hand side represent possible multiple overhang and the third term, the possibility of right steps after the overhang. U_R may be rewritten as

$$U_R = \left[W_R^{(1)} + W_R^{(2)}\right]\left[\frac{O_R}{1 - O_R}\right]\left[1 + \widetilde{R}\right], \tag{3.65}$$

where $\widetilde{R}$ is defined in Eq. (3.45).

3.4.2.2 Left Overhangs

The weight for left overhangs may be calculated in a manner similar to that for right overhangs. There are two kinds of left overhangs depending on whether the first downward step is followed by leftward steps [see Fig. 3.11 (a)] or rightward steps [see Fig. 3.11 (b)]. We split each of these into three parts, where the initial red line represents the first two downward steps and the intervening region, the middle yellow line represents overhangs and final red line represents leftward steps. We denote these parts symbolically by $\mathbb{W}_L^{(1)}(n)$, $\mathbb{W}_L^{(2)}(n)$, $\mathbb{O}_L(n_1, n_2)$ and $\mathbb{L}'(n')$ respectively, where the superscript (1) and (2) refer to the two kinds of left overhangs, and subscript L stands for left. Thus, a generic left overhang of first kind [see Fig. 3.11 (a)] is represented by

$$\mathbb{W}_L^{(1)}(n)\mathbb{O}_L(n_1, n_2)\mathbb{O}_L(n_3, n_4)...\mathbb{L}'(n'), \tag{3.66}$$

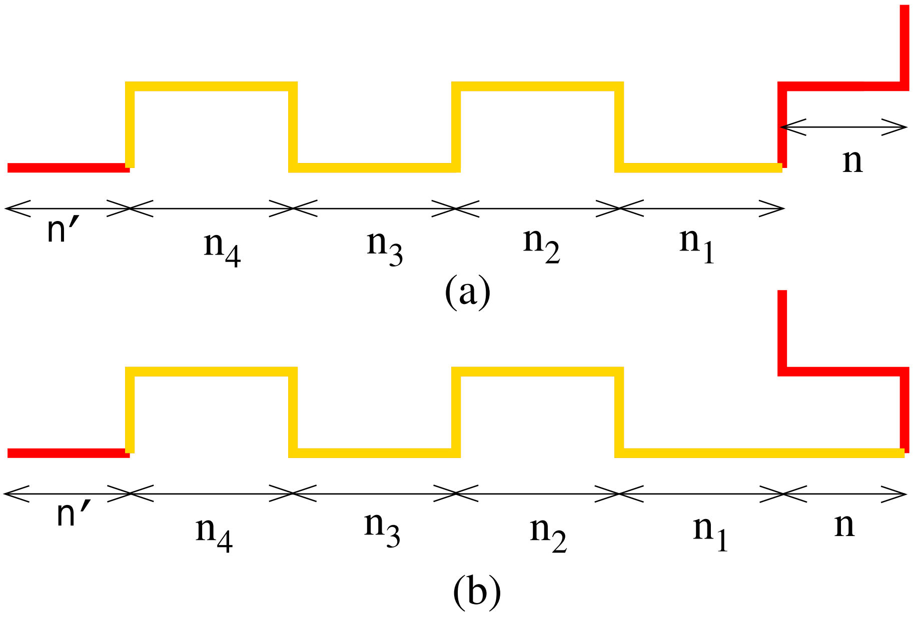

Figure 3.11: Schematic diagram of two ways of taking two downward steps before the beginning of an left overhang. The first downward step may be followed by (a) left or (b) right step. Overhangs are denoted by yellow line.

and that of the second kind [see Fig. 3.11 (b)] is represented by

$$\mathbb{W}_L^{(2)}(n)\mathbb{O}_L(n+n_1,n_2)\mathbb{O}_L(n_3,n_4)...\mathbb{L}'(n'). \tag{3.67}$$

We now determine the weights of the different parts constituting the left overhangs. For the overhang of first kind, the total weight associated with the initial red part $\mathbb{W}_L^{(1)}(n)$ may be written as

$$W_L^{(1)} = \sum_{n=1}^{\infty} wt[\mathbb{W}_L^{(1)}(n)] = D^2\sum_{n=1}^{\infty} L_\Delta = D^2\widetilde{L}, \tag{3.68}$$

where L_Δ and $\widetilde{L}$ are given respectively in Eqs. (3.42) and (3.45). The weight O_L associated with the left overhang is identical to that of the right overhang of similar shape, i.e.,

$$O_L = \sum_{n_1}\sum_{n_2} wt[\mathbb{O}_L(n_1,n_2)] = O_R, \tag{3.69}$$

where O_R is given in Eq. (3.63).

Now, consider the left overhangs of the second kind [see Fig. 3.11 (b)]. The total weight associated with the first two downward steps and the first overhang may be written as

$$\begin{aligned}\mathcal{W}_L^{(2)} &= \sum_{n}\sum_{n_1}\sum_{n_2} wt[\mathbb{W}_L^{(2)}(n)\mathbb{O}_L(n+n_1,n_2)] \\ &= \sum_{n=0}^{\infty}\sum_{n_1=1}^{\infty} D^2 L_n \omega(n+n_1)\Big[z_v\Omega(n+n_1-1,0) \\ &+ z_s\Omega(n+n_1-2,0)\Big]\lambda^{-3(n+n_1)/2}\sqrt{O_L}, \end{aligned} \tag{3.70}$$

where the summation over n_2 contributes $\sqrt{O_L}$. It is convenient to change the variable to $m = n + n_1$. In this new variable Eq. (3.70) may be rewritten as

$$\begin{aligned}\mathcal{W}_L^{(2)} &= \sum_{m=1}^{\infty}\sum_{n=0}^{m-1} D^2 L_n m\omega(m)\Big[z_v\Omega(m-1,0) \\ &+ z_s\Omega(m-2,0)\Big]\lambda^{-3m/2}\sqrt{O_L}. \end{aligned} \tag{3.71}$$

We define the functions

$$\mathcal{F}_i(y) = y^{1+i}\frac{d}{dy'}\Big[G(y',0)\Big]_{y'=y} + iy^iG(y,0), \tag{3.72}$$

where $i = 1, 2$ and $G(y,0)$ is the generating function as determined in Eq. (3.7). Doing the sums in Eq. (3.71), we obtain

$$\begin{aligned}\mathcal{W}_L^{(2)} &= \tfrac{D^2}{a(0)}\Bigg[\Bigg(\tfrac{p_+x_+\sqrt{\lambda}}{x_+\sqrt{\lambda}-1} + \tfrac{p_-x_-\sqrt{\lambda}}{x_-\sqrt{\lambda}-1}\Bigg)\mathcal{J}\Bigg(\tfrac{1}{x_+\lambda^{3/2}}, \tfrac{1}{x_-\lambda^{3/2}}\Bigg) \\ &\quad -\tfrac{p_+x_+\sqrt{\lambda}}{x_+\sqrt{\lambda}-1}\mathcal{J}\Bigg(\tfrac{1}{x_+^2\lambda^2}, \tfrac{1}{x_+x_-\lambda^2}\Bigg) \\ &\quad -\tfrac{p_-x_-\sqrt{\lambda}}{x_-\sqrt{\lambda}-1}\mathcal{J}\Bigg(\tfrac{1}{x_+x_-\lambda^2}, \tfrac{1}{x_-^2\lambda^2}\Bigg)\Bigg]\sqrt{O_L}, \end{aligned} \tag{3.73}$$

where

$$\begin{aligned}\mathcal{J}(x_1, x_2) &= z_s\Big[b_+\mathcal{F}_2(x_1) + b_-\mathcal{F}_2(x_2)\Big] \\ &+ z_v\Big[b_+\mathcal{F}_1(x_1) + b_-\mathcal{F}_1(x_2)\Big]. \end{aligned} \tag{3.74}$$

with $b_\pm$ as defined in Eq. (3.55).

Finally, we calculate the total weight associated with the final set of leftward steps that may be taken after the overhangs:

$$\begin{aligned}\widetilde{L'} &= \sum_{n'=0}^{\infty} wt[\mathbb{L}'(n')] = \sum_{n'=0}^{\infty} \omega(n')\lambda^{-n'/2} \\ &= \left(\frac{b_+x_+\sqrt{\lambda}}{x_+\sqrt{\lambda}-1} + \frac{b_-x_-\sqrt{\lambda}}{x_-\sqrt{\lambda}-1}\right). \end{aligned} \tag{3.75}$$

The total weight of all walks with left overhang may now be computed. Let $\mathbb{U}_L$ represent all possible walks with at least one left overhang. Let the total weight associated with these walks be U_L. Then we obtain

$$U_L = [W_L^{(1)}O_L + \mathcal{W}_L^{(2)}][1 + O_L + O_L^2 + ...][\widetilde{L'}], \tag{3.76}$$

where the second term in the right hand side represents multiple overhangs and the third term accounts for the leftward steps after the final overhang. Rewriting,

$$U_L = \Big[W_L^{(1)}O_L + \mathcal{W}_L^{(2)}\Big]\Big[\frac{1}{1-O_L}\Big]\Big[\widetilde{L'}\Big]. \tag{3.77}$$

3.4.2.3 Phase boundary

The formal generating function of all possible walks including those with overhangs may be written as

$$\mathbb{G}_{ov} = \frac{1}{1-(\mathbb{D} + \mathbb{D}\widetilde{\mathbb{R}} + \mathbb{D}\widetilde{\mathbb{L}} + \mathbb{U}_R + \mathbb{U}_L)}. \tag{3.78}$$

For every term in the expansion, one may uniquely identify a walk from top to bottom. The weighted generating function corresponding to $\mathbb{G}_{ov}$ may be written as

$$\mathcal{G}_{ov} = \frac{1}{1 - (D + D\widetilde{R} + D\widetilde{L} + U_R + U_L)} \tag{3.79}$$

As discussed earlier [see discussion following Eq. (3.46)], the generating function $\mathcal{G}_{ov}$ diverges at the transition point when the interfacial tension σ vanishes, and this condition is equivalent to

$$D + D\widetilde{R} + D\widetilde{L} + U_R + U_L = 1, \tag{3.80}$$

where D, $\widetilde{R}$, $\widetilde{L}$, U_R and U_R are given in Eqs. (3.41), (3.45), (3.65) and (3.77) respectively.

In Fig. 3.6(a), blue line represents the critical line for activity with overhang. It shows transitions at $z_s^{1/4} = 0.733$ along SV line and at $z_s^{1/4} = 0.642$ along SD line. The density plot of critical line with overhang is shown in the Fig. 3.6(b) by blue line. It shows transitions at $\rho_s = 0.934$ along SV line and at $\rho_s = 0.779$ along SD line.

3.4.3 Monte Carlo simulations

In this section we determine the phase boundary numerically using grand canonical Monte Carlo simulations. Conventional algorithms that include only local evaporation and deposition moves often do not equilibrate the system, within available computer time, at high densities due to long-lived metastable states. Here, we implement an algorithm that updates two rows at a time using a transfer matrix based Monte Carlo algorithm [8]. The algorithm not only succeeds in equilibrating the system at high densities, but also at full packing. This algorithm is a generalization of a cluster algorithm that is able to equilibrate systems of particles with large excluded volume at high densities [71, 107]. In this Monte Carlo scheme [8], all particles that are fully contained in a $2 \times L$ track, consisting of two adjacent rows or columns of length L, are evaporated. The track is refilled with particles according to the correct weights in the partition function for the track, subject to the constraints induced by particles protruding into the track. The calculation of the restricted partition function is done using standard transfer matrix technique, details of which may be found in the Supplemental Information of Ref. [8].

The order parameter Q is defined as

$$Q = \sqrt{(\rho_{er} - \rho_{or})^2 + (\rho_{ec} - \rho_{oc})^2}, \tag{3.81}$$

where ρ_{er}, ρ_{ec}, ρ_{or} and ρ_{oc} are the densities of heads of particles (including both dimers and squares) in even rows, odd rows, even columns and odd columns respectively. Consider the second moment of the order parameter Q, defined as

$$\chi = L^2 \langle Q^2 \rangle, \tag{3.82}$$

where $L \times L$ is the system size. Near the transition point χ obeys following scaling law

$$\chi \simeq L^{\gamma/\nu} f(\epsilon L^{1/\nu}), \tag{3.83}$$

where ϵ is the deviation from critical point $\epsilon = z_s - z_c$, and f is the finite size scaling function, and γ and ν are the usual critical exponents. Since the model belongs to Ashkin-Teller universality class, one knows that the exponent $\gamma/\nu = 7/4$ [8], independent of the parameters. From Eq. (3.83), we see that $\chi/L^{7/4}$ for different L should cross at $\epsilon = 0$, allowing the critical point to be estimated. An example is shown in Fig. 3.12. We fix the activity of dimer z_d and vary the activity of square z_s to get its critical value z_c. Critical value of z_0 may be obtained from the normalization condition given in Eq. (3.30). The data of full phase boundary for activity plane and density plane are shown by blue dots in Fig. 3.6(a) and Fig. 3.6(b) respectively.

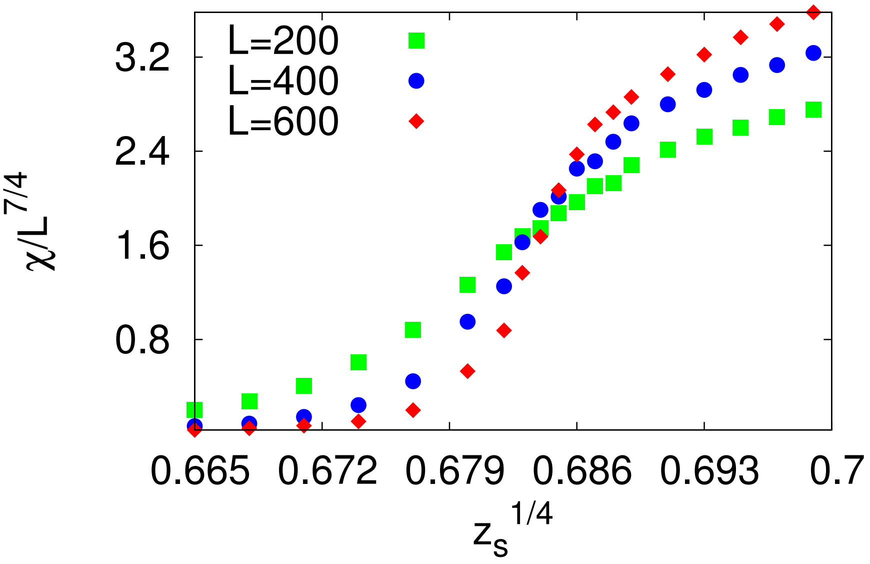

Figure 3.12: Variation of of $\chi/L^{7/4}$ with activity of squares $z_s^{1/4}$ for fixed activity of dimer $z_d = 0.031$ for different system sizes. The curves cross at $z_c^{1/4} \approx 0.684$. Critical value of z_0 may be calculated from Eq. (3.30).

3.5 Discussion

To summarize, we calculated the interfacial tension between two differently ordered phases in a mixture of hard squares and dimers, within two approximation schemes. The estimates for the phase boundary between the ordered columnar phase and disordered fluid-like or power law correlated phase was obtained by setting the interfacial tension to zero. In the first calculation, we modeled the interface as having no overhangs. The estimates were improved by extending the calculations to an interface where overhangs of height one were allowed. The estimates that we obtain for critical parameters are shown in Fig. 3.6(a) and 3.6(b), and are in good agreement with results from Monte Carlo simulations. The deviation from the numerical results are largest along the fully packed square-dimer (SD) line. Along this line, we obtain the critical parameters to be $z_s^{1/4} = 0.616$, $\rho_s = 0.714$ for interfaces without overhang, and $z_s^{1/4} = 0.642$, $\rho_s = 0.779$ for interfaces with overhangs. These are to be compared with results from Monte Carlo simulations: $z_s^{1/4} = 0.692$ and $\rho_s = 0.843$. Along the square vacancy (SV) line, the calculation reproduces the results in Ref. [7] for interfaces without overhangs, but corrects the result for interfaces with overhangs. For the latter case, it was erroneously assumed in Ref. [7] that the contributions from left and right interfaces are identical.

In our calculations we assumed that the ordered phases have perfect order, thereby ignoring the presence of defects in the bulk phases. Defects may be included in a systematic manner, as was done for the case of $2 \times d$ rectangles [7]. However, it was found that the corrections appearing from including overhangs were more dominant than that arising from including defects when d was small as is the case for hard squares. At the same time, the calculations for including defects is involved and including the effect of two defects appears a formidable task. We have, therefore, ignored the corrections due to the presence of defects.

The calculations could also be improved by taking into account multiple defects using the pairwise approximation [64]. Such an approach could improve the estimates for the phase boundary along the fully packed square-dimer line. This is a promising area for future study.

It will also be interesting to study mixtures of $m \times m$ squares and $m \times 1$ rods, $m = 2$ being the square-dimer problem. Along the fully packed line, it would be possible to map the configurations to a vector height field. The ordered phase has a $2m$ fold symmetry. This will possibly change the nature of the transition from the ordered to disordered phases. Also, along the fully packed line, it raises the possibility of an intermediate hexatic phase. For $m > 2$, the correlations even the fully packed m-mer problem is not known [66]. Thus, $m = 3$ system (trimers+squares) would be a good starting point.

Chapter 4

Hard plates on cubic lattice

4.1 Introduction

The numerical studies of HCLG models become difficult when the density is close to full packing, and/ or the excluded volume is large. We require sophisticated Monte Carlo algorithms [72, 73, 8], that implement cluster movements of particles to overcome this issue. In this chapter, we apply such an algorithm to study a collection of particles with the smallest non-trivial shape in three dimensions, namely a mixture of $2 \times 2 \times 1$ plates which could orient in any of the three orthogonal directions. The corresponding problem of plates or board-like particles in the continuum have been studied numerically [96, 97, 98]. The phase diagram of the system is very rich, showing multiple transitions with increasing particle densities, and varying aspect ratios. Different phases like smectic, biaxial smectic, uniaxial and biaxial nematic, prolate and oblate columnar etc., arise. However, less is known for the lattice model. If the orientations of the plates are restricted to the orthogonal directions, then it is possible to obtain some rigorous results regarding the nature of the phases, in particular for a system of hard parallelepipeds of size $1 \times k^{\alpha} \times k$, $\alpha \in [0, 1]$. For plate like objects ($1/2 < \alpha < 1$), it is possible to show rigorously, for $k \gg 1$, the existence of a uniaxial nematic phase, where only minor axes of plates are aligned parallel to each other, and there is no translational order [95].

A different motivation for studying plates in three dimensions arise from the corresponding problem in two dimensions. When only one kind of plate is present, then a two dimension section corresponds to the well-studied hard square model [1, 60, 63, 2, 7, 64], which undergoes a transition from disordered to columnar phase with increasing particle density. When all three kinds of plates are present, then a two dimensional section, maps onto a problem of hard squares and dimers. This model has a very rich phase diagram including two lines of critical points meeting at a point [8, 69]. Given the richness of the phase diagram, one may expect the phase diagram of plates to be also complex.

In this chapter we show that the system of hard plates on the cubic lattice undergoes two entropy driven transitions with increasing density of particles. The different phases that we observe are disordered, layered and sublattice phases. In the layered phase, in one of the three directions, particles preferentially occupies either even or odd planes, also the density of one the three types of plates is suppressed. In the sublattice phase, particles preferentially occupy one sublattice position and each type of particle breaks translational symmetry along two directions (see Sec. 4.3 for more precise definitions). The disordered to layered transition occurs at density $\rho^{DL} \approx 0.941$. From finite size scaling, we show that this transition is continuous and consistent with the universality class of three dimensional Heisenberg model with cubic anisotropy. The transition from layered to sublattice phase occurs at density $\rho^{LS} \approx 0.974$. We show that this second transition is discontinuous. The content of this chapter is under preparation.

4.2 Model & Algorithm

Consider a $L \times L \times L$ cubic lattice with periodic boundary along the three orthogonal directions. The lattice sites may be empty or occupied by $2 \times 2 \times 1$ plates. Three types of plates are possible depending on the orientation of the normal to the larger side, i.e.,

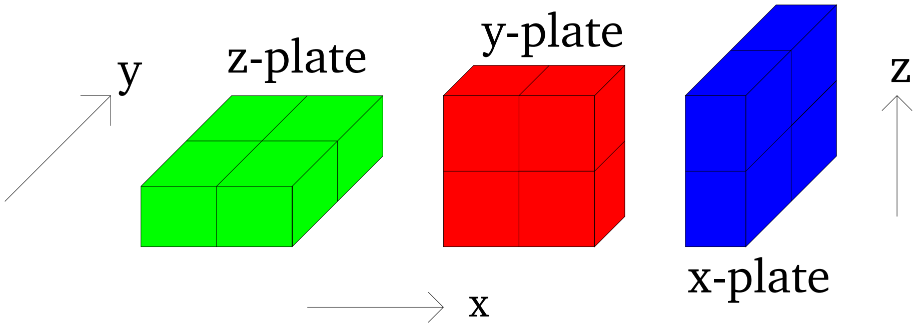

Figure 4.1: Schematic diagram of three types of particles: x-plate y-plate and z-plate having normals along three principal directions of the cubic lattice in hard plate model.

x, y and z-plates corresponding to plates lying in the yz, zx and xy planes respectively, as shown in Fig. 4.1. The plates interact through excluded volume interaction i.e., no two particles may overlap. We associate activity z_s and z_0 to each plate and vacancy respectively. These are normalised through

$$z_s^{1/4} + z_0 = 1, \tag{4.1}$$

where the power $1/4$ accounts for the volume of a plate.

We study the system using grand canonical Monte Carlo simulations. Conventional Monte Carlo simulations involving local evaporation, deposition, diffusion, and rotation moves are inefficient in equilibrating such systems especially when the packing fraction approaches full packing. These difficulties may be over come by algorithms that include cluster moves. In particular, an algorithm that updates strips of sites of size proportional to L using transfer matrices has been particularly useful for hard core lattice gas models [107, 71, 8, 77]. We briefly describe the algorithm and give details of its implementation for the system of hard plates. The implementation and terminology closely follow that followed in Ref. [8] where the phase diagram was obtained for a mixture of dimers and squares at all packing densities.

Let a track be defined as a $2 \times 2 \times L$ subsystem of the lattice, made up of L rungs of size $2\times2\times1$. Choose a track at random in any one of the three orthogonal directions. Remove all the plates that are completely contained within the track. There may be some plates that are not fully contained within the track, but partially protrude into the track. Due to this protrusion, the shape of the track (after removal of fully contained plates) is complicated and can be characterised by assigning different morphologies to each rung depending on the protrusion. There are are 16 such morphologies possible for each rung and they are listed in Fig. 4.2(a). The aim is to refill the track with a new configuration of plates that are fully contained within the track, but with the correct equilibrium probability. The probability of this new configuration may be calculated using transfer matrices. Any $2 \times 2 \times 1$ rung with a given morphology may be filled by plates in at most eight different ways. The possible states for a rung is listed in Fig. 4.2(b). Among the sixteen possible morphologies, there are fifteen morphologies with partially blocked sites. The remaining one morphology [morphology-16 as shown in Fig. 4.2 (a)] represents a complete blockage in the chosen track. We have to thus calculate $15^2 = 225$ different transfer matrices of size 8×8. Let T_{m_1,m_2} be the transfer matrix where the system is transferring from morphology m_2 to morphology m_1. The matrix element may be written as

$$T_{m_1,m_2}(i,j) = c_{m_1,m_2}(i,j) W_p W_0, \tag{4.2}$$

where $c_{m_1,m_2}(i,j)$ is the compatibility factor, W_p is the weight associated with the particle that sits on morphology m_1 and W_0 is the weight of vacancies present on morphology m_2 after depositing particle on morphology m_1. The compatibility factor $c_{m_1,m_2}(i,j)$ is 1 if the states i and j are compatible on morphologies m_1 and m_2, otherwise it equals zero. The weights associated with the particles and vacancies may be written as

$$W_p = z_s^{n_s}, \; n_s = 0, 1, 2, \tag{4.3}$$

$$W_0 = z_0^{n_0}, \; n_0 = 0, 1, 2, 3, 4. \tag{4.4}$$

Examples of few transfer matrices are given in Eqs. (4.5)–(4.7).

$$T_{1,1} = \begin{pmatrix} z_0^4 & z_0^2 & z_0^2 & z_0^2 & z_0^2 & 1 & 1 & 1 \\ z_s z_0^2 & 0 & z_s & 0 & 0 & 0 & 0 & 0 \\ z_s z_0^2 & z_s & 0 & 0 & 0 & 0 & 0 & 0 \\ z_s z_0^2 & 0 & 0 & 0 & z_s & 0 & 0 & 0 \\ z_s z_0^2 & 0 & 0 & z_s & 0 & 0 & 0 & 0 \\ z_s^2 & 0 & 0 & 0 & 0 & 0 & 0 & 0 \\ z_s^2 & 0 & 0 & 0 & 0 & 0 & 0 & 0 \\ z_s z_0^4 & z_s z_0^2 & z_s z_0^2 & z_s z_0^2 & z_s z_0^2 & z_s & z_s & z_s \end{pmatrix} \tag{4.5}$$

$$T_{1,3} = \begin{pmatrix} z_0^3 & 0 & z_0 & 0 & z_0 & 0 & 0 & 0 \\ 0 & 0 & 0 & 0 & 0 & 0 & 0 & 0 \\ z_s z_0 & 0 & 0 & 0 & 0 & 0 & 0 & 0 \\ 0 & 0 & 0 & 0 & 0 & 0 & 0 & 0 \\ z_s z_0 & 0 & 0 & 0 & 0 & 0 & 0 & 0 \\ 0 & 0 & 0 & 0 & 0 & 0 & 0 & 0 \\ 0 & 0 & 0 & 0 & 0 & 0 & 0 & 0 \\ z_s z_0^3 & 0 & z_s z_0 & 0 & z_s z_0 & 0 & 0 & 0 \end{pmatrix} \tag{4.6}$$

$$T_{3,1} = \begin{pmatrix} z_0^4 & z_0^2 & z_0^2 & z_0^2 & z_0^2 & 1 & 1 & 1 \\ 0 & 0 & 0 & 0 & 0 & 0 & 0 & 0 \\ z_s z_0^2 & z_s & 0 & 0 & 0 & 0 & 0 & 0 \\ 0 & 0 & 0 & 0 & 0 & 0 & 0 & 0 \\ z_s z_0^2 & 0 & 0 & z_s & 0 & 0 & 0 & 0 \\ 0 & 0 & 0 & 0 & 0 & 0 & 0 & 0 \\ 0 & 0 & 0 & 0 & 0 & 0 & 0 & 0 \\ 0 & 0 & 0 & 0 & 0 & 0 & 0 & 0 \end{pmatrix} \tag{4.7}$$

The partition function of a closed $2 \times 2 \times L$ track with morphology $m_1, \ldots, m_L$ may be

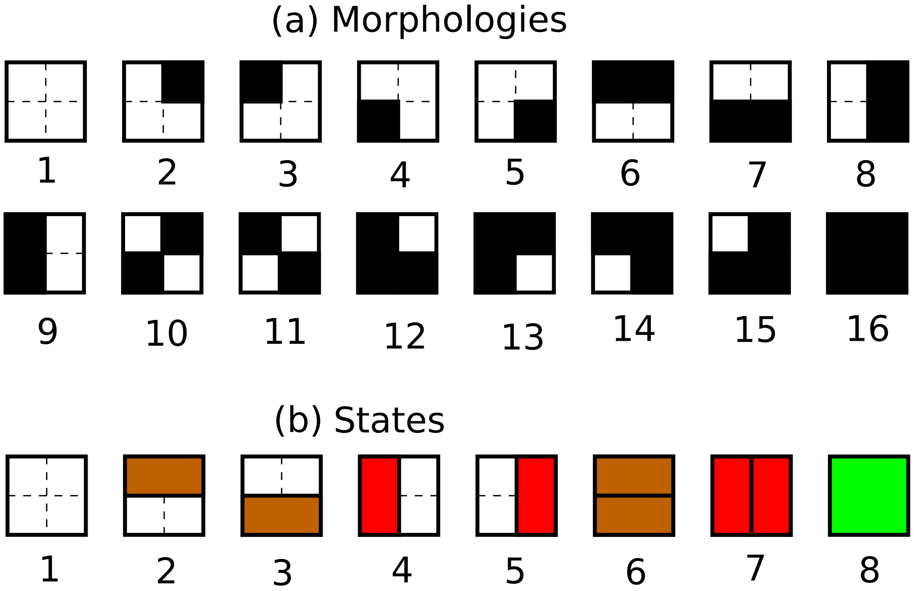

Figure 4.2: Schematic diagram of (a) sixteen possible morphologies and (b) eight possible states, that are used to construct the transfer matrix. To represent different states we have taken the projection of particles in *xy*-plane. Black represent blocked site and brown, red, green respectively represents projection of *y*, *x* and *z*-particles.

written as

$$Z^c = \sum_i \langle i | T_{m_L,m_1} T_{m_1,m_2} \ldots T_{m_{L-1},m_L} | i \rangle, \tag{4.8}$$

where $|i\rangle$ is the state vector of state i. The partition function for the open track of length $X < L$ may be written as

$$Z^o = \langle \mathcal{L}_{m_1} | T_{m_1,m_2} T_{m_2,m_3} \ldots T_{m_{X-1},m_X} | \mathcal{R}_{m_X} \rangle, \tag{4.9}$$

where $\langle \mathcal{L}_{m_1}|$ and $|\mathcal{R}_{m_X}\rangle$ are respectively left and right vectors that may be written as

$$\mathcal{L}_{m_1}(n) = T_{16,m_1}(1,n), \tag{4.10}$$

$$\mathcal{R}_{m_X}(n) = T_{m_X,16}(n,1). \tag{4.11}$$

Calculating the partition function, we deposit particles one by one in each rung so that the detailed balance is obeyed.

For each value of activity, we ensure that equilibration has been achieved by starting the

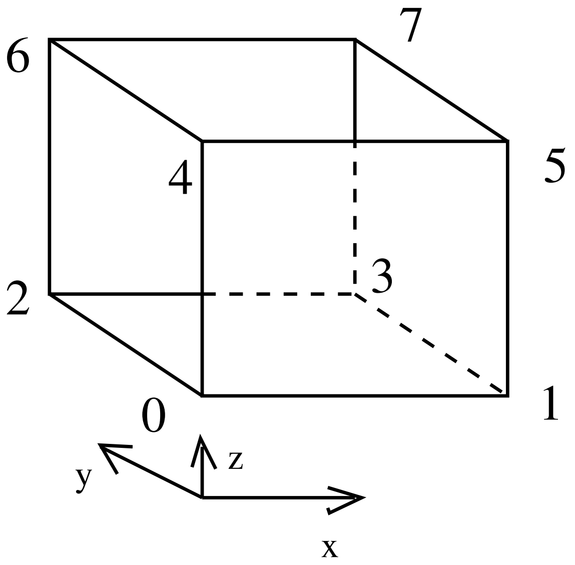

Figure 4.3: Division of the full lattice into eight sublattices $0, 1, \ldots, 7$, depending on whether each coordinate is odd or even. The arrows show the orientation of the three axes x, y and z.

simulations with configurations that correspond to different phases, and ensuring that the final equilibrium state is independent of the initial state.

4.3 Different Phases

We observe three different phases in our simulations as density is varied. To characterize them, it is convenient to divide the full lattice into eight sublattices depending on whether the x, y, and z coordinates of a site are even (0) or odd (1), as shown in Fig. 4.3. A lattice site (x, y, z) belongs to the sublattice constructed out of the binary number zyx where each coordinate is modulo two. We define the head of a particle to be at the centre of the square in the transverse direction, and the smaller of the coordinate in the perpendicular direction.

At low densities, the plates are in a *disordered phase* and the particles are uniformly distributed, i.e. each of the sublattice densities are equal for the three different types of plates. With increasing density, we observe that the system undergoes a transition into a *layered* *phase*, in which the plates preferentially occupy either even or odd planes along one of the three directions, while occupying all planes in the other two directions. Also, the symmetry among the three types of plates is broken, and the density of plates whose normal is in the direction of layering is suppressed compared to the other two types of plates. thus, translational symmetry is broken in one direction simultaneously breaking rotational and particle symmetry. The layering may be visualised through the snapshots of cross sections of the equilibrated layered phase as shown in Fig. 4.4(a)–(f), where red squares represent particles whose heads are on the plane and blue squares represent shadows or protrusions of particles whose heads are on neighbouring planes. Figure 4.4(a) and (b) are snapshots of a randomly chosen even and odd xy planes respectively. Likewise, Fig. 4.4(c) and (d) are snapshots of randomly chosen even and odd xz planes and Fig. 4.4(e) and (f) are snapshots of randomly chosen odd and even yz planes. In Fig. 4.4(a)–(d), there are approximately equal number of red and blue squares, showing both odd and even xy and xz planes are equally occupied. On the other hand, it can be seen that Fig. 4.4(e) has much larger number of red squares than blue squares and vice-versa in Fig. 4.4(f), showing that plates preferably occupy even yz planes.

To characterize the phases quantitatively, we define sublattice ρ_i^j as the volume fraction of plates of type $j = x, y, z$ whose heads are in sublattice $i = 0, \ldots, 7$. We also define three particle densities ρ^j and eight sublattice densities ρ_i as

$$\rho^j = \sum_{i=0}^{7} \rho_i^j, \; j = x, y, z, \tag{4.12}$$

$$\rho_i = \sum_{j=x,y,z} \rho_i^j, \; i = 0, \ldots, 7. \tag{4.13}$$

The time evolution of the sublattice densities, when the system is in a layered phase, with layering in x-direction, is shown in Fig. 4.5. Fig. 4.5(a) compares the densities of the three types of plates. It is clear that the density of x-plates is suppressed compared to y- and z-plates, when the layering is in the x-direction, i.e., $\rho^y \approx \rho^z \gg \rho^x$. At the same time, Fig. 4.5(b)–(d) show that while x-plates occupy all sublattices equally, y- and z- plates

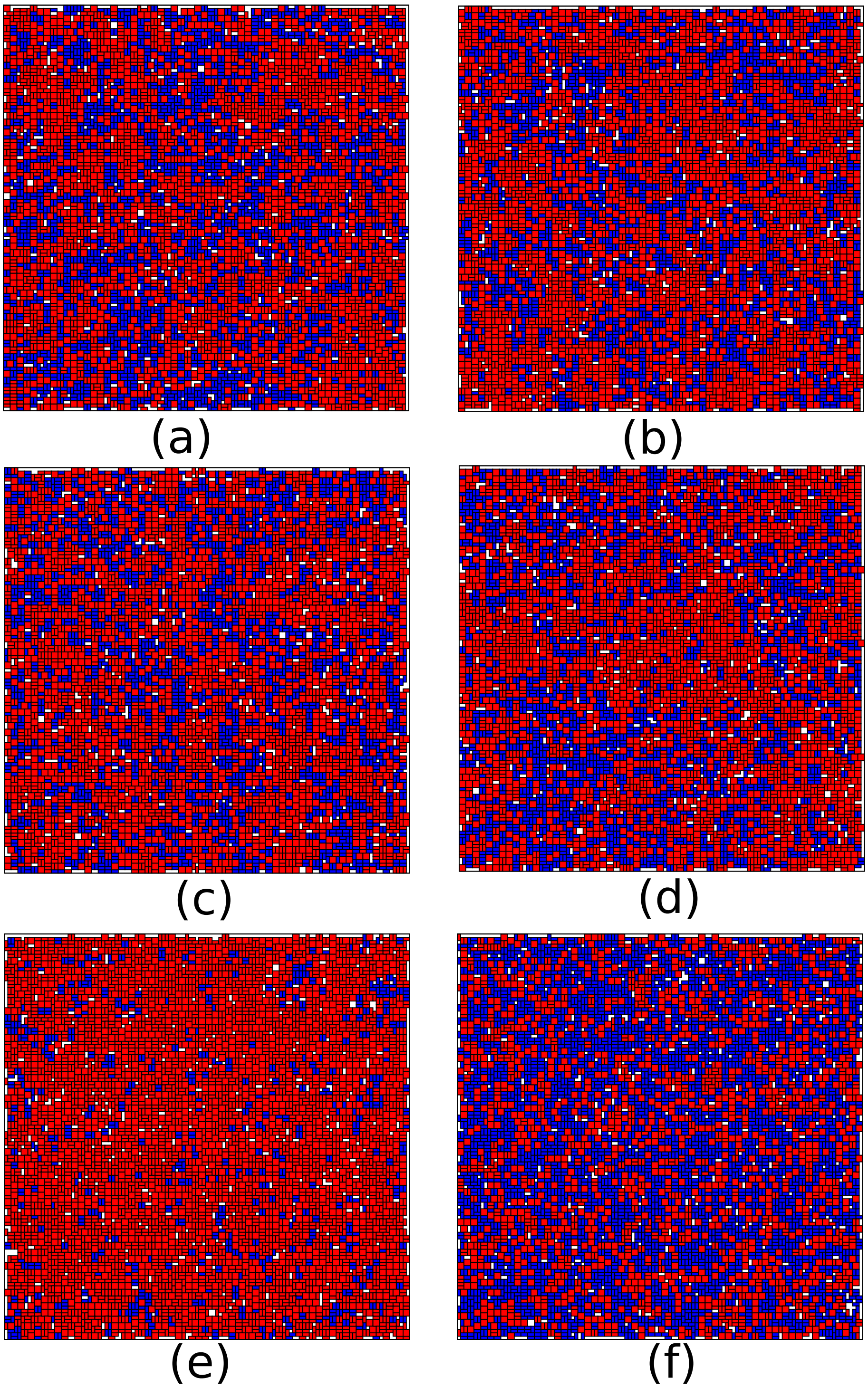

Figure 4.4: Snapshot of cross sections of equilibrated layered phase, where layering is in the x-direction, and the cross sections are of randomly chosen (a) even-xy, (b) odd-xy, (c) even-xz, (d) odd-xz, (e) even-yz and (f) odd-yz planes. Plates whose heads are on the plane are coloured in red and the projections of the plates which protrude onto the plane from nearby planes are coloured in blue. (a)–(d) look similar, while (e) is mostly red and (f) is mostly blue, showing a layering in the x-direction. The data are for system size $L = 120$ with activity $z_s = 0.380$, and density $\rho \approx 0.970$.

preferentially occupy planes with even x (corresponding to ρ_0, ρ_2, ρ_4, and ρ_6).

At higher densities including full packing, we observe a *sublattice phase*. Snapshots of six cross-sections of the system in sublattice phase is shown in Fig. 4.6(a)–(f), where grey represents the projection of particles coming from nearby plane, and eight different colours represent the particles with heads in eight different sublattices. Fig. 4.6(a) and (b) are snapshots of a randomly chosen even and odd xy planes respectively. Likewise, Fig. 4.6(c) and (d) are snapshots of randomly chosen even and odd xz planes and Fig. 4.6(e) and (f) are snapshots of randomly chosen odd and even yz planes. Fig. 4.6(a), (d) and (f) are dominated by grey particles, while very few gray particles are present in Fig. 4.6(b), (c) and (f), which indicates breaking of translational invariance in all three directions. In this phase, particle symmetry is restored, however translational symmetry is broken in two orthogonal directions by each kind of particle, and rotational symmetry is restored. Breaking of translational symmetry may be seen in the time evolution of the sublattice densities, as shown in Fig. 4.7. Fig. 4.7(a)-(c) shows the time evolution of the eight sublattice densities of individual types of plates, where we see two sublattices are preferentially occupied for each type of particles. Time evolution of the eight sublattice densities (summing over three types of particle densities at each sublattice position) is also shown in Fig. 4.8, where we see that particles preferentially occupy sublattice 3 positions. Other seven sublattice densities break up into three layers.

Also, from Fig. 4.7(a)–(c), it is clear that the three types of particles occur with the same density. To capture this broken symmetry in *sublattice phase*, it is convenient to define the quantity

$$\tilde{\eta}(k_x, k_y, k_z) = \frac{4}{L^3} \sum_{x,y,z} \eta(x, y, z) e^{i(k_x x + k_y y + k_z z)}, \tag{4.14}$$

where $\eta(x, y, z)$ is 1 if the site is occupied by the center of a plate and zero otherwise. The

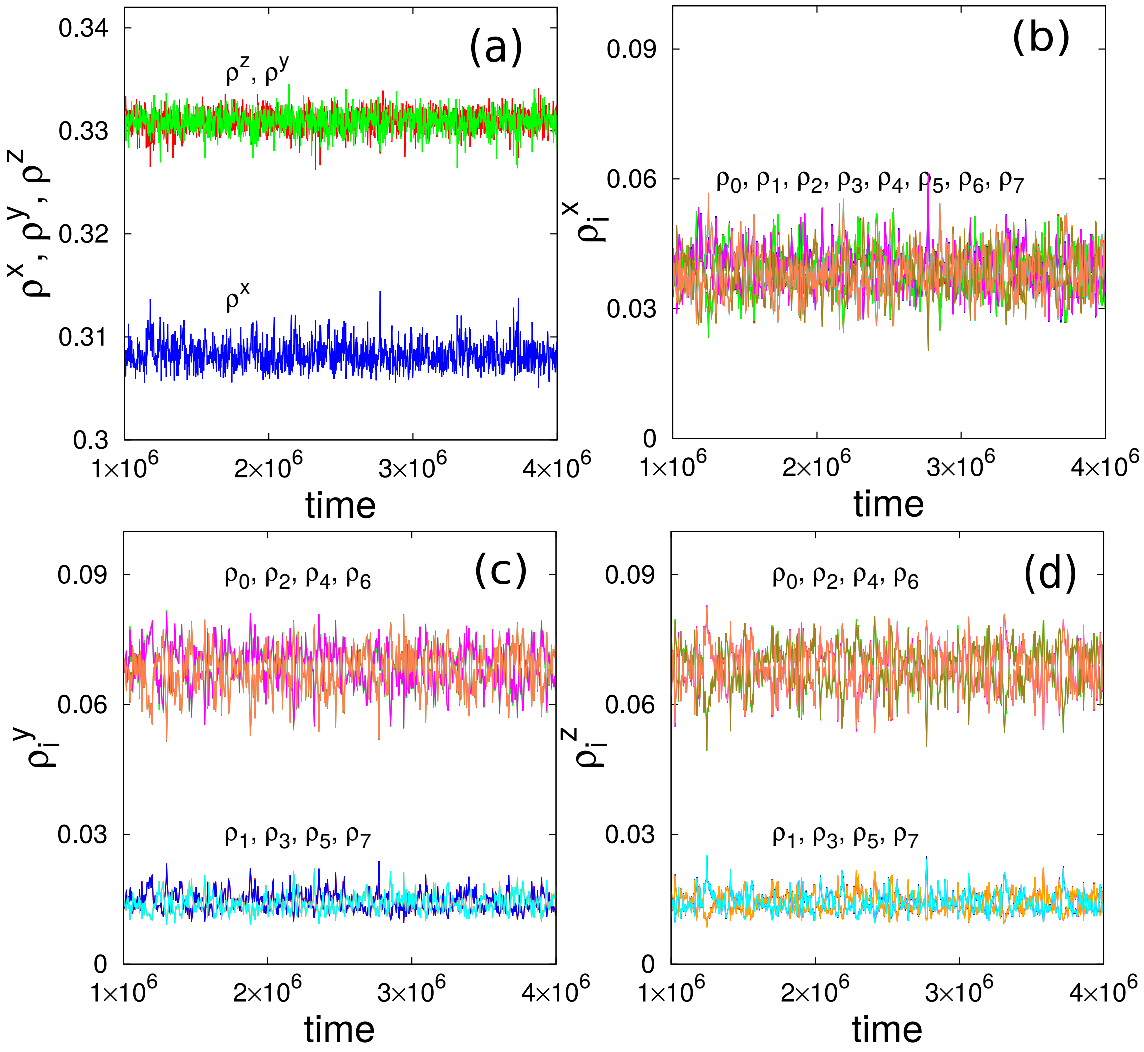

Figure 4.5: Temporal evolution of (a) three particle densities ρ^x, ρ^y, ρ^z, and eight sublattice densities (b) ρ_i^x for x-plates, (c) ρ_i^y for y-plates, (d) ρ_i^z for z-plates, where the subscripts $i = 0, \ldots, 7$ represents the sublattice positions and the superscript x, y, z represents type of plates. The time profiles are for the system in the layered phase with activity of each plate $z_s = 0.380$ and system size $L = 120$.

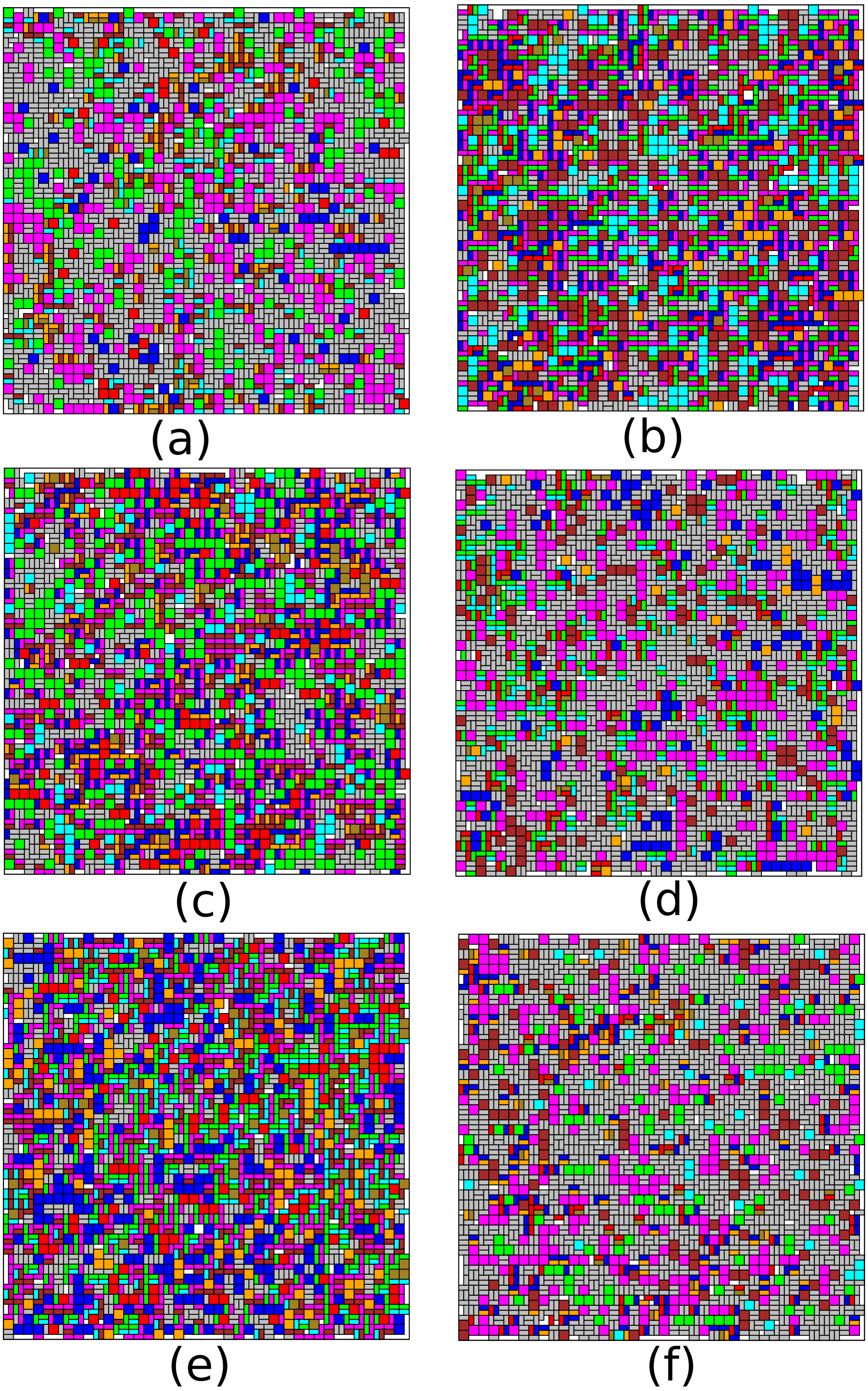

Figure 4.6: Snapshot of cross sections of equilibrated sublattice phase, where the cross sections are of randomly chosen (a) even-xy, (b) odd-xy, (c) even-xz, (d) odd-xz, (e) even-yz and (f) odd-yz planes. Grey represents the projection of particles coming from nearby plane, and eight different colors represent the particles with heads in eight different sublattices. The data are for system size $L = 120$ with activity $z_s = 0.460$, and density $\rho \approx 0.987$.

order parameters q_i for $i = 1, 2, 3$, may be defined as

$$q_1 = \sqrt{\tilde{\eta}(\pi,0,0)^2 + \tilde{\eta}(0,\pi,0)^2 + \tilde{\eta}(0,0,\pi)^2}, \tag{4.15}$$

$$q_2 = \sqrt{\tilde{\eta}(0,\pi,\pi)^2 + \tilde{\eta}(\pi,0,\pi)^2 + \tilde{\eta}(\pi,\pi,0)^2}, \tag{4.16}$$

$$q_3 = |\tilde{\eta}(\pi,\pi,\pi)|. \tag{4.17}$$

Time evolution of order parameters q_2 and q_3 are shown in Fig. 4.7(d), where we see that q_2 is non-zero whereas q_3 is exactly zero in sublattice phase.

In our simulations ranging up to the fully packed system, we do not observe any other phases other than those listed above.

4.4 Phase transitions

In this section, we study the nature of the disordered-layered and layered-sublattice phase transitions.

4.4.1 Disordered to Layered Transition

To capture the symmetry breaking in the different transitions, we consider the order parameter q_1, q_2, and q_3 as defined in Eqs. (4.15)–(4.17). In the disordered phase all three translational order parameters $q_i \approx 0$, $i = 1, 2, 3$, while in a pure layered phase $q_1 \approx 1$ and $q_2 \approx q_3 \approx 0$. On the other hand, since each type of particle breaks translational invariance along two directions, in a pure sublattice phase $q_2 \approx 1$ and $q_3 \approx 0$. The variation of q_i for $i = 1, 2, 3$ with activity z_s for different system size is shown in Fig. 4.9(a). We clearly observe a layered phase ($q_1 \neq 0$, $q_2 = 0$, $q_3 = 0$) and a sublattice phase ($q_1 \neq 0$, $q_2 \neq 0$, $q_3 = 0$).

We also define the nematic order parameter q_n to capture the breaking of particle number

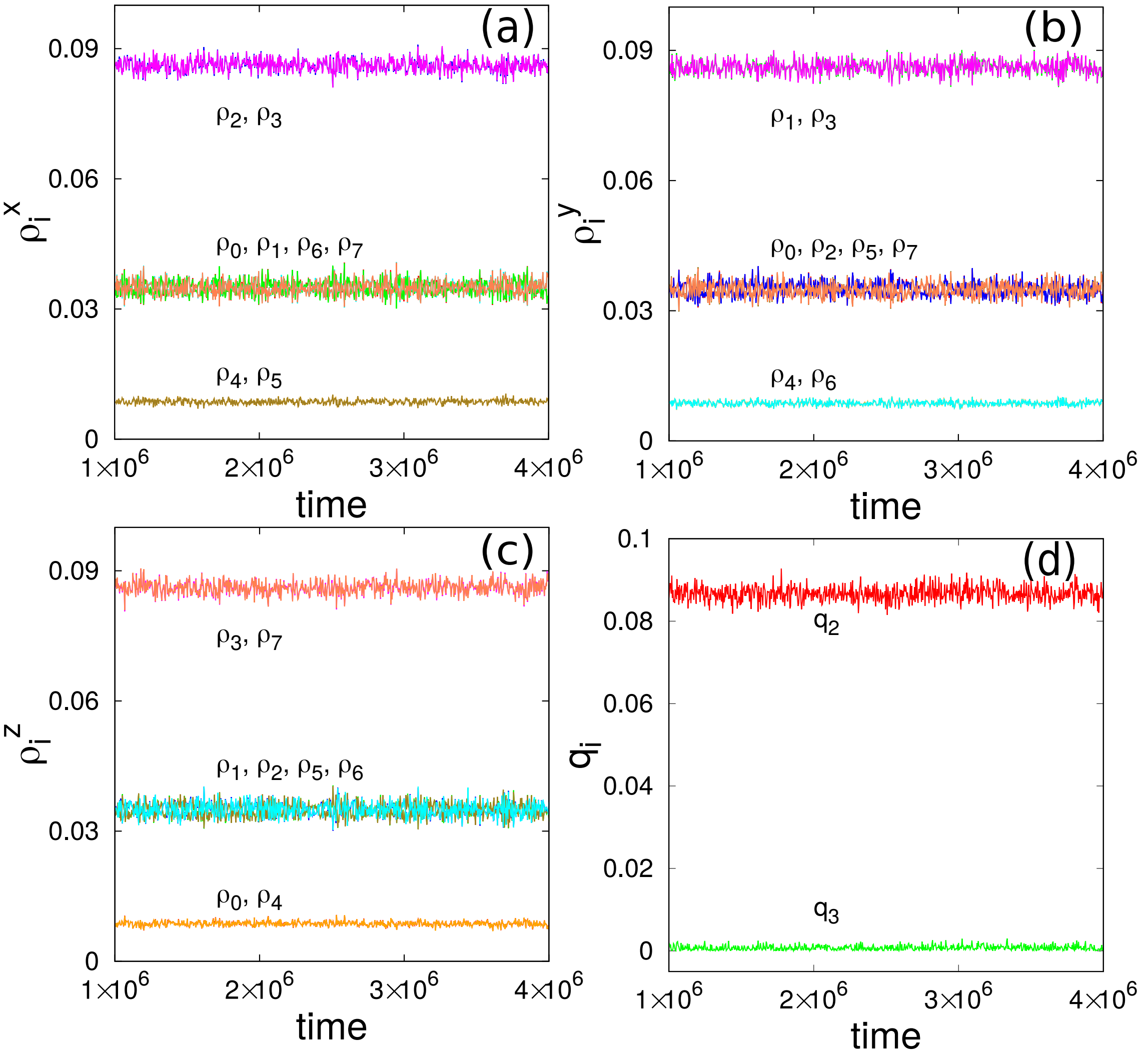

Figure 4.7: Temporal evolution of eight sublattice densities: (a) ρ_i^x for x-plates, (b) ρ_i^y for y-plates, (c) ρ_i^z for z-plates and (d) order parameter q_k, with $k = 2, 3$, where the subscripts $i = 0, \ldots, 7$ represents the sublattice positions and the superscript x, y, z represents type of plates. The time profiles are for the system in the sublattice phase with activity of each plate $z_s = 0.460$ and system size $L = 120$.

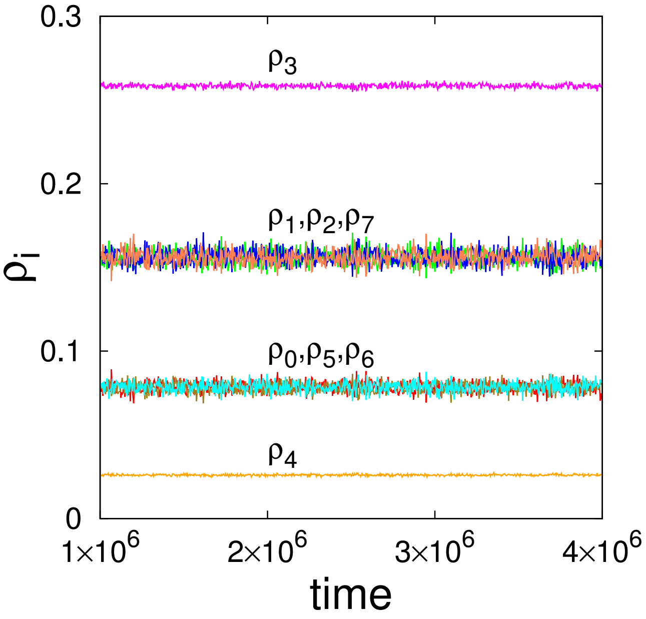

Figure 4.8: Temporal evolution of eight sublattice densities in the sublattice phase for activity of each plate $z_s = 0.460$ and system size $L = 120$.

symmetry. The order parameter q_n is defined as

$$Q_n = q_n e^{i\theta_p} = \rho^z + \rho^y e^{i\frac{2\pi}{3}} + \rho^x e^{i\frac{4\pi}{3}}. \tag{4.18}$$

The variation of q_n as a function of z_s is shown in Fig. 4.9(b). q_n is zero in both disordered and sublattice phase, and takes nonzero values only in the layered phase, which indicates asymmetric densities of three types of particles in the layered phase.

We now study the disordered-layered transition using the order parameter q_1. We define the susceptibility χ_i and Binder cumulant u_i associated with q_i, and compressibility κ as

$$\chi_i = L^3(\langle q_i^2\rangle - \langle q_i\rangle^2), i = 1, 2, n, \tag{4.19}$$

$$u_i = 1 - c_i\frac{\langle q_i^4\rangle}{\langle q_i^2\rangle^2}, i = 1, 2, n, \tag{4.20}$$

$$\kappa = L^3(\langle \rho^2\rangle - \langle \rho\rangle^2), \tag{4.21}$$

where $c_1 = 9/15$ and $c_2 = c_n = 1/2$, and n refers to nematic. We study the critical behaviour using finite size scaling. Near the critical point, it is well known that the singular

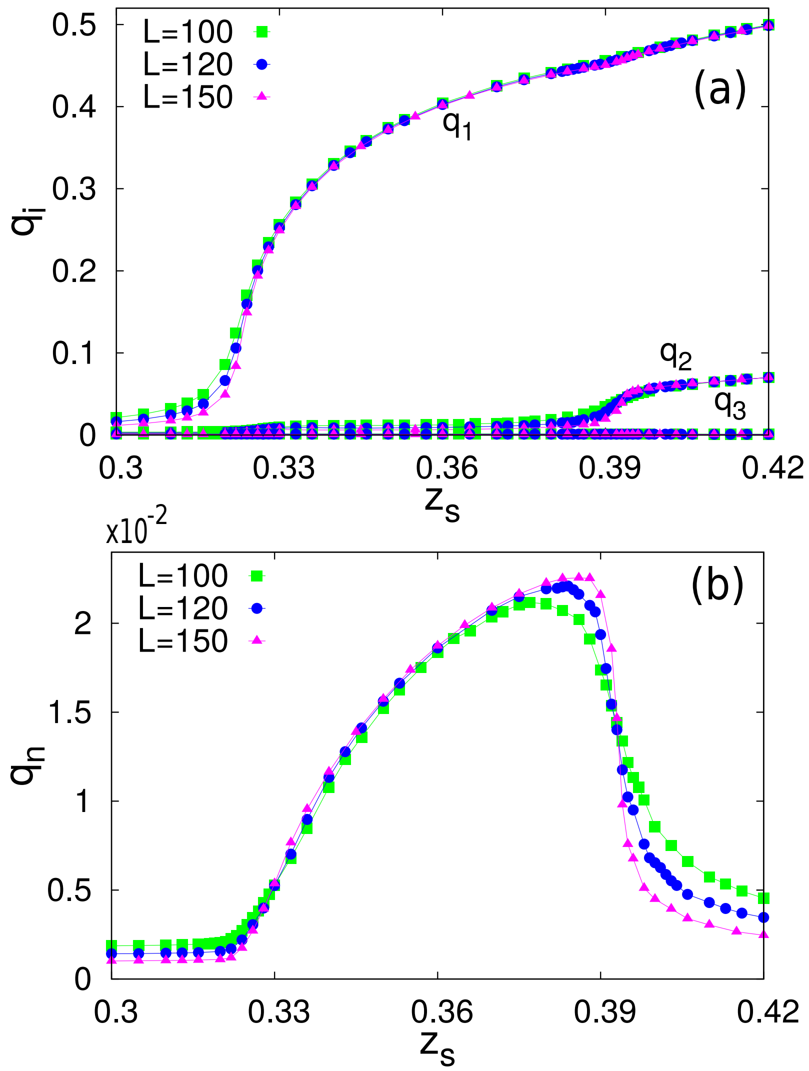

Figure 4.9: Variation of (a) translational order parameters q_1, q_2, q_3, and (b) nematic order parameter q_n with activity of plate z_s. The data are for for system sizes $L = 100, 120, 150$.

part of the different thermodynamic quantities obey

$$u_i(\epsilon, L) \simeq f_u(\epsilon L^{1/\nu}), \tag{4.22}$$

$$q_i(\epsilon, L) \simeq L^{-\beta/\nu} f_q(\epsilon L^{1/\nu}), \tag{4.23}$$

$$\chi_i(\epsilon, L) \simeq L^{\gamma/\nu} f_\chi(\epsilon L^{1/\nu}), \tag{4.24}$$

where $\epsilon = z_s - z_c$ is the deviation from the critical point, β, γ, and ν are critical exponents, and f_u, f_q, and f_χ are scaling functions.

We now show that the data near the disordered-layered transition are consistent with the universality class of three dimensional Heisenberg model with cubic anisotropy having critical exponents $\nu = 0.704, \beta = 0.362$, and $\gamma = 1.389$. The variation of u_1 with z_s for different system sizes is shown in Fig. 4.10(a). The data for different system sizes cross each other at the critical point $z_s^{DL} \approx 0.323$. The data for different L collapse onto one curve when the variables are scaled as in Eq. (4.22) with $\nu = 0.704$, as shown in Fig. 4.10(b). From Fig. 4.10(c), we obtain that the corresponding critical density is $\rho^{DL} \approx 0.940$. The data for different system sizes for q_1 [see Fig. 4.10(d)], χ_1 [see Fig. 4.10(e)] collapse onto a single curve when the thermodynamic variables are scaled as in Eqs. (4.23)–(4.24) with exponents $\nu = 0.704$, $\beta = 0.362$, and $\gamma = 1.389$. From the excellent data collapse, we conclude that the transition, most likely, belongs to the universality class of the three dimensional Heisenberg model with cubic anisotropy.

4.4.2 Layered to Sublattice Transition

In this section, we study the nature of the second transition from layered to sublattice phase. Suitable order parameters are q_2 and q_n as defined in Eqs. (4.16) and (4.18) respectively. The associates susceptibility and Binder cumulants are defined in Eqs. (4.19) and (4.20) respectively. We show that the transition is discontinuous.

The variation of q_2 and q_n with z_s, for different system sizes, is shown in Fig. 4.11(a)

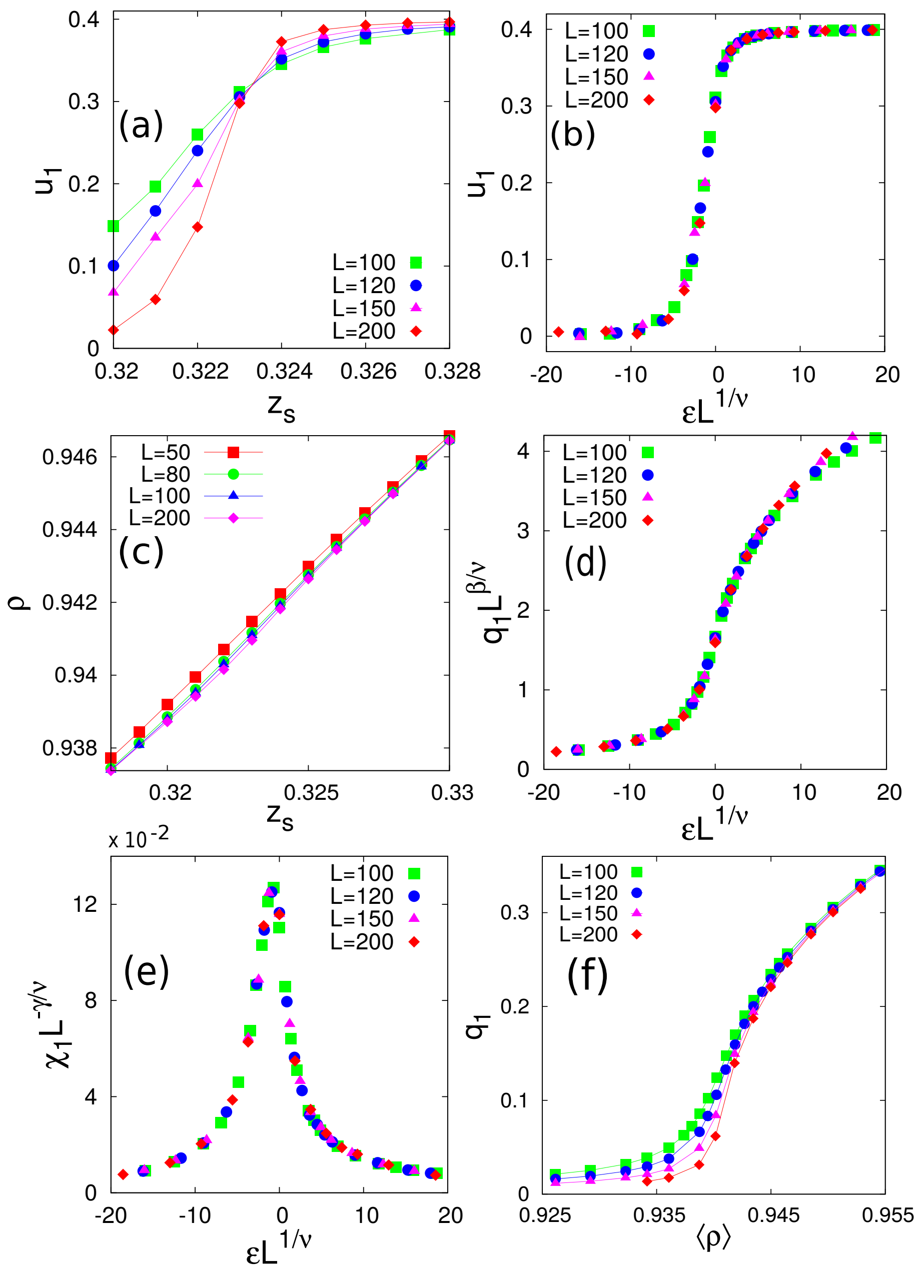

Figure 4.10: Data for different thermodynamic quantities near the disordered-layered transition. (a) Binder cumulant u_1 for different system sizes intersect close to $z_s^{DL} \approx 0.323$. (b) The Binder cumulant for different system sizes collapse onto a curve when the parameter are scaled as in Eq. (4.22). (c) Variation of average density $\langle\rho\rangle$ with z_s. The data for different system sizes for (d) order parameter q_1 and (e) susceptibility χ_1 collapse onto a single curve when the data are scaled as in Eqs. (4.23)– (4.24) with exponents $\nu = 0.704$, $\beta = 0.362$, and $\gamma = 1.389$. (f) Variation of q_1 as a function of average density $\langle\rho\rangle$.

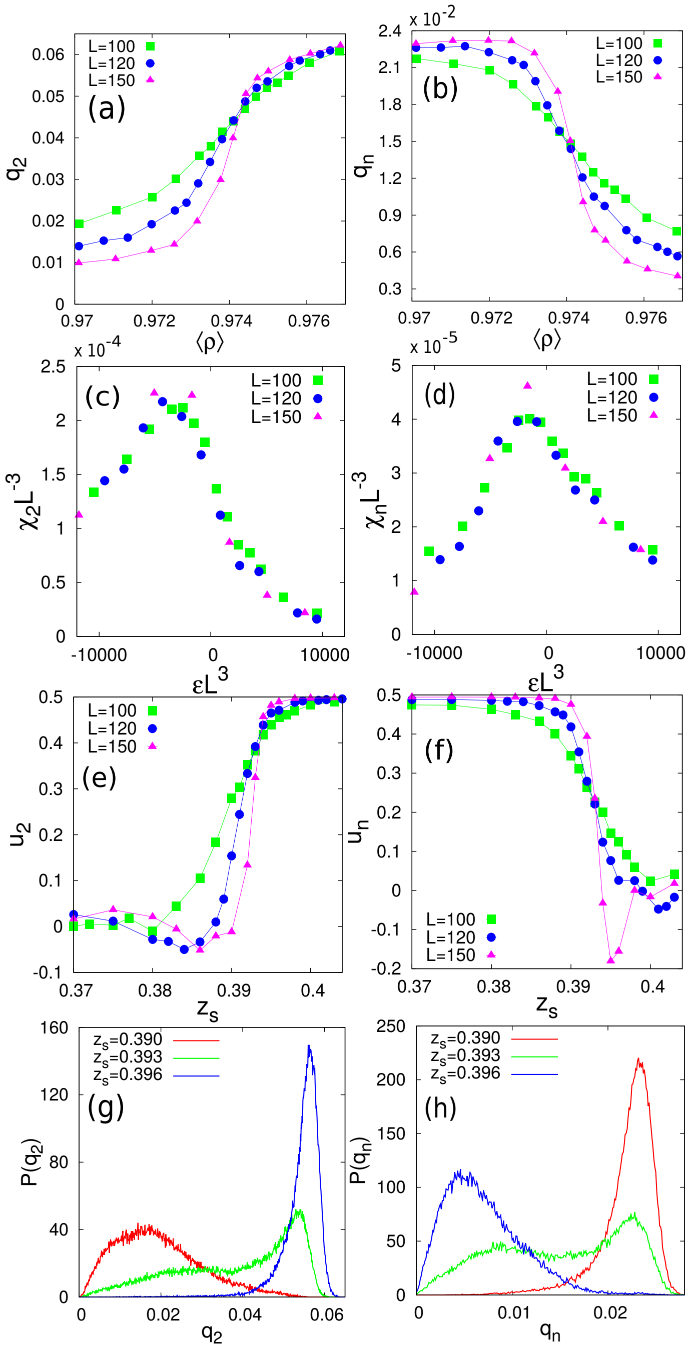

Figure 4.11: Data for different thermodynamic quantities near the layered-sublattice transition. The variation of the order parameters (a) q_2 and (b) q_n with density for different system sizes. The different curves intersect each other and become steep with increasing system size. (c) and (d): The data for susceptibility for different system sizes collapse onto a curve when scaled as shown in the figure. (e) and (f) Binder cumulants for different system sizes. The cumulants become negative near the transition. (g) and (h): The probability distributions for the order parameters close to the transition point for $L = 150$.

and (b) respectively. We observe that both order parameters have a sharp variation across the transition point, and the data for different system sizes intersect each other with the curves becoming steeper with increasing system size. These are signatures of a discontinuous transition. More evidence of the discontinuous nature may be found by examining susceptibility and Binder cumulants. The data for susceptibility for different system sizes collapse onto a curve [see Fig. 4.11(c) and (d)] with the following scaling: χL^{-3} and ϵL^3, as expected for a first order transition, where $z_s^{LS} \approx 0.393$ and $\rho^{LS} \approx 0.974$. The variation of Binder cumulant u_2 and u_n are shown in Fig. 4.11(e) and (f) respectively, for different system sizes. Clearly, both cumulants negative near the transition, a clear signature of a first order transition. Finally, as in a discontinuous transition, we see the typical double peaked distribution for the order parameters as the activity crosses the critical activity, showing coexistence [see Fig. 4.11(g) and (h)]. The jump in density across the transition is presumably small because we are unable to detect it upto a system size $L = 200$. We, thus, conclude that the layered-sublattice transition is discontinuous.

4.5 Summary and discussion

In this chapter we studied the phases and phase transitions in a system of $2 \times 2 \times 1$ hard plates on the three dimensional cubic lattice using Monte Carlo simulations. Three types of plates are possible depending on its orientation. We showed, that the system undergoes two entropy driven transitions with increasing density of particles: first from disordered to layered and second from layered to sublattice, as shown in Fig. 4.12. In the fully packed limit, the system has sublattice order. We showed that the disordered to layered transition is continuous and the critical behaviour is consistent with the universality class of the three dimensional Heisenberg model with cubic anisotropy. On the other hand, we find the transition from layered to sublattice phase is discontinuous.

In the layered phase, the density of one type of plate is suppressed, and translational

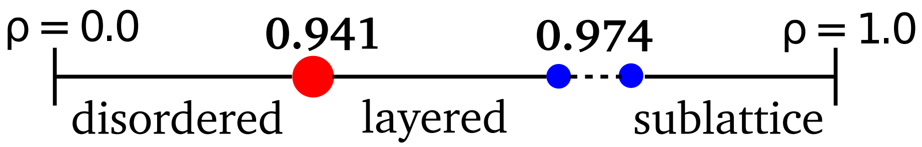

Figure 4.12: Schematic phase diagram of 2 × 2 × 1 hard plate model. Red dot represent second order transition and dotted line represent first order transition.

symmetry is broken in only direction. This phase is similar to the biaxial smectic phase seen in simulations of hard boards in the continuum [96]. In the sublattice phase, the system has translational order in two of the three directions. Each type of particle has sublattice order in the direction normal to the plane of the particle. On the other hand, if one looks at the densities of sublattices [see Fig. 4.7], then one sublattice is preferentially occupied, as in crystalline-sublattice order. However, the order parameter q_3 is zero for all densities, while q_2 is non-zero for the sublattice phase, showing that crystalline order is not present.

Although, numerous analytical [108, 109, 95], experimental [110, 111] and computer simulation [112, 113, 98] studies indicate the presence of biaxial nematic phase in the system of anisotropic plate like objects in three dimensions, there is long standing debate regarding the existence of this phase. In this study we have not found any biaxial nematic phase in the system of plates with side length $k = 2$. It would be very interesting to check the existence and stability of biaxial nematic phase for the lattice models of plates with larger side length. The system of rectangular plates with different aspect ratio having hard core and/or attractive interaction are also promising area for future study.

A two dimensional section of the system of hard plates corresponds to a problem of hard squares and dimers. This model, when the activities of dimers and squares can be varied independently, has a very rich phase diagram including two lines of critical points meeting at a point [8, 69]. Thus, one can expect that if the activities of the three kinds of plates in three dimensions can be independently varied, then a very rich phase diagram can be expected, especially at full packing, where regions of power-law correlated phases should exist.

Chapter 5

Y-shaped particles on triangular lattice

5.1 Introduction

In this chapter, we determine the different phases and nature of the phase transitions for the system of hard Y-shaped particles on the triangular lattice. We study the system by considering excluded volume interactions between particles which corresponds to the infinite temperature limit of the model studied in Refs. [16, 15]. We show that the sublattice phase at high densities which breaks particle symmetry is unstable to a sliding instability in the presence of vacancies. This results in the phase near full packing having columnar order, where there is translational order only in one of the three directions. This phase also has roughly equal number of both types of particles. In the presence of attractive interactions between the arms of the particles, we argue, using a high density expansion at finite temperatures, that this result continues to hold. Thus, irrespective of whether attractive interactions are present, neither does the high density phase have sublattice order nor is there a critical temperature above which there is no phase transition in contradiction to the results reported in Refs. [16, 15]. We also demonstrate the presence of an intermediate phase, and that there are two entropy-driven phase transitions with increasing density of particles: first from a disordered phase to an intermediate density sublattice phase where the symmetry between the two kinds of particles are broken and second from the sublattice phase to a high density columnar phase where the symmetry between the two types of particles is restored. In addition, we also study the special case of the model when only one kind of Y-shaped particle is present, and show that it undergoes a single first order transition from a disordered phase to an ordered sublattice phase. The content of this chapter is published in Ref. [114].

5.2 Model and algorithm

Consider a two dimensional triangular lattice of linear dimension L with periodic boundary, as shown in Fig. 5.1(a). A lattice site may be empty or occupied by one of two types of particles. Particles are Y-shaped and occupy four lattice sites, consisting of a central site and three of its six neighbors chosen alternately. The three neighbors can be chosen in two different ways, and hence there are two types of particles, examples of which are shown in Fig. 5.1(a). We will refer to the two types as A- and B-type particles. The particles interact through excluded volume interaction, i.e., a site may be occupied by at most one particle. Activities $z_A = \exp(\mu_A)$ and $z_B = \exp(\mu_B)$ are associated with each A- and B-type particle respectively, where μ_A and μ_B are the reduced chemical potentials. We will refer to the central site of a particle as its head.

We study the system using grand canonical Monte Carlo simulations. Conventional algorithms involving local evaporation and deposition of a single particle are inefficient in equilibrating the system at densities close to full packing. We implement an improved version of a recently introduced algorithm with cluster moves that is able to efficiently equilibrate systems of particles with large excluded volume interactions at densities close to full packing [107, 71], as well as at the fully packed density [8].

We briefly describe the algorithm. First, a row is chosen at random (the row can be in any of the three directions of the triangular lattice). Then all the A-type (or equivalently

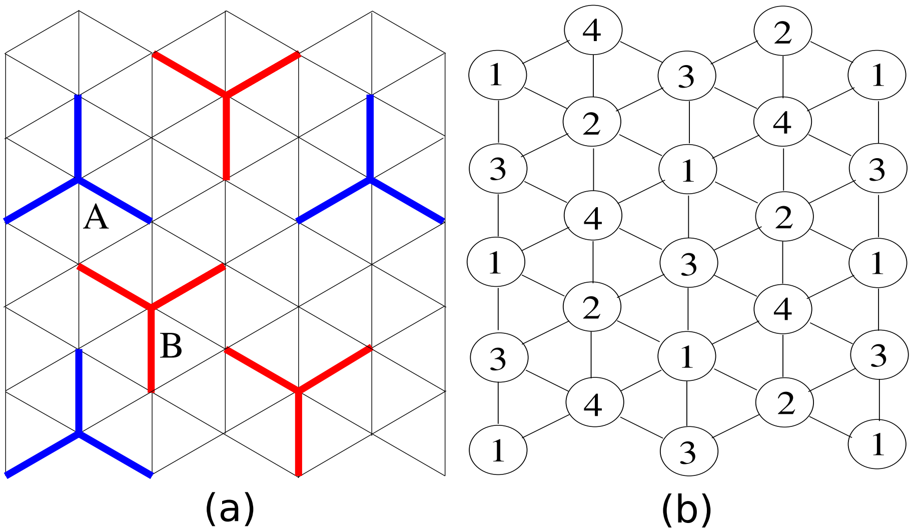

Figure 5.1: (a) Schematic diagram of a triangular lattice and the two types of Y-shaped particles. A- and B-type particles are represented by blue and red colors respectively. (b) The lattice sites are labeled as $1, 2, 3, 4$ depending on the sublattice they belong to.

B-type) particles with heads on this row are evaporated. The row now consists of empty intervals separated from each other by B-type particles with heads on the same row as well as A- and B-type particles with heads on neighbouring rows. These empty intervals are now re-occupied with A-type particles with the correct equilibrium probabilities. The calculation of these probabilities reduces to determining the partition function of a one-dimensional system of dimers. Details may be found in Refs. [107, 71, 77, 8]. For each row, we choose at random whether A- or B-type particles are to be evaporated. A Monte Carlo move is completed when $3L$ rows are updated.

Though the above algorithm is able to equilibrate the system at densities close to full packing, we find that the equilibration times as well as the autocorrelation times are large. In order to improve the efficiency of the algorithm, we introduce a sliding move in addition to the evaporation-deposition move. The first step in the sliding move is to select a site at random. If the site is not occupied by the head of a particle, then another site is chosen. If the site is occupied by the head of a particle, then one direction out of six possible directions is chosen, and we identify a cluster of same type of particles, defined as a set of consecutive particles separated by two sites, starting from the randomly chosen site

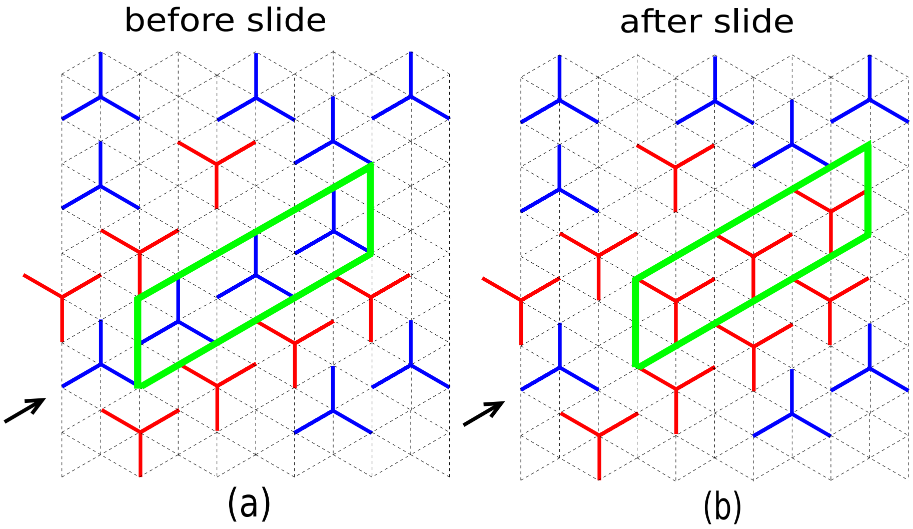

Figure 5.2: Schematic diagram to illustrate the sliding move. A cluster is identified [highlighted box in (a)] by choosing randomly a site and one of the six directions (shown by arrow). The cluster is slid by one lattice site in the chosen direction and the particle type is switched from $A \leftrightarrow B$ to obtain a new configuration as shown in (b).

along the chosen direction. An example of such a cluster is shown by the highlighted box in Fig. 5.2(a). The cluster of particles is slid by one lattice site in the chosen direction and the particle type is changed from $A \leftrightarrow B$ [see Fig. 5.2(b)]. The new configuration is accepted if it does not violate the hard core constraint. It is straightforward to confirm that the sliding move obeys detailed balance as the reverse move occurs with exactly the same probability. A Monte Carlo move is completed when $3L$ rows are updated through the evaporation-deposition and $L^2/10$ sliding moves are attempted. We have chosen a ratio of sliding to evaporation/deposition moves that is efficient but have not optimized the ratio.

We compare the efficiency of the algorithm with and without the sliding move in Fig. 5.3. Starting from a disordered phase, the system is evolved in time at a value of chemical potential $\mu = \mu_A = \mu_B$ for which the equilibrium density is high (≈ 0.967), and the system is ordered. From Fig. 5.3, we see that the density reaches the equilibrium value in 10^5 steps when the sliding move is present compared to 4×10^6 steps when the sliding move is absent. Second, we calculate the density-density autocorrelation function, defined as

$$C(t) = \frac{\langle \rho(t+t_0)\rho(t_0)\rangle - \langle \rho \rangle^2}{\langle \rho^2 \rangle - \langle \rho \rangle^2}, \tag{5.1}$$

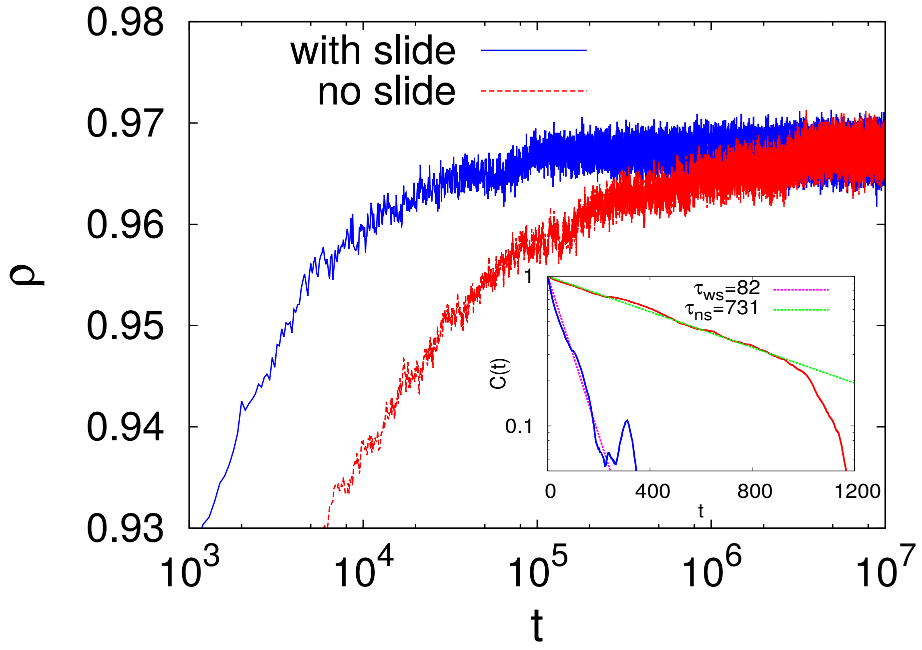

Figure 5.3: The increase in density ρ to its equilibrium value for a system of size $L = 300$ and $\mu = \mu_A = \mu_B = 6.0$ for the algorithms with (blue) and without (red) the sliding move. The initial condition is disordered and the equilibrium configuration has $\rho \approx 0.967$, and is ordered. Logarithmic scale has been used for the t-axis. Inset: Equilibrium density-density autocorrelation function $C(t)$ as a function of time t. When fitted to an exponential as in Eq. (5.2), we obtain $\tau_{ws} \approx 82$ when the sliding move is present and $\tau_{ns} \approx 731$ when the sliding move is absent.

where $\rho(t)$ is the density at time t, and the average is over t_0. We determine the autocorrelation time τ by fitting the correlation function to an exponential

$$C(t) \approx e^{-t/\tau}. \tag{5.2}$$

From the inset of Fig. 5.3, we find the autocorrelation time, τ_{ws}, for the algorithm with sliding move is $\tau_{ws} \approx 82$, while the autocorrelation time, τ_{ns}, for the algorithm with no sliding move is $\tau_{ns} \approx 731$. Thus, the inclusion of the sliding move results in considerable shorter equilibration times as well as autocorrelation times, and results in much better statistics. We have also checked that the autocorrelation function is independent of different choices of t_0, showing that time translational invariance has been achieved and the system has equilibrated.

The evaporation and deposition of particles along a row depends only on the configuration of the four neighbouring rows. Thus, rows that are separated by three can be updated simultaneously, and the implementation of the algorithm is easily parallelizable. All the results presented in this paper are obtained using the parallelized algorithm. Equilibration is checked by starting the simulations with different initial conditions, corresponding to different phases, and confirming that the equilibrated phase is independent of the initial condition.

5.3 One type of particle ($\mathbf{z_A = 0}$)

We first obtain the phase diagram for the case when only B-type particles are present, corresponding to $z_A = e^{\mu_A} = 0$ and $z_B = e^{\mu_B} > 0$. To demonstrate the different types of phases present in the system, we divide the lattice into four sublattices as shown in Fig. 5.1(b). A particle occupies four sites that belong to four different sublattices. We color the four sites occupied by a particle by one of four colors depending on the sublattice that the head of the particle belongs to. Snapshots of typical equilibrated configurations are shown in Fig. 5.4 for both small densities [Fig. 5.4(a)] and high densities [Fig. 5.4(b)]. From the snapshots, it is clear that at small densities, all four colors are roughly equally present. We will refer to this phase as the disordered phase, in which

$$\rho_1^B \approx \rho_2^B \approx \rho_3^B \approx \rho_4^B, \ \text{disordered phase}, \tag{5.3}$$

where ρ_i^B is the fraction of sites in sublattice i that are occupied by B-type particles.

The snapshot of the system at higher densities, as shown in Fig. 5.4(b) is predominantly of one color, implying that the heads of the particles preferably occupy one of the four sublattices. We will refer to this solid-like phase as the sublattice phase. The sublattice phase has translational order.

To quantify the phase transition from the disordered phase to sublattice phase, we define

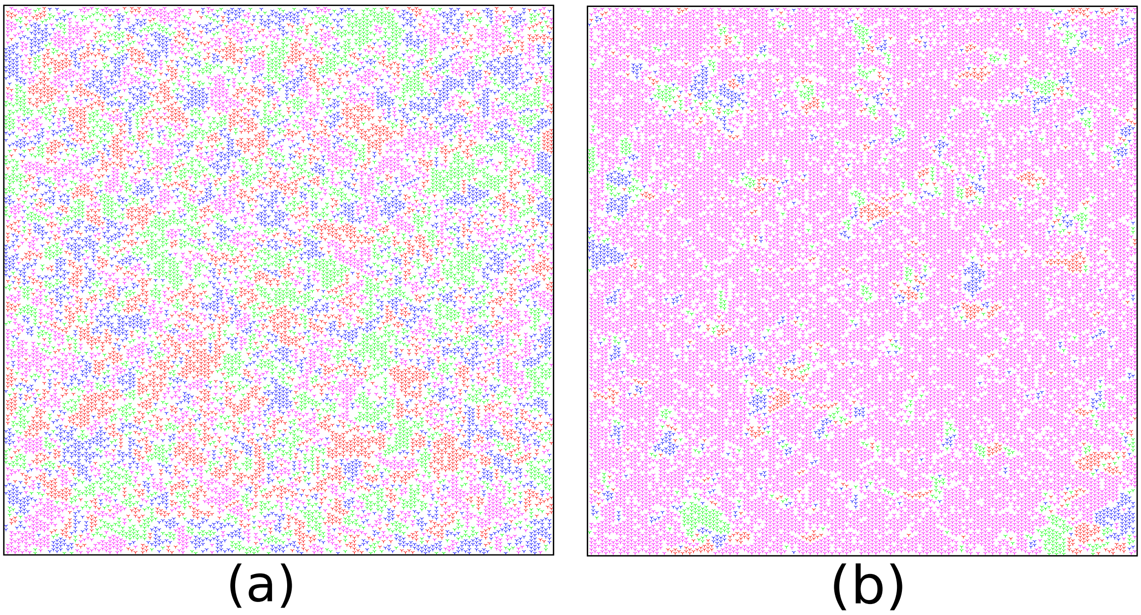

Figure 5.4: Snapshot of typical equilibrated configurations of the system obtained from *grand canonical* Monte Carlo simulations with only one type of particle ($z_A = 0$) for two different values of chemical potential: (a) disordered phase at $\mu_B = 1.420$ ($\rho^B \approx 0.710$) and (b) sublattice phase at $\mu_B = 1.765$ ($\rho^B \approx 0.775$). The particles on the four sublattices 1, 2, 3 and 4 are represented by green, red, blue and magenta respectively. The data are for a system of size $L = 300$.

the vector

$$\mathbf{Q}^B = |\mathbf{Q}^B| e^{i\theta_B} = \sum_{n=1}^{4} \rho_n^B e^{i(n-1)\pi/2}, \tag{5.4}$$

where the sublattice densities ρ_i^B are as defined in Eq. (5.3). We define the sublattice order parameter Q^B to be

$$Q^B = \langle |\mathbf{Q}^B| \rangle, \tag{5.5}$$

where the average $\langle \ldots \rangle$ is over equilibrium configurations. Clearly, Q^B is zero in the disordered phase and non-zero in the sublattice phase.

The variation of Q^B with chemical potential μ_B is shown in Fig. 5.5(a) for different system sizes. It increases sharply from zero to a non-zero value as μ_B crosses a critical value $\mu_{Bc} \approx 1.75$ and critical density $\rho_c^B \approx 0.750$. The transition becomes sharper with increasing system size. The total density of the system ρ^B has a system size dependence for intermediate densities [see Fig. 5.5(b)]. We also study the Binder cumulant U^B defined as

$$U^B = 1 - \frac{\langle |\mathbf{Q}^B|^4 \rangle}{2\langle |\mathbf{Q}^B|^2 \rangle^2}. \tag{5.6}$$

The variation of U^B with μ_B is shown in Fig. 5.5(c) for three different system sizes. For small μ_B, it is zero for the disordered phase and close to 0.5 for the ordered phase as expected. Near the transition point, U^B becomes negative and the minimum value decreases with increasing system size. This is a clear signature of a first order transition, as for a continuous transition U^B is positive and the data for different system sizes intersect at the critical point. We conclude that the transition is first order. Now, consider the susceptibility χ defined as

$$\chi = L^2(\langle |\mathbf{Q}^B|^2 \rangle - Q^{B2}). \tag{5.7}$$

For a first order transition, the singular behaviour of χ near the transition obeys the finite size scaling $\chi \sim L^2 f[(\mu_B - \mu_{Bc})L^2]$, where f is a scaling function. The data for χ for different system sizes collapse onto one curve when scaled as above with $\mu_{Bc} \simeq 1.756$ as shown in Fig. 5.5(d).

We now give further evidence of the transition being first order. At a first order phase transition, the system keeps transiting from the disordered phase to the sublattice phase. This results in the probability distributions for the order parameter and density having multiple peaks. The probability distribution for $|\mathbf{Q^B}|$ and the density ρ^B are shown in Figs. 5.5(e) and (f) respectively for values of μ_B near the transition point. The plots shows two clear peaks for $\mu_B \approx 1.75$, one corresponding to the disordered phase and the other to the sublattice phase, consistent with a first order transition. The two dimensional color plot of the probability distribution of the complex order parameter $\mathbf{Q^B}$ near the critical point is shown in Fig. 5.6, and is consistent with the above observation.

To further establish the first order nature of the transition, we show coexistence of the disordered phase and sublattice phase at the transition point. To do so, we do simula-

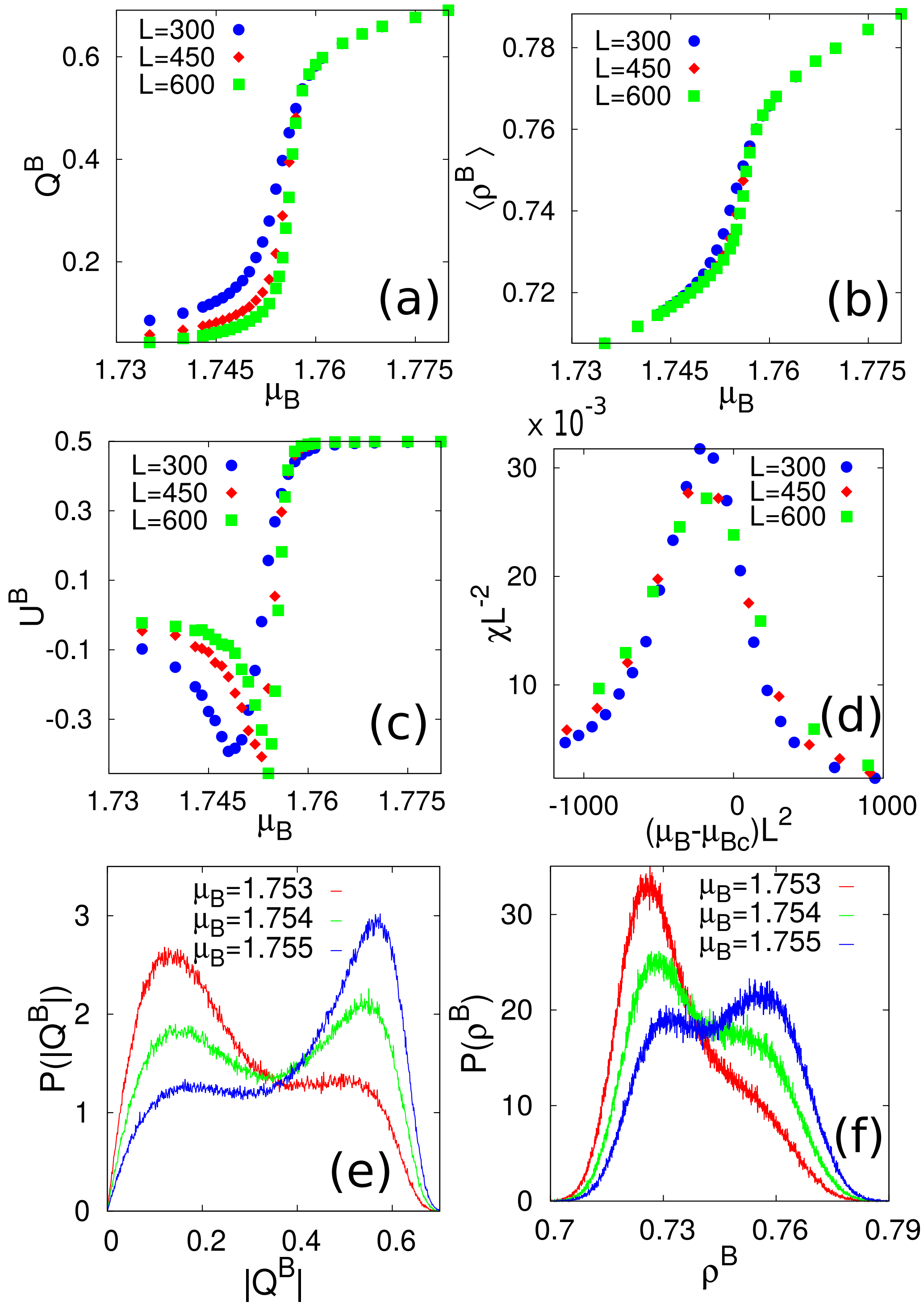

Figure 5.5: Plot of (a) order parameter Q^B, (b) total density ρ^B, (c) Binder cumulant U^B and (d) χL^{-2}, as a function of chemical potential μ_B for three different system sizes $L = 300$ (blue), 450 (red), 600 (green). Plot of probability density function (e) $P(|\mathbf{Q^B}|)$, (f) $P(\rho^B)$ for $\mu_B = 1.753, 1.754, 1.755$ with system size $L = 300$.

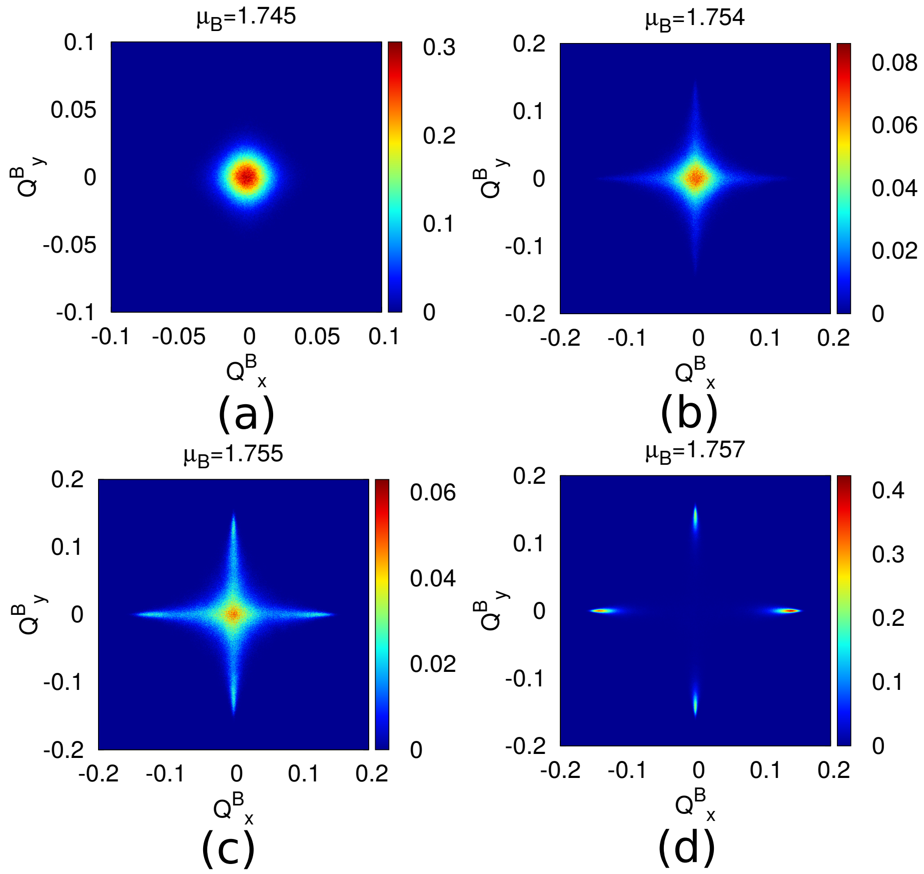

Figure 5.6: Two dimensional density plots of $P(\mathbf{Q^B})$ for different values of μ_B near the transition: (a) $\mu_B = 1.745$, (b) $\mu_B = 1.754$, (c) $\mu_B = 1.755$, and (d) $\mu_B = 1.757$. The data are for a system of size $L = 600$.

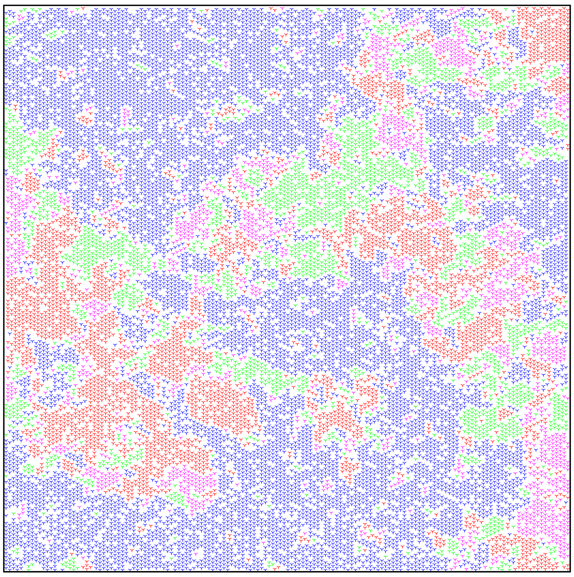

Figure 5.7: Snapshot of a typical equilibrated configuration of the system obtained from *canonical* Monte Carlo simulations with one type of particle having fixed density $\rho^B = 0.740$. The particles on the four sublattices 1, 2, 3 and 4 are represented by green, red, blue and magenta respectively. The snapshot shows the co-existence of the sublattice and disordered phases. The data are for a system of size $L = 300$.

tions in the canonical ensemble, conserving density, of a system having density that lies between the density of disordered system just below the transition and the density of the sublattice phase just above the transition. We choose $\rho^B = 0.74$, which lies between the two maxima of the probability distribution for density as shown in Fig. 5.5(f). The system is evolved in time through an algorithm that conserves the density of the system. A lattice site is chosen at random. If it is occupied by the head of a particle, the particle is removed and deposited at another randomly chosen lattice site. If the deposition does not violate the hard core constraint, the move is accepted, else the particle is placed at its original position. The algorithm obeys detailed balance as each move is reversible and occurs at the same rate. The snapshot of a typical equilibrated configuration of the system is shown in Fig. 5.7. There are regions where the colour is uniform (blue), showing a sublattice phase, while there are other regions where all four colours appears, corresponding to a disordered phase. We conclude that there is phase segregation and coexistence, both signatures of a first order transition.

5.4 Two types of Particles ($z_A = z_B$)

Now consider the case where both types of particles are present with equal activity $z_A = z_B = z$. It is natural to expect that the fully packed phase has a sublattice order where the heads of particles occupy only one sublattice. We first argue that at densities close to full packing, sublattice order is not stable due to the presence of vacancies, and the system prefers a columnar order with densities of both types of particles being roughly equal. We illustrate this instability through an example.

Consider a fully packed configuration with sublattice order. Such a configuration can have only one type of particle (say B-type). Removal of a single particle creates single vacancy made of four empty sites as shown by the filled circles in Fig. 5.8(a). These empty sites may be split into two unbound pairs of half-vacancies by sliding a number of consecutive particles adjacent to the empty sites and flipping their type to A, each of these configurations having the same weight. An example of two particles being slid is shown in Fig. 5.8(b). Introducing more vacancies results in destabilizing the sublattice phase. Sliding results in restoring translational invariance along two of the three directions. However, translational order is still present in the third direction. We will refer to this phase as the columnar phase. We note that in this phase, two sublattices are preferentially occupied, one with A-type particles and the other with B-type particles. The stabilization of the columnar phase by creating vacancies is an example of order by disorder, prototypical example being the hard square gas [1, 60, 63, 2, 7, 64].

If additional attractive interactions are present between neighbouring arms, then the above argument may also be extended to account for the energy cost of creating vacancies. It may then be shown that even for this case, that at high densities, the columnar phase is preferred over the sublattice phase, at all finite temperatures. To preserve continuity of presentation, we postpone the description of the generalized argument to Sec. 5.5.

We now give numerical evidence for the high density phase being columnar and also de-

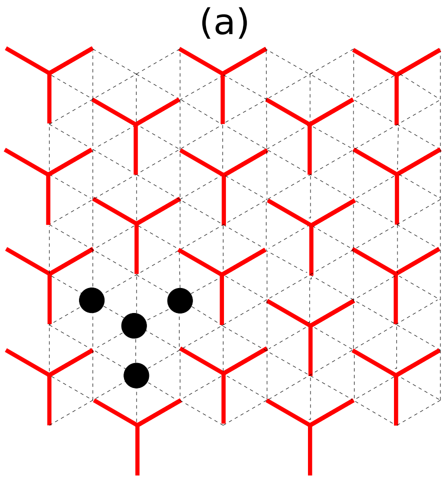

Figure 5.8: (a) Schematic diagram showing the creation of a vacancy consisting of four empty sites (black solid circles), when a particle is removed from the fully packed sublattice phase. (b) The vacancy may be split into two half-vacancies, and separated along a row by sliding particles along the row and changing the type.

termine numerically the different phases of the system at densities away from full packing. Snapshots of equilibrated configurations of the system for different values of μ are shown in Fig. 5.9. Here, the lattice sites are colored using eight colors depending on the type of the particle (2 types) and the sublattice (4 sublattices) that the head belongs to. For small values of μ, the snapshot contains all eight colours distributed uniformly [see Fig. 5.9(a)], corresponding to the disordered phase. For intermediate values of μ, the snapshot shown in Fig. 5.9(b) is predominantly of one color. This phase corresponds to a sublattice phase. The sublattice phase breaks the A-B symmetry and one type of particle is preferred over the other. Finally, for larger values of μ, the snapshot shown in Fig. 5.9(c) has mostly two colors that appear in strips. This phase corresponds to the columnar phase. This is in agreement with our argument presented above that the phase close to full packing is columnar due to the sublattice phase being unstable due to a sliding instability. We thus identify two phase transitions, the critical values of μ being denoted as μ^{DS} and μ^{SC}.

The sublattice phase has an 8 fold degeneracy. To quantify it, consider the vector $\mathbf{Q}_s$:

$$\mathbf{Q}_s = |\mathbf{Q}^A| - |\mathbf{Q}^B|, \tag{5.8}$$

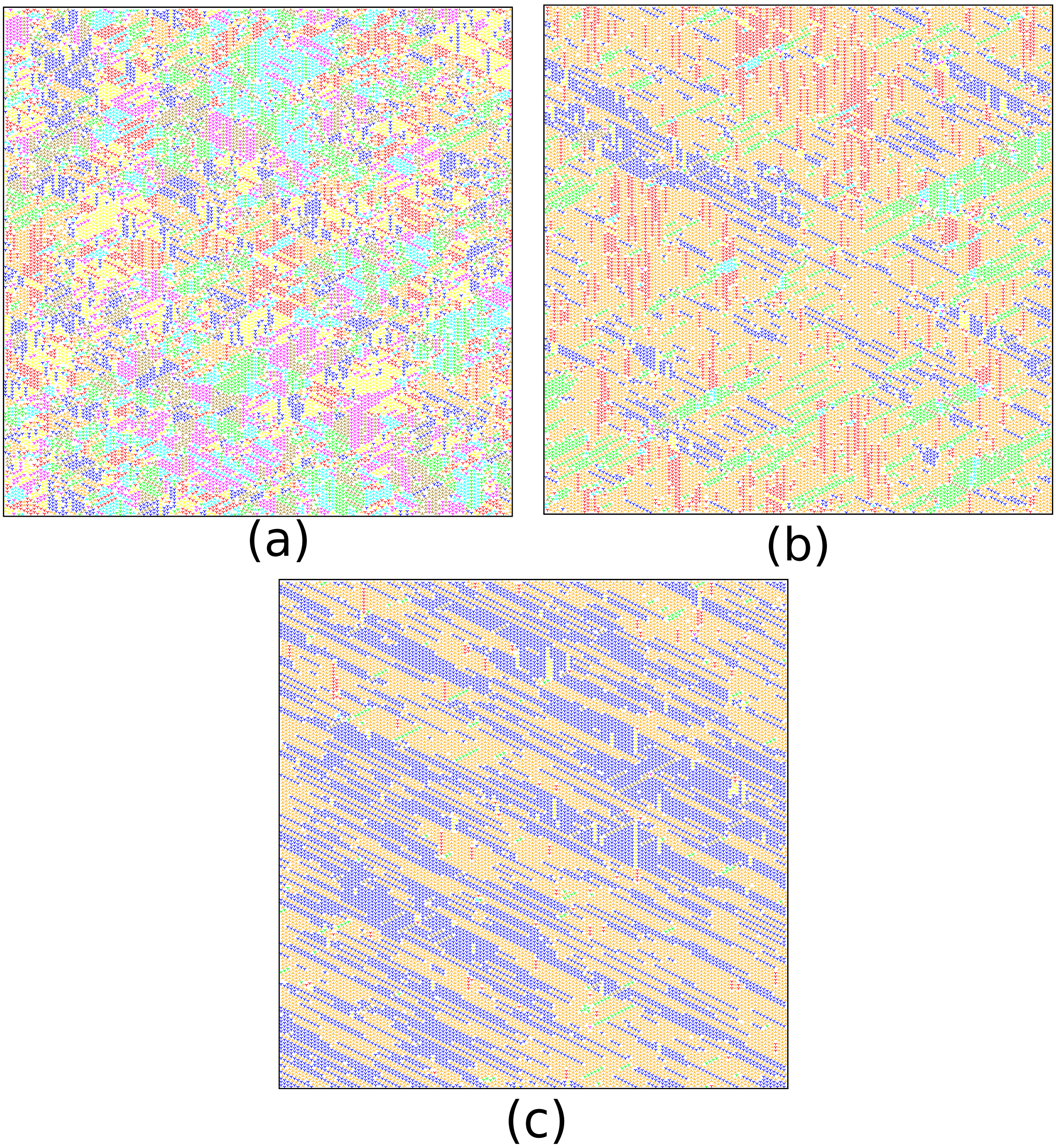

Figure 5.9: Snapshots of equilibrated configurations of the system with two types of particles obtained from *grand canonical* Monte Carlo simulations for different values of μ: (a) disordered phase with $\mu = 4.5$ ($\rho \approx 0.88$), (b) sublattice phase with $\mu = 5.4$ ($\rho \approx 0.947$), and (c) columnar phase with $\mu = 6.0$ ($\rho \approx 0.967$). The particles on the four sublattices 1, 2, 3 and 4 are represented by yellow, olive, cyan and orange for type A and by green, red, blue and magenta for type B. The data are for a system of size $L = 300$.

where $\mathbf{Q}^B$ is given in Eq.(5.4) and $\mathbf{Q}^A$ has a similar definition with ρ_n^B replaced by ρ_n^A. We define the sublattice order parameter Q_s to be

$$Q_s = \langle |\mathbf{Q}_s| \rangle. \tag{5.9}$$

Q_s is zero in the disordered phase and non-zero in the sublattice phase. It is also straightforward to check that $Q_s \approx 0$ in the columnar phase. We characterize the fluctuations of Q_s through the susceptibility χ_s defined as

$$\chi_s = L^2(\langle |\mathbf{Q_s}|^2 \rangle - Q_s^2). \tag{5.10}$$

We also define the Binder cumulant associated with Q_s as U_s:

$$U_s = 1 - \frac{\langle |\mathbf{Q}_s|^4 \rangle}{2\langle |\mathbf{Q}_s|^2 \rangle^2}. \tag{5.11}$$

To characterize the symmetry breaking between the two types of the particles in the disordered phase, we introduce an order parameter ρ_d defined as

$$\rho_d = \langle |\rho^A - \rho^B| \rangle, \tag{5.12}$$

where ρ^A and ρ^B are the fraction of sites occupied by A and B-type particles respectively. We denote the associated susceptibility as χ_d and Binder cumulant as U_d:

$$\begin{aligned} \chi_d &= L^2\left[\langle (\rho^A - \rho^B)^2 \rangle - \rho_d^2\right], && (5.13) \\ U_d &= 1 - \frac{\langle |\rho^A - \rho^B|^4 \rangle}{2\langle |\rho^A - \rho^B|^2 \rangle^2}. && (5.14) \end{aligned}$$

The variation of the order parameters Q_s and ρ_d with μ is shown in Fig. 5.10(a) and (b) respectively. They increase from close to zero to a nonzero value, showing the presence

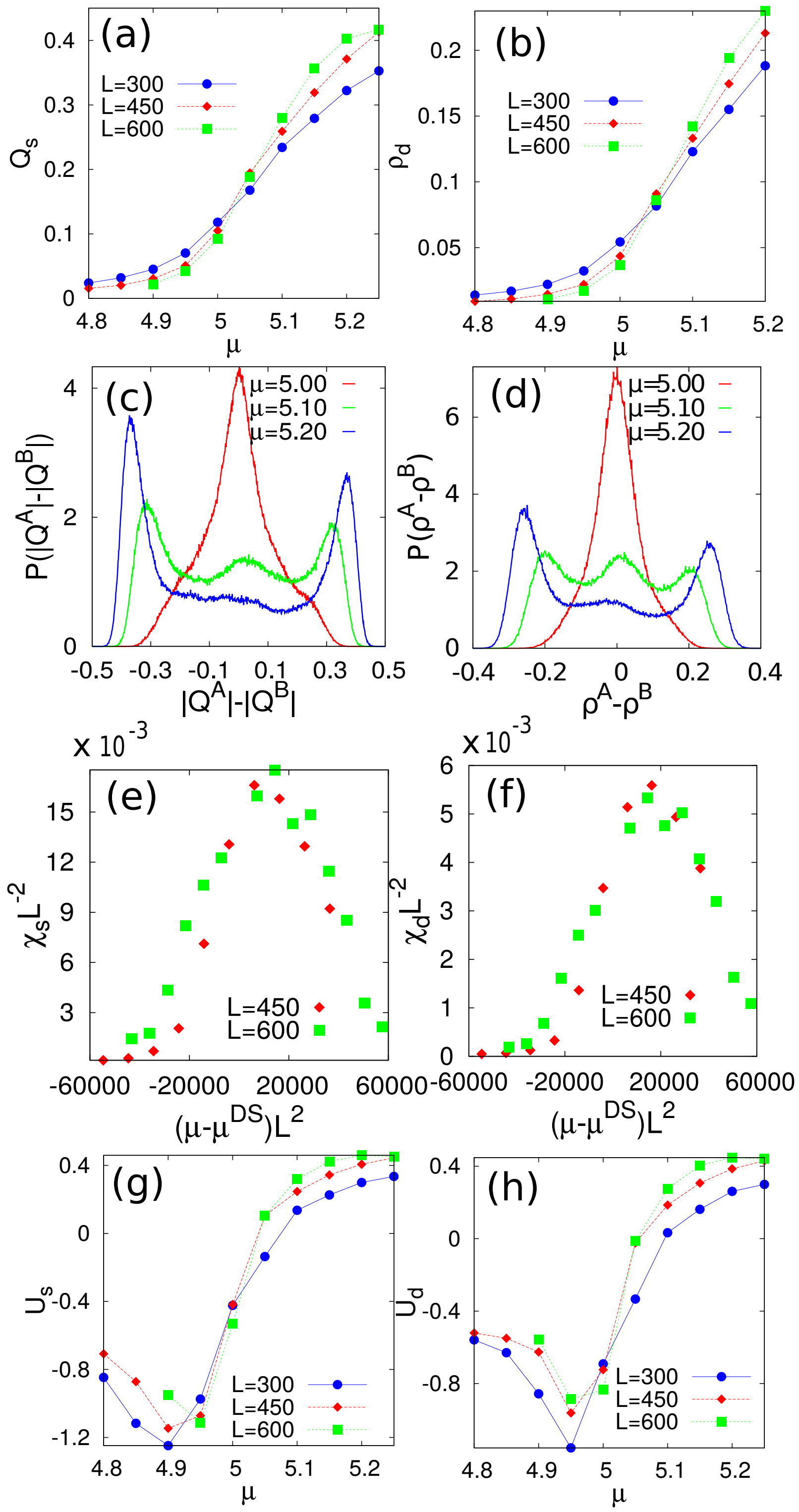

Figure 5.10: Plot of (a) sublattice order parameter Q_s and (b) density difference ρ_d as a function of μ. Plot of probability distribution: (c) $P(|Q^A| - |Q^B|)$ and (d) $P(\rho^A - \rho^B)$ near disorder to sublattice transition for the system of size $L = 300$. Plot of rescaled susceptibilities: (e) $\chi_s L^{-2}$ and (f) $\chi_d L^{-2}$ associated with Q_s and ρ_d respectively about the critical point μ^{DS}. Plots are for the systems of size $L = 300, 450$ and 600.

of the sublattice phase. The curves for different system sizes cross close to $\mu \approx 5.07$, and density $\rho \approx 0.930$. While a clear discontinuity in the order parameters is not discernable from Fig. 5.10(a) and (b), we now present evidence for the transition being first order in nature. The probability distributions for $(|Q^A| - |Q^B|)$ and $(\rho^A - \rho^B)$ near the transition point are shown in Fig. 5.10(c) and (d) respectively. As μ is increased, the probability distributions change from being single peaked, corresponding to the disordered phase, to a three-peaked distribution, corresponding to coexistence of the sublattice and disordered phase, to a symmetric double-peaked distribution, corresponding to the sublattice phase. Coexistence close to the transition is a clear signature of the first order nature of the transition. We note that the distributions sharpen with increasing system size. The variation of Binder cumulant U_s and U_d with μ is shown in Fig. 5.10(g) and (h) respectively. It becomes negative for certain values of μ, which is a clear signature of first order transition. In a first order transition, the susceptibilities scale as

$$\chi \sim L^2 f[(\mu - \mu_c)L^2]. \tag{5.15}$$

When scaled as described with $\mu^{DS} \approx 5.07$, $\rho^{DS} \approx 0.930$, the data for different system sizes collapse onto a single curve, as shown in Fig. 5.10(e) and (f). We conclude that the disordered to sublattice transition is first order in nature.

In the columnar phase, two sublattices are preferentially occupied by the particles. This selection can be done in six different ways and each way has two possibilities of filling, as A-type and B-type particles can choose either one of the selected two sublattices. Thus, the columnar phase has a 12 fold degeneracy. To quantify this phase illustrated in Fig. 5.9(c), we define a columnar order parameter Q_c as follows. In the columnar phase, the particles occupy alternate rows along one of the three orientations, and occupy all rows in the other two orientations. The breaking of the translational invariance in a direction is reflected in the difference in density of heads between even and odd rows and is captured by

$$\begin{aligned}
Q_1 &= |\rho_1 + \rho_2 - \rho_3 - \rho_4|, \\
Q_2 &= |\rho_1 + \rho_3 - \rho_2 - \rho_4|, \\
Q_3 &= |\rho_1 + \rho_4 - \rho_3 - \rho_2|,
\end{aligned} \tag{5.16}$$

where ρ_i is the fraction of sites belonging to sublattice i that is occupied by a particle, irrespective of the type. In Q_1, $(\rho_1 + \rho_2)$ measures the density of occupied sites in odd horizontal rows [see Fig. 5.1(b)] and $(\rho_3 + \rho_4)$ the density of occupied sites in even horizontal rows. Thus, Q_1 is non-zero only when there is translational order along the horizontal rows, and similar interpretations hold for Q_2 and Q_3. Now, consider the vector

$$\mathbf{Q}_c = |\mathbf{Q}_c| e^{i\theta_c} = Q_1 + Q_2 e^{2\pi i/3} + Q_3 e^{4\pi i/3}. \tag{5.17}$$

We define the columnar order parameter to be

$$Q_c = \langle |\mathbf{Q}_c| \rangle. \tag{5.18}$$

In the columnar phase, Q_c is non-zero. In the disordered phase $Q_c \approx 0$, as each of the Q_i in Eq. (5.16) is approximately zero. In the sublattice phase, one sublattice is preferentially occupied and each of the Q_i in Eq. (5.16) becomes non-zero but approximately equal in magnitude, and hence again $Q_c \approx 0$. Thus, a non-zero Q_c is a signature for the columnar phase. We define the corresponding susceptibility as

$$\chi_c = L^2(\langle |\mathbf{Q}_c|^2 \rangle - Q_c^2). \tag{5.19}$$

In the columnar phase the sublattice order parameter Q_s [see Eq. (5.9)] and the density difference ρ_d [see Eq. (5.12)] both becomes zero. The variation of Q_s and ρ_d with μ is shown

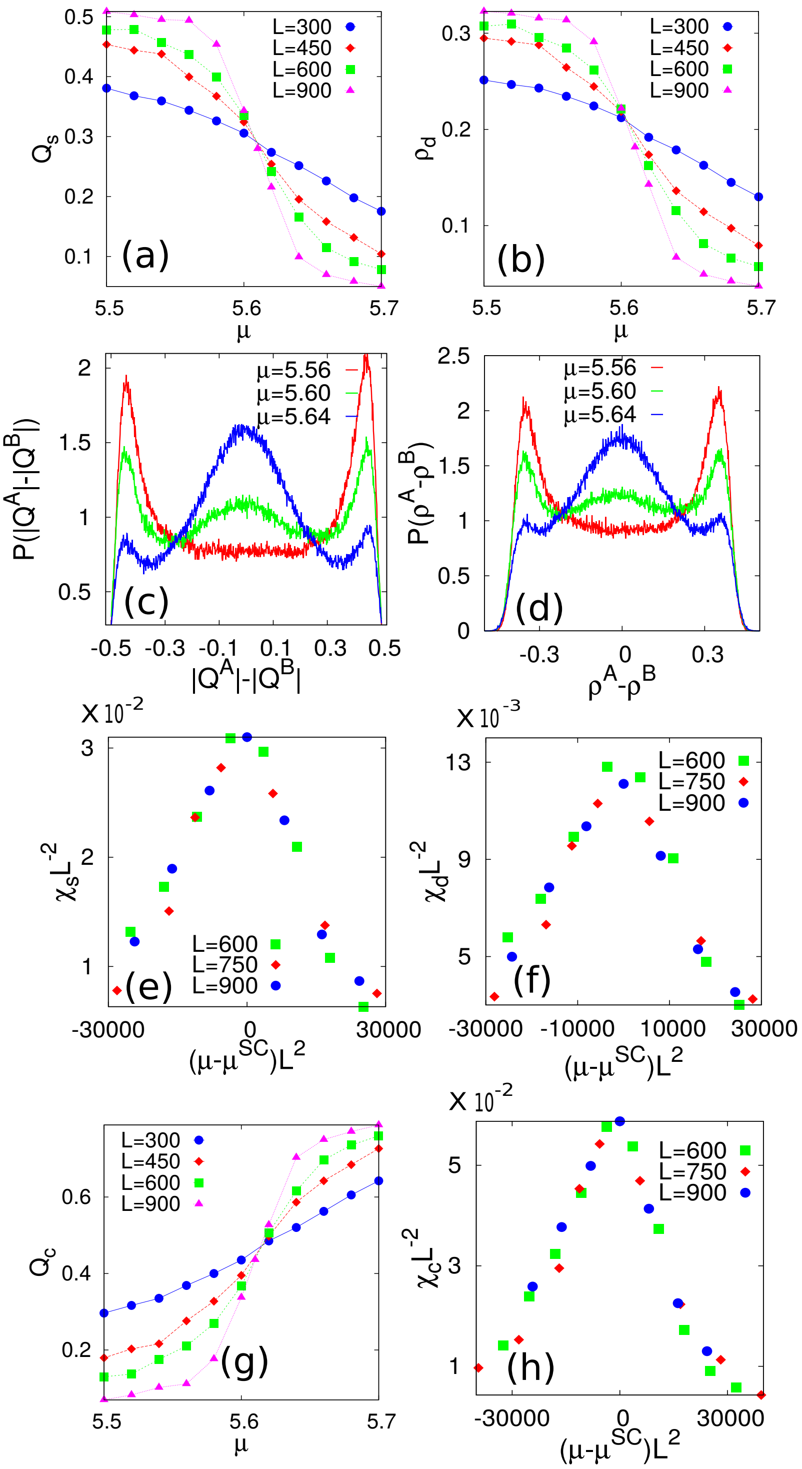

Figure 5.11: Plot of (a) sublattice order parameter Q_s and (b) density difference ρ_d as a function of μ. Plot of probability distribution: (c) $P(|Q^A| - |Q^B|)$ and (d) $P(\rho^A - \rho^B)$ near sublattice to columnar transition for the system size $L = 300$. Plot of rescaled susceptibilities: (e) $\chi_s L^{-2}$ and (f) $\chi_d L^{-2}$ associated with Q_s and ρ_d respectively about the critical point μ^{SC}. Plot of (g) columnar order parameter Q_c and (h) associated rescaled susceptibility $\chi_c L^{-2}$ as a function of μ and $(\mu - \mu^{SC})$ respectively. Plots are for the systems of size varying from $L = 300$ to 900.

in Fig. 5.11(a) and (b) respectively. The probability distributions for Q_s and $(\rho^A - \rho^B)$ near the transition point are shown in Fig. 5.11(c) and (d) respectively. As μ is increased, the probability distributions change from symmetric double-peaked, corresponding to the sublattice phase, to a three-peaked distribution, corresponding to coexistence of the sublattice and columnar phase, to a dominant single-peaked distribution, corresponding to the columnar phase. The coexistence of both columnar phase and sublattice phase is a signature of first order transition. For the first order transition susceptibilities follow the scaling law as described in Eq. (5.15). With this scaling we get the collapse of susceptibilities χ_s and χ_d onto single curve as shown in Fig. 5.11(e) and (f), for critical value of chemical potential $\mu^{SC} \approx 5.61$ with density $\rho^{SC} \approx 0.956$.

The variation of the order parameter Q_c with μ for different system size is shown in Fig. 5.11(g). It acquires nonzero value in the columnar phase. The susceptibility χ_c also obeys the scaling law as described in Eq. (5.15). This is confirmed from the Fig. 5.11(h) in which collapse of curves for different system sizes with described scaling is shown.

5.5 Conclusion

In this paper we studied the different phases and phase transitions of hard Y-shaped particles on a two dimensional triangular lattice. There are two types of Y-shaped particles depending on their orientation on the lattice, which are mirror images of each other. By incorporating cluster moves, we were able to equilibrate the system at densities close to full packing, allowing us to unambiguously determine the phases at all densities. In addition to the low-density disordered phase, we find two other phases. At intermediate phases, the phase has a solid-like sublattice order. In this phase, the symmetry between the two types of particles is broken resulting in a majority of one type of particle. In addition, these particles preferentially occupy one of the four sublattices of the lattice. At high densities, the phase has columnar order. In this phase, the symmetry between the two types of particles is restored. However, there is translational order in one of the three directions, wherein particles preferentially occupy either even or odd rows. The first transition from disordered to sublattice phase occurs at $\mu^{DS} \approx 5.07$ and the second transition from sublattice to columnar phase occurs at $\mu^{SC} \approx 5.61$. Both the transitions are first order in nature. Y-shaped particles give a simple example of a system where small number of vacancies destabilize the sublattice phase into a columnar phase while a larger number of vacancies again stabilizes the sublattice phase. When only one type of particle is present, the model undergoes a single first order phase transition from a low density disordered phase to high density sublattice phase, and occurs at $\mu_{Bc} \approx 1.756$.

The high density phase that we observe in this paper has columnar order with both types of particles equally present, which is in contradiction to the results obtained from Monte Carlo simulations of Y-shaped particles with attractive interactions in Refs. [16, 15], wherein it was shown that the high density phase has sublattice order in which only one kind of particle is present. For only excluded volume interactions, we argued in Sec. 5.4 that the introduction of vacancies results in the destabilization of the sublattice phase into a columnar phase, because the vacancies split into two unbound half-vacancies that can be separated away from each other resulting in a gain in entropy. We now argue that this instability is present even in the presence of attractive interaction between the nearest-neighbour arms of different particles. Consider the case when vacancy is created by removing a single particle from a sublattice phase at full packing, as shown in Fig. 5.12(a). If $-\epsilon$ is the energy of each nearest neighbour pair of arms, then this vacancy costs an energy 12ϵ. On splitting the vacancy into two half-vacancies and sliding them away from each other by one, two, or three particles [see Figs. 5.12(b)–(d)], the energy cost increases to 13ϵ, but *does not* increase with separation between the half-vacancies.

Thus, the partition function Z of the system may be written as

$$\begin{aligned} Z &= 4z^{N/4}e^{3N\beta\epsilon/2}\left[1+\frac{Ne^{-12\beta\epsilon}}{4z}\right.\\ &\left. +\frac{3N(\frac{L}{2}-1)e^{-13\beta\epsilon}}{8z}+O(z^{-2})\right], \end{aligned} \tag{5.20}$$

where $\beta = (kT)^{-1}$ is the inverse temperature. The free energy $\beta f = -\ln Z$ is then

$$\beta f = \frac{-\ln z}{4} - \frac{3\beta\epsilon}{2} - \frac{e^{-12\beta\epsilon}}{4z} - \frac{3Le^{-13\beta\epsilon}}{16z} + O(z^{-2}). \tag{5.21}$$

Clearly, the first order correction term proportional to z^{-1} diverges with system size, as is indicative of systems with columnar order. If the divergent terms are resummed correctly, taking into account the columnar nature of the phase, then the first correction term becomes $O(z^{-1/2})$ [2, 115]. The term of order z^{-1} being divergent implies that the expansion about the sublattice phase is not convergent and, thus, we conclude that the high density phase is columnar even when interactions are present. We note that in Ref. [15], attractive interactions were included for neighbouring central sites too. However, it may be easily checked that the above expansion is true for this case also, albeit with a energy cost of 2ϵ for half-vacancy when compared to bound vacancy. From Eq. (5.21), it may also be seen that for temperatures less than or order of $\epsilon/\ln L$, it would be possible to see a sublattice phase, but this is purely a finite-size effect.

In addition, it was argued in Refs. [16, 15] that, for the model with attractive interactions and hard core constraints, there is no phase transition above a critical temperature. In the limit of infinite temperature, the attractive interactions play no role, and the model reduces to a problem with only hard core interactions between the particles, which is the model studied in the current paper. For the latter model, we established the presence of two density driven phase transitions, in contradiction to the results implied in Refs. [16, 15]. Re-analysing the model with interactions to make the results consistent with those in the current paper is a promising area for future study. Another area for future study is the

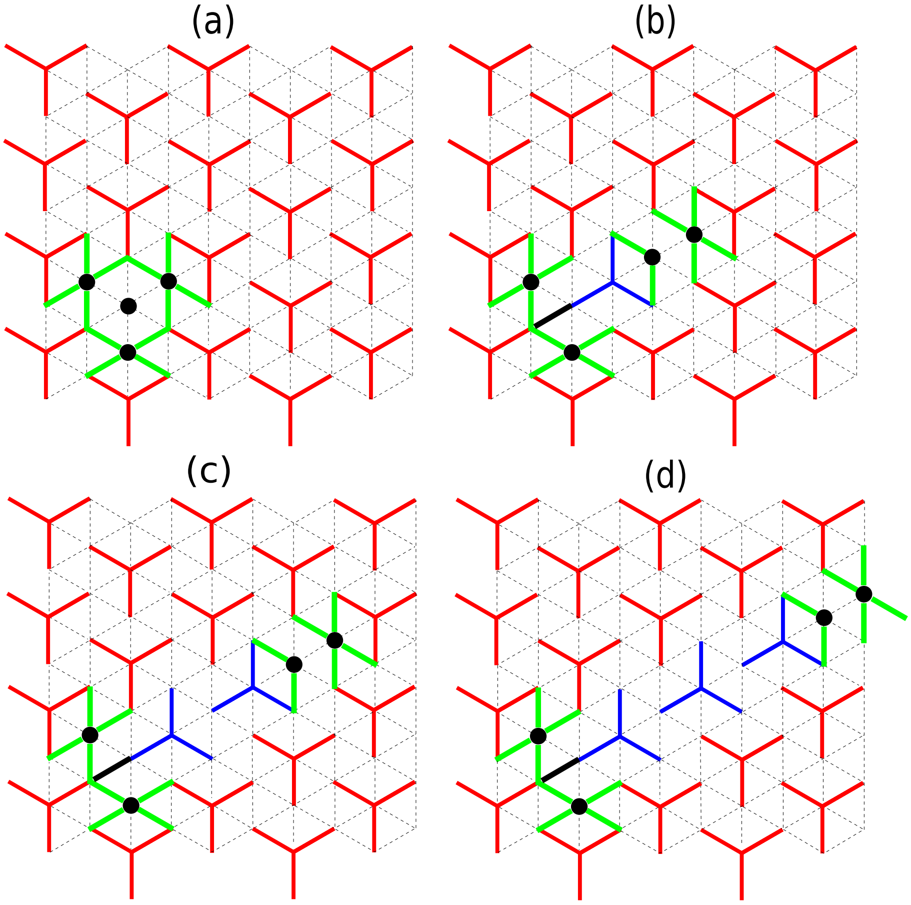

Figure 5.12: Schematic diagrams to calculate, in a fully packed sublattice phase of B-type particles, the energy cost to create: (a) a vacancy consisting of four empty sites (black solid circle) vacancy), (b) two half-vacancies separated by one A-type particle, (c) two half-vacancies separated by two A-type particles, and (d) two half-vacancies separating three A-type particles. Compared to the background sublattice phase, green bonds increase the energy by ϵ while black bonds decrease the energy by ϵ. The energy cost is 12ϵ for (a), and 13ϵ for (b)-(d).

system of Y-shaped particles with larger arm lengths which could be symmetric [15]. For these systems with only excluded volume interaction, we expect the high density phase to be columnar [15].

It is tempting to analyse the high density columnar phase using high density expansions as developed for squares and rectangles [1, 60, 63, 2, 7, 64, 8, 69]. These expansions are in terms of number defects (which could be extended). However the columnar phase of Y-shaped particles is different from that of these simpler models, in which the type of particles occupy preferred sublattices in the columnar phase. This makes it difficult to even write the zeroth order term for the partition function corresponding to no defects.

One may also consider kinds of lattices like the honeycomb lattice. The honeycomb lattice (see Fig. 5.13) is different from the triangular lattice in that the site decides what type of Y-molecule may be placed on it. We argue that the nature of the high density phase is different on the honeycomb lattice as compared to the triangular lattice. Consider a fully packed phase, as shown in Fig. 5.13(a), in which translational order is broken, and the system is in a solid-like phase. Four vacancies may be created by removing one particle from site S_1 as shown in Fig. 5.13(b). The four vacant sites that are created remain bound to each other, and the solid-like order is stable. To next order in perturbation, consider creating eight vacant sites by removing two adjacent particles as shown in Fig. 5.13(c). These eight vacancies may be split into two sets and moved arbitrarily far from each other by sliding particles along the direction shown by dotted lines in Fig. 5.13(c). This instability will lead to the phase becoming columnar (as argued by the high density expansion for the triangular lattice). Thus, we have the following interesting scenario. As density is decreased from one, the system will first undergo a transition from a solid-like phase to a columnar phase. Further decrease in density may result in a transition to a solid-like phase as in the triangular lattice followed by a disorder phase, or directly into a disordered phase. It would be interesting to verify these conjectures in Monte Carlo simulations.

HCLGs sometimes show multiple phase transitions with increasing density, but only when

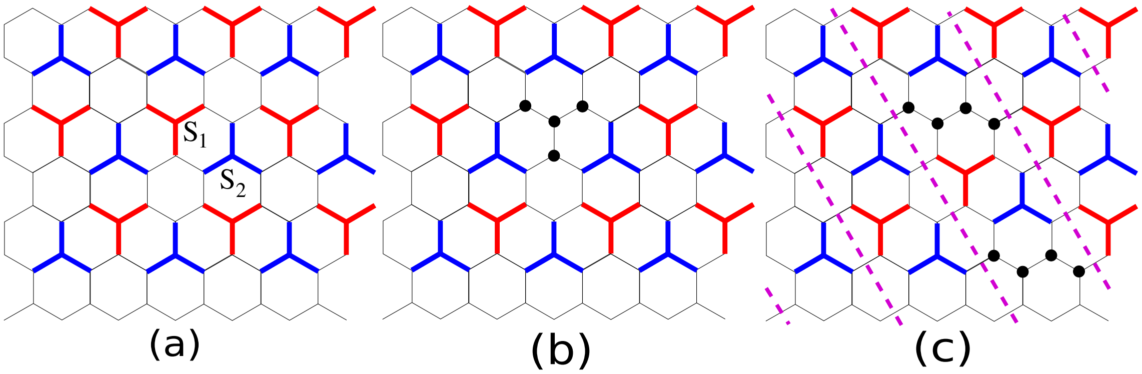

Figure 5.13: Schematic diagrams of configurations on a honeycomb lattice when: (a) no vacancy is present (full packing), (b) four bound vacancies are created by removing a particle from the site labelled S_1, and (c) eight unbounded vacancies are created by removing two particles from the sites labeled S_1 and S_2 followed by sliding particles in the directions shown by the dotted magenta lines. Black dots represent empty sites.

the excluded volume per particle is large. For instance, for multiple phase transitions to be present, the minimum range of interaction is seventh nearest neighbour for rods [71, 14], fifth nearest neighbour for rectangles [72, 73], fourth nearest neighbour for HCLG models for discs [77, 115] while nearest neighbour exclusion models like the 1-NN model on the square lattice [1, 116, 117, 3, 118, 119, 120, 121, 122, 63, 123, 124, 125, 126, 127, 128, 129, 130, 131, 132] or the hard hexagon model on the triangular lattice [61] show only one transition from a disordered phase to a sublattice phase. The excluded volume of Y-shaped particles consists of nearest neighbour sites, as in the hard hexagon model and half of the next-nearest neighbour sites depending on the pair of particles being considered. It is quite surprising that despite the short ranged nature of the interaction, the system undergoes two density-driven phase transitions. It is possible that this feature may also be extended to mixtures on a square lattice. From the insights gained from the current paper, we expect that if there are two kinds of particles A and B on a square lattice, where the A-A and B-B excluded volume interactions are upto second nearest neighbour, but the A-B excluded volume interaction is upto the third nearest neighbour, then the high density phase will be columnar and there will be multiple transitions. Confirming this conjecture in simulations would be interesting.

Chapter 6

Conclusions

In this thesis we have studied, in detail, the phase diagram of system of particles having different geometrical shapes both in two and three dimensions. The particles sit on lattice sites and interact only through excluded volume interaction, i.e., no two particles may overlap. The HCLG models that we have studied include: (1) hard 2×2 squares on square lattice, (2) mixture of hard 2×2 squares, horizontal and vertical dimers on square lattice, (3) hard $2 \times 2 \times 1$ hard plates on cubic lattice and (4) hard Y-shaped particles on triangular lattice.

In Chapter 1, we have given a brief introduction and previous studies of HCLG models.

In Chapter 2, we have estimated the critical activity for hard square model with pairwise approximation by calculating the interfacial tension between two differently ordered columnar phase and equating it to zero. In this calculation, we have considered the presence of multiple defect particles in both ordered phase and overhangs of height two in the interface. We have estimated the critical activity $z_c = 105.35$, which is in good agreement with existing Monte Carlo simulation results, and is a significant improvement over earlier best estimates of $z_c = 54.87$ and $z_c = 135.63$. The calculation of interfacial tension in the presence of overhangs of height greater than two may be the future extension of current work. It would be interesting to perform the interfacial tension calculation in antiferromagnetic Ising model [6] in the presence of overhangs and defects.

In Chapter 3, we have estimated the phase boundary separating the disordered phase and columnar ordered phase by calculating the interfacial tension between two columnar ordered phase in the mixture of hard squares and dimers. We have calculated the interfacial tension for two different cases. In first case, we have ignored the presence of overhangs in the interface. In secondly case, we have considered the presence of overhangs of height two in the interface. Both estimates show reasonable agreement with the Monte Carlo results. In both calculations, we assumed that the ordered phases are perfectly columnar, i.e., no defect particles are present. The calculation could be improved by considering the presence of single defect or multiple defect at both sides of the interface. Another promising area of future research is the mixture of 3×3 squares and trimers (both horizontal and vertical).

In Chapter 4, we have studied the phase diagram for the system of hard $2 \times 2 \times 1$ plates in cubic lattice. Three types of plates are possible x-plate, y-plate and z-plate, having normals along three principal directions of the cubic lattice. Using transfer matrix based Monte Carlo simulations we have shown that the system undergoes two entropy driven phase transitions with increasing density. These are disordered phase to layered phase and layered phase to sublattice phase. Using finite size scaling we have demonstrated that disordered–layered transition is continuous with the universality class of three dimensional Heisenberg model with cubic anisotropy, while layered–sublattice transition in discontinuous in nature. System of $k \times k \times 1$ plates with $k > 2$ is an interesting area for pursuing future research. Another interesting area could be the system of interacting hard plates in cubic lattice.

In Chapter 5, we have studied system of hard Y-shaped particles on triangular lattice. Two types of particles are possible which are mirror images of each other. Using large scale Monte Carlo simulation, we have shown that the system undergoes two phase transitions with increasing particle density. At low density the system is disordered. With increasing density the system goes to sublattice phase by breaking translational symmetry in all three directions. At very high density the equilibrium phase is columnar ordered. Using finite size scaling, we have shown that both transitions are discontinuous in nature. In real system along with the excluded volume effect, other effects, e.g., coulomb interaction, spin interaction, etc. are present. The study of Y-shaped particles in the presence of interaction is an open area for future study.

Bibliography

[1] A. Bellemans and R. K. Nigam, “Phase transitions in two dimensional lattice gases of hard square molecules,” *J. Chem. Phy.*, vol. 46, no. 8, pp. 2922–2935, 1967.

[2] K. Ramola and D. Dhar, “High-activity perturbation expansion for the hard square lattice gas,” *Phys. Rev. E*, vol. 86, p. 031135, Sep 2012.

[3] H. C. M. Fernandes, J. J. Arenzon, and Y. Levin, “Monte carlo simulations of two-dimensional hard core lattice gases,” *J. Chem. Phys.*, vol. 126, no. 11, p. 114508, 2007.

[4] L. Lafuente and J. A. Cuesta, “Phase behavior of hard-core lattice gases: A fundamental measure approach,” *The Journal of Chemical Physics*, vol. 119, no. 20, pp. 10832–10843, 2003.

[5] L. Lafuente and J. A. Cuesta, “Fundamental measure theory for lattice fluids with hard-core interactions,” *Journal of Physics: Condensed Matter*, vol. 14, no. 46, p. 12079, 2002.

[6] P. A. Slotte, “Phase diagram of the square-lattice ising model with first- and second-neighbour interactions,” *Journal of Physics C: Solid State Physics*, vol. 16, no. 15, p. 2935, 1983.

[7] T. Nath, D. Dhar, and R. Rajesh, “Stability of columnar order in assemblies of hard rectangles or squares,” *Europhys. Lett.*, vol. 114, no. 1, p. 10003, 2016.

[8] K. Ramola, K. Damle, and D. Dhar, "Columnar order and ashkin-teller criticality in mixtures of hard squares and dimers," *Phys. Rev. Lett.*, vol. 114, p. 190601, May 2015.

[9] X. Feng, H. W. J. Blöte, and B. Nienhuis, "Lattice gas with nearest- and next-to-nearest-neighbor exclusion," *Phys. Rev. E*, vol. 83, p. 061153, Jun 2011.

[10] M. E. Zhitomirsky and H. Tsunetsugu, "Lattice gas description of pyrochlore and checkerboard antiferromagnets in a strong magnetic field," *Phys. Rev. B*, vol. 75, p. 224416, Jun 2007.

[11] H. C. Marques Fernandes, Y. Levin, and J. J. Arenzon, "Equation of state for hard-square lattice gases," *Phys. Rev. E*, vol. 75, p. 052101, May 2007.

[12] H. N. V. Temperley, "Improvements in the lattice model of a liquid," *Proceedings of the Physical Society*, vol. 77, no. 3, p. 630, 1961.

[13] A. Gschwind, M. Klopotek, Y. Ai, and M. Oettel, "Isotropic-nematic transition for hard rods on a three-dimensional cubic lattice," *Phys. Rev. E*, vol. 96, p. 012104, Jul 2017.

[14] N. Vigneshwar, D. Dhar, and R. Rajesh, "Different phases of a system of hard rods on three dimensional cubic lattice," *J. Stat. Mech.*, vol. 2017, p. 113304, nov 2017.

[15] P. Szabelski, W. Rzysko, T. Panczyk, E. Ghijsens, K. Tahara, Y. Tobe, and S. De Feyter, "Self-assembly of molecular tripods in two dimensions: structure and thermodynamics from computer simulations," *RSC Adv.*, vol. 3, pp. 25159–25165, 2013.

[16] D. Ruth, R. Toral, D. Holz, J. Rickman, and J. Gunton, "Impact of surface interactions on the phase behavior of y-shaped molecules," *Thin Solid Films*, vol. 597, pp. 188 – 192, 2015.

[17] P. N. Pusey and W. van Megen, "Phase behaviour of concentrated suspensions of nearly hard colloidal spheres," *Nature*, vol. 320, no. 16, pp. 340–342, 1986.

[18] K. Zhao, R. Bruinsma, and T. G. Mason, "Entropic crystal-crystal transitions of brownian squares," *Proc. Natl. Acad. Sci.*, vol. 108, no. 7, pp. 2684–2687, 2011.

[19] X. Wen, R. B. Meyer, and D. L. D. Caspar, "Observation of smectic-a ordering in a solution of rigid-rod-like particles," *Phys. Rev. Lett.*, vol. 63, pp. 2760–2763, Dec 1989.

[20] Z. Dogic and S. Fraden, "Cholesteric phase in virus suspensions," *Langmuir*, vol. 16, no. 20, pp. 7820–7824, 2000.

[21] A. Kuijk, A. van Blaaderen, and A. Imhof, "Synthesis of monodisperse, rodlike silica colloids with tunable aspect ratio," *Journal of the American Chemical Society*, vol. 133, no. 8, pp. 2346–2349, 2011.

[22] M. P. B. van Bruggen, F. M. van der Kooij, and H. N. W. Lekkerkerker, "Liquid crystal phase transitions in dispersions of rod-like colloidal particles," *J. Phys. Condensed Matter*, vol. 8, no. 47, p. 9451, 1996.

[23] Y. Maeda, T. Niori, J. Yamamoto, and H. Yokoyama, "Phase behavior of banana-shaped molecules under pressure," *Thermochimica Acta*, vol. 431, no. 12, pp. 87 – 93, 2005. A collection of papers from the 40th Anniversary Japanese Conference on Calorimetry and Thermal Analysis held in Tokyo, Japan, October 12 - 14, 2004.

[24] D. E. Taylor, E. D. Williams, R. L. Park, N. C. Bartelt, and T. L. Einstein, "Two-dimensional ordering of chlorine on ag(100)," *Phys. Rev. B*, vol. 32, pp. 4653–4659, Oct 1985.

[25] P. Bak, P. Kleban, W. N. Unertl, J. Ochab, G. Akinci, N. C. Bartelt, and T. L. Einstein, "Phase diagram of selenium adsorbed on the ni(100) surface: A physical

realization of the ashkin-teller model," *Phys. Rev. Lett.*, vol. 54, pp. 1539–1542, Apr 1985.

[26] L. Onsager, "The effects of shape on the interaction of colloidal particles," *Annals of the New York Academy of Sciences*, vol. 51, no. 4, pp. 627–659, 1949.

[27] W. G. Hoover and F. H. Ree, "Melting transition and communal entropy for hard spheres," *J. Chem. Phys.*, vol. 49, no. 8, pp. 3609–3617, 1968.

[28] P. Bolhuis and D. Frenkel, "Tracing the phase boundaries of hard spherocylinders," *J. Chem. Phys.*, vol. 106, no. 2, pp. 666–687, 1997.

[29] M. A. Bates and D. Frenkel, "Influence of polydispersity on the phase behavior of colloidal liquid crystals: A monte carlo simulation study," *J. Chem. Phys.*, vol. 109, no. 14, pp. 6193–6199, 1998.

[30] C. Avendano and F. A. Escobedo, "Phase behavior of rounded hard-squares," *Soft Matter*, vol. 8, pp. 4675–4681, 2012.

[31] A. van Blaaderen, "Observation of solid-solid transitions in 3d crystals of colloidal superballs," *Nature*, vol. 439, no. 545, 2006.

[32] P. F. Damasceno, M. Engel, and S. C. Glotzer, "Predictive self-assembly of polyhedra into complex structures," *Science*, vol. 337, no. 6093, pp. 453–457, 2012.

[33] J.-M. Meijer, A. Pal, S. Ouhajji, H. N. W. Lekkerkerker, A. P. Philipse, and A. V. Petukhov, "Observation of transitions in 3d crystals of colloidal superballs," *Nature Communications*, vol. 8, no. 14352, 2017.

[34] J. A. Champion, Y. K. Katare, and S. Mitragotri, "Particle shape: A new design parameter for micro- and nanoscale drug delivery carriers," *Journal of Controlled Release*, vol. 121, no. 1, pp. 3 – 9, 2007. Fourth International Nanomedicine and Drug Delivery Symposium.

[35] A. B. Jindal, “The effect of particle shape on cellular interaction and drug delivery applications of micro- and nanoparticles,” *International Journal of Pharmaceutics*, vol. 532, no. 1, pp. 450 – 465, 2017.

[36] Y. A. Vlasov, X.-Z. Bo, J. C. Sturm, and D. J. Norris, “On-chip natural assembly of silicon photonic bandgap crystals,” *Nature*, vol. 414, no. 6861, p. 289, 2001.

[37] J. D. Forster, J.-G. Park, M. Mittal, H. Noh, C. F. Schreck, C. S. O Hern, H. Cao, E. M. Furst, and E. R. Dufresne, “Assembly of optical-scale dumbbells into dense photonic crystals,” *ACS nano*, vol. 5, no. 8, pp. 6695–6700, 2011.

[38] S. Sacanna, M. Korpics, K. Rodriguez, L. Colon-Melendez, S.-H. Kim, D. J. Pine, and G.-R. Yi, “Shaping colloids for self-assembly,” *Nature communications*, vol. 4, p. 1688, 2013.

[39] A. Patrykiejew, S. Skowski, and K. Binder, “Phase transitions in adsorbed layers formed on crystals of square and rectangular surface lattice,” *Surface Science Reports*, vol. 37, no. 6, pp. 207 – 344, 2000.

[40] B. Dunweg, A. Milchev, and P. A. Rikvold, “A model for adsorption of o on mo(110): Phase transitions with nonuniversal behavior,” *The Journal of Chemical Physics*, vol. 94, no. 5, pp. 3958–3973, 1991.

[41] W.-H. Soe, C. Manzano, N. Renaud, P. de Mendoza, A. De Sarkar, F. Ample, M. Hliwa, A. M. Echavarren, N. Chandrasekhar, and C. Joachim, “Manipulating molecular quantum states with classical metal atom inputs: Demonstration of a single molecule nor logic gate,” *ACS Nano*, vol. 5, no. 2, pp. 1436–1440, 2011. PMID: 21291281.

[42] W.-H. Soe, C. Manzano, A. De Sarkar, F. Ample, N. Chandrasekhar, N. Renaud, P. de Mendoza, A. M. Echavarren, M. Hliwa, and C. Joachim, “Demonstration of a nor logic gate using a single molecule and two surface gold atoms to encode the logical input,” *Phys. Rev. B*, vol. 83, p. 155443, Apr 2011.

[43] S. Godlewski, M. Kolmer, H. Kawai, B. Such, R. Zuzak, M. Saeys, P. de Mendoza, A. M. Echavarren, C. Joachim, and M. Szymonski, “Contacting a conjugated molecule with a surface dangling bond dimer on a hydrogenated ge(001) surface allows imaging of the hidden ground electronic state,” *ACS Nano*, vol. 7, no. 11, pp. 10105–10111, 2013. PMID: 24148187.

[44] B. J. Alder and T. E. Wainwright, “Phase transition in elastic disks,” *Phys. Rev.*, vol. 127, pp. 359–361, Jul 1962.

[45] B. J. Alder and T. E. Wainwright, “Phase transition for a hard sphere system,” *J. Chem. Phys.*, vol. 27, no. 5, pp. 1208–1209, 1957.

[46] D. Dhar, “Equivalence of the two-dimensional directed-site animal problem to baxter’s hard-square lattice-gas model,” *Phys. Rev. Lett.*, vol. 49, pp. 959–962, Oct 1982.

[47] D. Dhar, “Exact solution of a directed-site animals-enumeration problem in three dimensions,” *Phys. Rev. Lett.*, vol. 51, pp. 853–856, Sep 1983.

[48] D. C. Brydges and J. Z. Imbrie, “Dimensional reduction formulas for branched polymer correlation functions,” *J. Stat. Phys.*, vol. 110, no. 3, pp. 503–518, 2003.

[49] G. Parisi and N. Sourlas, “Critical behavior of branched polymers and the lee-yang edge singularity,” *Phys. Rev. Lett.*, vol. 46, pp. 871–874, Apr 1981.

[50] D. E. Taylor, E. D. Williams, R. L. Park, N. C. Bartelt, and T. L. Einstein, “Two-dimensional ordering of chlorine on ag(100),” *Phys. Rev. B*, vol. 32, pp. 4653–4659, Oct 1985.

[51] S. Mitchell, G. Brown, and P. Rikvold, “Static and dynamic monte carlo simulations of br electrodeposition on ag(1 0 0),” *Surface Science*, vol. 471, no. 13, pp. 125 – 142, 2001.

[52] M. T. Koper, “A lattice-gas model for halide adsorption on single-crystal electrodes,” *J. Electroanal. Chem.*, vol. 450, no. 2, pp. 189 – 201, 1998.

[53] C. Domb, “Some theoretical aspects of melting,” *Il Nuovo Cimento (1955-1965)*, vol. 9, no. 1, pp. 9–26, 1958.

[54] P. Kasteleyn, “The statistics of dimers on a lattice,” *Physica*, vol. 27, no. 12, pp. 1209 – 1225, 1961.

[55] H. N. V. Temperley and M. E. Fisher, “Dimer problem in statistical mechanics-an exact result,” *Phil. Mag.*, vol. 6, no. 68, pp. 1061–1063, 1961.

[56] M. E. Fisher and J. Stephenson, “Statistical mechanics of dimers on a plane lattice. ii. dimer correlations and monomers,” *Phys. Rev.*, vol. 132, pp. 1411–1431, Nov 1963.

[57] O. J. Heilmann and E. H. Lieb, “Theory of monomer-dimer systems,” *Communications in Mathematical Physics*, vol. 25, no. 3, pp. 190–232, 1972.

[58] D. A. Huse, W. Krauth, R. Moessner, and S. L. Sondhi, “Coulomb and liquid dimer models in three dimensions,” *Phys. Rev. Lett.*, vol. 91, p. 167004, Oct 2003.

[59] C. Gruber and H. Kunz, “General properties of polymer systems,” *Communications in Mathematical Physics*, vol. 22, no. 2, pp. 133–161, 1971.

[60] A. Bellemans and R. K. Nigam, “Phase transitions in the hard-square lattice gas,” *Phys. Rev. Lett.*, vol. 16, pp. 1038–1039, Jun 1966.

[61] R. J. Baxter, “Hard hexagons: exact solution,” *J. Phys. A*, vol. 13, no. 3, p. L61, 1980.

[62] A. Verberkmoes and B. Nienhuis, “Triangular trimers on the triangular lattice: An exact solution,” *Phys. Rev. Lett.*, vol. 83, pp. 3986–3989, Nov 1999.

[63] F. H. Ree and D. A. Chesnut, "Phase transition of a hard core lattice gas. the square lattice with nearest neighbor exclusion," *J. Chem. Phys.*, vol. 45, no. 11, pp. 3983–4003, 1966.

[64] D. Mandal, T. Nath, and R. Rajesh, "Estimating the critical parameters of the hard square lattice gas model," *J. Stat. Mech.*, vol. 2017, no. 4, p. 043201, 2017.

[65] J. Nicholls, G. P. Alexander, and D. Quigley, "Polyomino Models of Surface Supramolecular Assembly: Design Constraints and Structural Selectivity," *ArXiv e-prints*, Feb. 2017.

[66] A. Ghosh, D. Dhar, and J. L. Jacobsen, "Random trimer tilings," *Phys. Rev. E*, vol. 75, p. 011115, Jan 2007.

[67] L. Mao, H. H. Harris, and K. J. Stine, "Simple lattice simulation of chiral discrimination in monolayers," *J. Chem. Inf. Comput. Sci.*, vol. 42, no. 5, pp. 1179–1184, 2002.

[68] B. C. Barnes, D. W. Siderius, and L. D. Gelb, "Structure, thermodynamics, and solubility in tetromino fluids," *Langmuir*, vol. 25, no. 12, pp. 6702–6716, 2009.

[69] D. Mandal and R. Rajesh, "Columnar-disorder phase boundary in a mixture of hard squares and dimers," *Phys. Rev. E*, vol. 96, p. 012140, Jul 2017.

[70] A. Ghosh and D. Dhar, "On the orientational ordering of long rods on a lattice," *Europhys. Lett.*, vol. 78, no. 2, p. 20003, 2007.

[71] J. Kundu, R. Rajesh, D. Dhar, and J. F. Stilck, "Nematic-disordered phase transition in systems of long rigid rods on two-dimensional lattices," *Phys. Rev. E*, vol. 87, p. 032103, Mar 2013.

[72] J. Kundu and R. Rajesh, "Phase transitions in a system of hard rectangles on the square lattice," *Phys. Rev. E*, vol. 89, p. 052124, May 2014.

[73] J. Kundu and R. Rajesh, “Asymptotic behavior of the isotropic-nematic and nematic-columnar phase boundaries for the system of hard rectangles on a square lattice,” *Phys. Rev. E*, vol. 91, p. 012105, Jan 2015.

[74] T. Nath, J. Kundu, and R. Rajesh, “High-activity expansion for the columnar phase of the hard rectangle gas,” *J. Stat. Phys.*, vol. 160, no. 5, pp. 1173–1197, 2015.

[75] P. Gurin, S. Varga, M. G. Pinto, Y. M. Ratan, and E. Velasco, “Ordering of hard rectangles in strong confinement,” *J. Chem. Phys.*, vol. 146, no. 13, p. 134503, 2017.

[76] N. Vigneshwar, D. Mandal, K. Damle, D. Dhar, and R. Rajesh, “Phase diagram of a system of hard cubes on the cubic lattice,” *Phys. Rev. E*, vol. 99, p. 052129, May 2019.

[77] T. Nath and R. Rajesh, “Multiple phase transitions in extended hard-core lattice gas models in two dimensions,” *Phys. Rev. E*, vol. 90, p. 012120, Jul 2014.

[78] R. J. Baxter, “Planar lattice gases with nearest-neighbor exclusion,” *Annals of Combinatorics*, vol. 3, no. 2, pp. 191–203, 1999.

[79] D. W. Blair, C. Santangelo, and J. Machta, “Packing squares in a torus,” *Journal of Statistical Mechanics: Theory and Experiment*, vol. 2012, no. 01, p. P01018, 2012.

[80] P. Decaudin and F. Neyret, “Packing square tiles into one texture,” *Eurographics*, pp. 49–52, august 2004.

[81] L. Walsh and N. Menon, “Ordering and dynamics of vibrated hard squares,” *J. Stat. Mech.*, vol. 2016, no. 8, p. 083302, 2016.

[82] W. Kinzel and M. Schick, “Extent of exponent variation in a hard-square lattice gas with second-neighbor repulsion,” *Phys. Rev. B*, vol. 24, pp. 324–328, Jul 1981.

[83] J. Amar, K. Kaski, and J. D. Gunton, “Square-lattice-gas model with repulsive nearest- and next-nearest-neighbor interactions,” *Phys. Rev. B*, vol. 29, pp. 1462–1464, Feb 1984.

[84] F. H. Ree and D. A. Chesnut, “Phase transition of hard-square lattice with second-neighbor exclusion,” *Phys. Rev. Lett.*, vol. 18, pp. 5–8, Jan 1967.

[85] R. Nisbet and I. Farquhar, “First-order phase transitions in hard-core lattice gases,” *Physica*, vol. 76, no. 2, pp. 283 – 294, 1974.

[86] T. J. Oliveira and J. F. Stilck, “Transfer-matrix study of a hard-square lattice gas with two kinds of particles and density anomaly,” *Phys. Rev. E*, vol. 92, p. 032101, Sep 2015.

[87] D. Poland, “The coexistence curve for a mixture of hard particle lattice gases,” *The Journal of Chemical Physics*, vol. 80, no. 6, pp. 2767–2771, 1983.

[88] D.-J. Liu and J. W. Evans, “Phase transitions in mixed adsorbed layers: Effect of repulsion between hard squares and point particles,” *The Journal of Chemical Physics*, vol. 114, no. 24, pp. 10977–10978, 2001.

[89] J. S. van Duijneveldt and H. N. W. Lekkerkerker, “Three-phase equilibrium in a binary hard-core lattice model,” *Phys. Rev. Lett.*, vol. 71, pp. 4264–4266, Dec 1993.

[90] A. Verberkmoes and B. Nienhuis, “Evidence against a three-phase point in a binary hard-core lattice model,” *Phys. Rev. E*, vol. 60, pp. 2501–2509, Sep 1999.

[91] M. Dijkstra and D. Frenkel, “Evidence for entropy-driven demixing in hard-core fluids,” *Phys. Rev. Lett.*, vol. 72, pp. 298–300, Jan 1994.

[92] M. Dijkstra, D. Frenkel, and J. P. Hansen, “Phase separation in binary hard core mixtures,” *The Journal of Chemical Physics*, vol. 101, no. 4, pp. 3179–3189, 1994.

[93] J. F. Stilck and R. Rajesh, “Polydispersed rods on the square lattice,” *Phys. Rev. E*, vol. 91, p. 012106, Jan 2015.

[94] J. Kundu, J. F. Stilck, and R. Rajesh, “Phase diagram of a bidispersed hard-rod lattice gas in two dimensions,” *EPL (Europhysics Letters)*, vol. 112, no. 6, p. 66002, 2016.

[95] M. Disertori, A. Giuliani, and I. Jauslin, “Plate-nematic phase in three dimensions,” *ArXiv e-prints*, May 2018.

[96] A. Cuetos, M. Dennison, A. Masters, and A. Patti, “Phase behaviour of hard board-like particles,” *Soft Matter*, vol. 13, pp. 4720–4732, 2017.

[97] Y. Martinez-Raton, S. Varga, and E. Velasco, “Biaxial nematic phases in fluids of hard board-like particles,” *Phys. Chem. Chem. Phys.*, vol. 13, pp. 13247–13254, 2011.

[98] S. Dussi, N. Tasios, T. Drwenski, R. van Roij, and M. Dijkstra, “Hard competition: Stabilizing the elusive biaxial nematic phase in suspensions of colloidal particles with extreme lengths,” *Phys. Rev. Lett.*, vol. 120, p. 177801, Apr 2018.

[99] C. Janeway, *Immunobiology Five*. Immunobiology 5 : the Immune System in Health and Disease, Garland Pub., 2001.

[100] J. Li, R. Rajagopalan, and J. Jiang, “Polymer-induced phase separation and crystallization in immunoglobulin g solutions,” *J. Chem. Phys.*, vol. 128, no. 20, p. 205105, 2008.

[101] W. H. Soe, C. Manzano, N. Renaud, P. de Mendoza, A. De Sarkar, F. Ample, M. Hliwa, A. M. Echavarren, N. Chandrasekhar, and C. Joachim, “Manipulating molecular quantum states with classical metal atom inputs: Demonstration of a single molecule nor logic gate,” *ACS Nano*, vol. 5, no. 2, pp. 1436–1440, 2011.

[102] S. Godlewski, M. Kolmer, H. Kawai, B. Such, R. Zuzak, M. Saeys, P. de Mendoza, A. M. Echavarren, C. Joachim, and M. Szymonski, “Contacting a conjugated molecule with a surface dangling bond dimer on a hydrogenated ge(001) surface

allows imaging of the hidden ground electronic state," *ACS Nano*, vol. 7, no. 11, pp. 10105–10111, 2013.

[103] R. J. Baxter, "Hard hexagons: exact solution," *Journal of Physics A: Mathematical and General*, vol. 13, no. 3, p. L61, 1980.

[104] J. Enderby and N. March, "Electron theory of metals and liquid state theory," *Advances in Physics*, vol. 16, no. 64, pp. 691–702, 1967.

[105] D. McQuarrie, *Statistical Mechanics*. University Science Books, 2000.

[106] J. Kundu and R. Rajesh, "Phase transitions in systems of hard rectangles with non-integer aspect ratio," *The European Physical Journal B*, vol. 88, no. 5, p. 133, 2015.

[107] J. Kundu, R. Rajesh, D. Dhar, and J. F. Stilck, "A monte carlo algorithm for studying phase transition in systems of hard rigid rods," *AIP Conf. Proc.*, vol. 1447, no. 1, pp. 113–114, 2012.

[108] R. Alben, "Phase transitions in a fluid of biaxial particles," *Phys. Rev. Lett.*, vol. 30, pp. 778–781, Apr 1973.

[109] J. P. Straley, "Ordered phases of a liquid of biaxial particles," *Phys. Rev. A*, vol. 10, pp. 1881–1887, Nov 1974.

[110] L. J. Yu and A. Saupe, "Observation of a biaxial nematic phase in potassium laurate-1-decanol-water mixtures," *Phys. Rev. Lett.*, vol. 45, pp. 1000–1003, Sep 1980.

[111] G. R. Luckhurst, "A missing phase found at last?," *Nature*, vol. 430, pp. 413–414, July 2004.

[112] R. Berardi and C. Zannoni, "Do thermotropic biaxial nematics exist? a monte carlo study of biaxial gay berne particles," *J. Chem. Phys.*, vol. 113, no. 14, pp. 5971–5979, 2000.

[113] R. Berardi, L. Muccioli, S. Orlandi, M. Ricci, and C. Zannoni, "Computer simulations of biaxial nematics," *J. Phys. Condens. Matter*, vol. 20, no. 46, p. 463101, 2008.

[114] D. Mandal, T. Nath, and R. Rajesh, "Phase transitions in a system of hard y-shaped particles on the triangular lattice," *Phys. Rev. E*, vol. 97, p. 032131, Mar 2018.

[115] T. Nath and R. Rajesh, "The high density phase of the k -nn hard core lattice gas model," *J. Stat. Mech.*, vol. 2016, no. 7, p. 073203, 2016.

[116] P. A. Pearce and K. A. Seaton, "A classical theory of hard squares," *J. Stat. Phys.*, vol. 53, no. 5, pp. 1061–1072, 1988.

[117] K. Binder and D. P. Landau, "Phase diagrams and critical behavior in ising square lattices with nearest- and next-nearest-neighbor interactions," *Phys. Rev. B*, vol. 21, pp. 1941–1962, Mar 1980.

[118] D. S. Gaunt and M. E. Fisher, "Hard sphere lattice gases. i. plane square lattice," *J. Chem. Phys.*, vol. 43, no. 8, pp. 2840–2863, 1965.

[119] R. J. Baxter, I. G. Enting, and S. K. Tsang, "Hard-square lattice gas," *J. Stat. Phys.*, vol. 22, no. 4, pp. 465–489, 1980.

[120] A. Baram and M. Fixman, "Hard square lattice gas," *J. Chem. Phys.*, vol. 101, no. 4, pp. 3172–3178, 1994.

[121] L. K. Runnels, "Hard-square lattice gas," *Phys. Rev. Lett.*, vol. 15, pp. 581–584, Oct 1965.

[122] L. K. Runnels and L. L. Combs, "Exact finite method of lattice statistics. i. square and triangular lattice gases of hard molecules," *J. Chem. Phys.*, vol. 45, no. 7, pp. 2482–2492, 1966.

[123] R. Nisbet and I. Farquhar, "Hard-core lattice gases with residual degrees of freedom at close packing," *Physica*, vol. 73, no. 2, pp. 351 – 367, 1974.

[124] W. Guo and H. W. J. Blöte, "Finite-size analysis of the hard-square lattice gas," *Phys. Rev. E*, vol. 66, p. 046140, Oct 2002.

[125] Y. B. Chan, "Series expansions from the corner transfer matrix renormalization group method: the hard-squares model," *J. Phys. A*, vol. 45, no. 8, p. 085001, 2012.

[126] I. Jensen, "Comment on series expansions from the corner transfer matrix renormalization group method: the hard-squares model," *J. Phys. A*, vol. 45, no. 50, p. 508001, 2012.

[127] H. Meirovitch, "A monte carlo study of the entropy, the pressure, and the critical behavior of the hard-square lattice gas," *J. Stat. Phys.*, vol. 30, no. 3, pp. 681–698, 1983.

[128] C. K. Hu and K. S. Mak, "Percolation and phase transitions of hard-core particles on lattices: Monte carlo approach," *Phys. Rev. B*, vol. 39, pp. 2948–2951, Feb 1989.

[129] D. J. Liu and J. W. Evans, "Ordering and percolation transitions for hard squares: Equilibrium versus nonequilibrium models for adsorbed layers with $c(2\times2)$ superlattice ordering," *Phys. Rev. B*, vol. 62, pp. 2134–2145, Jul 2000.

[130] L. Lafuente and J. A. Cuesta, "Density functional theory for nearest-neighbor exclusion lattice gases in two and three dimensions," *Phys. Rev. E*, vol. 68, p. 066120, Dec 2003.

[131] Z. Ràcz, "Phase boundary of ising antiferromagnets near $h = H_c$ and $t = 0$: Results from hard-core lattice gas calculations," *Phys. Rev. B*, vol. 21, pp. 4012–4016, May 1980.

[132] C. K. Hu and C. N. Chen, "Percolation renormalization-group approach to the hard-square model," *Phys. Rev. B*, vol. 43, pp. 6184–6185, Mar 1991.